UC San Diego
UC San Diego Electronic Theses and Dissertations

Title

Polymer-Mediated Assembly of Nanoparticles into Anisotropic Architectures

Permalink

https://escholarship.org/uc/item/8vn9s44t

Author

Tang, TsungYeh

Publication Date

2019

Peer reviewed|Thesis/dissertation

UNIVERSITY OF CALIFORNIA SAN DIEGO

Polymer-Mediated Assembly of Nanoparticles into Anisotropic Architectures

A dissertation submitted in partial satisfaction of the
requirements for the degree
Doctor of Philosophy

in

Materials Science and Engineering

by

Tsung-Yeh Tang

Committee in charge:

    Professor Gaurav Arya, Chair
    Professor Sunil K. Sinha
    Professor Andrea Tao
    Professor Oscar Vazquez Mena
    Professor Kesong Yang

2019

The dissertation of Tsung-Yeh Tang is approved, and it is acceptable in quality and form for publication on microfilm and electronically:

_____

_____

_____

_____

_____

Chair

University of California San Diego

2019

EPIGRAPH

When we try to pick out anything by itself, we find it hitched

to everything else in the Universe.

—John Muir

TABLE OF CONTENTS

<h1 style="text-align:center">LIST OF TABLES</h1>

ACKNOWLEDGEMENTS

I would like to thank my advisor Prof. Gaurav Arya, who has been unfailingly patient in guiding me toward the completion of my degree. Your brilliance, positive attitude at work, and sense of humor will always be an inspiration to me. Thanks to all my coauthors, especially Dr. Jing-Jin Song and Prof. Sunil Sinha, your input was instrumental in the successful publication of our work. Without your contributions, I would not have made it to the high-profile journals as we did. I would also like to thank Dr. Su-Wen Hsu and Prof. Andrea Tao. It was a privilege to work in close collaboration with you. Last but not least, I would like to thank my parents, family members, and my lovely wife for their unconditional support during the past five years. Without you, my journey in academic research would not have been so smoothly.

Chapter 2, in full, is a reprint of the material as it appears in *Macromolecules*: Tsung-Yeh Tang, and Gaurav Arya. "Anisotropic Three-Particle Interactions between Spherical Polymer-Grafted Nanoparticles in a Polymer Matrix." *Macromolecules* 50, no. 3 (2017): 1167-1183. The dissertation author was the primary investigator and author of this paper.

Chapter 3, in full, is a reprint of the material as it appears in *ACS Nano*: Tsung-Yeh Tang†, Yilong Zhou†, and Gaurav Arya. "Interfacial Assembly of Tunable Anisotropic Nanoparticle Architectures." *ACS Nano*. The dissertation author was the primary investigator and author of this paper. 13, no. 4 (2019): 4111-4123. † These authors contributed equally to this work.

Chapter 4, in part, is a reprint of the material as it appears in *Physical Review Letters*: Jing-Jin Song, Rupak Bhattacharya, Yi Yang, Sajal K. Ghosh, Sunil K. Sinha, Hyunki Kim, Jooyoung Chang, Hyeyoung Kim, Thomas P. Russell, Tsung-Yeh Tang, Gaurav Arya, Hongyu Guo, Suresh Narayanan and Zhang Jiang. "One-Dimensional Anomalous Diffusion of Gold Nanoparticles in a Polymer Melt." *Physical Review Letters*. 122, no. 10 (2019): 107802. The dissertation author was the collaborating investigator and author of this paper.

2019	Ph. D. in Materials Science and Engineering, University of California, San Diego
2013	M. S. in Materials Science and Engineering, National Tsing-Hua University, Taiwan
2010	B. S. in Materials Science and Engineering, National Tsing-Hua University, Taiwan

PUBLICATIONS

T.Y. Tang, Y. Zhou, and G. Arya. "Interfacial Assembly of Tunable Anisotropic Nanoparticle Architectures". *ACS Nano*, 13, no. 4 (2019): 4111-4123.

J.J. Song, R. Bhattacharya, H. Kim, J. Chang, T.Y. Tang, H. Guo, S. K. Ghosh, Y. Yang, Z. Jiang, H. Kim, T. P. Russell, G. Arya, S. Narayanan, and S. K. Sinha. "One-dimensional anomalous diffusion of gold nanoparticles in a polymer melt". *Phys. Rev. Lett.*, 122, no. 10 (2019): 107802.

T.Y. Tang, and G. Arya. "Anisotropic Three-Particle Interactions between Spherical Polymer-Grafted Nanoparticles in a Polymer Matrix". *Macromolecules*, 50, no. 3 (2017): 1167-1183.

Y.W. Harn, T.H. Yang, T.Y. Tang, M.C. Chen, and J.M. Wu. "Facet-Dependent Photocatalytic Activity and Facet-Selective Etching of Silver(I) Oxide Crystals with Controlled Morphology". *ChemCatChem*, 7, no. 1 (2015): 80-86.

ABSTRACT OF THE DISSERTATION

Polymer-Mediated Assembly of Nanoparticles into Anisotropic Architectures

by

Tsung-Yeh Tang

Doctor of Philosophy in Materials Science and Engineering

University of California San Diego, 2019

Professor Gaurav Arya, Chair

Polymer-nanoparticle composites have attracted considerable interest over the past few decades. While many traditional applications of composites require the nanoparticles (NPs) to remain well dispersed within the polymer matrix, some of the newer proposed applications rely on higher-order organization of NPs. Self-assembly provides a powerful bottom-up approach for organizing nanoparticles in a highly parallelized fashion. However, directing nanoparticles to self-assemble into anisotropic architectures more complex than the isotropic, close-packed structures or random aggregates observed under equilibrium or non-equilibrium conditions is highly challenging. In this dissertation, I will demonstrate how we have used molecular dynamics simulations to investigate and propose new polymer-mediated strategies for assembling spherical

NPs into anisotropic, and often unique, configurations.

We first investigated the underlying basis for anisotropic interactions between spherical NPs uniformly grafted with polymer chains, which were recently shown to assemble into anisotropic phases like strings and sheets. The anisotropy was shown to arise from the expulsion of polymer grafts between two contacting NPs, which led to anisotropic graft-mediated steric repulsion felt by a third approaching NP. Our computed phase diagram for formation of isotropic versus anisotropic 3-particle clusters agreed qualitatively with that obtained experimentally for larger aggregates of NPs. Next, we proposed a new strategy for assembling spherical nanoparticles into unique, anisotropic architectures in a polymer matrix. The approach takes advantage of the interfacial tension between two mutually immiscible polymers forming a bilayer to trap NPs within two-dimensional planes parallel to the interface. We demonstrated both trapping NPs at tunable distances from the interface and assembling them into a variety of unconventional nanostructures. We also developed a theoretical model to predict the preferred positions and free energies of NPs. Lastly, we studied the dynamics of polymer-grafted gold nanoparticles loaded into polymer melts. Under certain annealing conditions, the diffusion is one-dimensional and related to the direction of heat flow during annealing and is associated with an dynamic alignment of the host polymer chains. We used molecular dynamics simulations to investigate a single gold nanoparticle diffusing in a partially aligned polymer network which semi-quantitatively reproduce the experimental results to a remarkable degree.

Chapter 1

Introduction

In the past decades, researchers have made tremendous progress in the field of materials science owing to rapid advancements in nanoparticle synthesis and assembly methods. Nanoparticles possess unique electronic and chemical properties, as they have large surface area with respect to the volume, which makes them promising candidates for materials applications. However, precise control over the organization of these extremely small particles into desired devices with specific functions remains a challenge. In the recent past, researchers have demonstrated self-assembly of nanoparticles into increasingly complex higher-order structures with versatile applications in fields ranging from plasmonics, optoelectronics, and molecular sensing to medicine and drug delivery [1–9]. Self-assembly refers to process where discrete components spontaneously aggregate into a group or a cluster in order to minimize the free energy in the system. The driving forces for such process may arise from specific interactions among the components or from their environment. Self-assembly of nanoparticles has long been considered as a powerful strategy to fabricate ordered macroscopic structures [10–14]. However, to avoid random aggregation and flocculation, high degree of control over the interactions between nanoparticles is required. Directed self-assembly offers a promising route to achieve more regular assembly of nanoparticle building blocks. It basically employs the same idea of self-assembly, but involves the use of chemical functionalization, templates, or external fields to

promote anisotropic interparticle forces between particles.

In the following section, I will review previous work on utilizing polymers and external fields for controlled assembly of nanoparticles. Considering the breadth of this topic, I would mainly focus on the systems that involve synthetic polymers and address only a few of the most significant works that was carried out using biological polymers (e.g. DNA).

1.1   Directed Assembly of Nanoparticles

The ability to exploit nanoparticle properties to device fabrication requires high degree of control over the aggregation process. The aim is to initially avoid random aggregation and flocculation, and eventually achieve desired structures. When it comes to nanofabrication, the challenge lies in the rather weak and specific interaction forces which are hard to be harnessed. There has been works that took different routes to achieve precise nanostructures, for example, by operating the cantilever of AFM to accurately place nanoparticles to the designated positions one by one [15], or by depositing nanoparticles onto stretchable elastomeric films and then tune the position of each nanoparticle through stretching the film [16]. However, this process of fabricating is either very time-consuming or expensive. In contrast, polymer scaffold directed self-assembly provides various promising routes that ensure low-cost and efficient scale-up. Either through intermolecular interactions between the polymer capping agents or through the surrounding polymer template, the distribution and alignment of nanoparticle assemblies can be effectively controlled. The morphology of nanoparticle assemblies can be further reconfigured through the use of stimuli-responsive polymers that respond to stimuli such as temperature, pH, light irradiation, solvent polarity or redox activity.

1.1.1 Template Supported Self-Assembly

Templates, in the context of nanofabrication, can be considered as surface-modified substrates containing active sites that allow nanoparticles to selectively attach upon. The size of the template can range from below to above the size of the nanoparticles, and the dimension can be 1D, 2D or 3D, as long as the template can serve as a scaffold for nanoparticles to arrange to whose morphology is complementary to that of the template. Templates can be soft (e.g., small molecule, linear polymer, biomolecule (DNA), copolymer), which offer better spatial distribution of the active sites for nanoparticle deposition, or hard (e.g., carbon nanotube), which provide relatively poor control over the particle distribution yet better performance at directing nanoparticle assembly. Small molecules are often relatively less complicated and inexpensive to synthesize which make them great candidates for use in nanoparticle self-assembly. For instance, specific halogen bonding was used to direct gold nanoparticle aggregation by exploiting the donor-acceptor interaction [17]. Chainlike structure or other dense assembly structures can therefore be obtained by manipulating the assembly time and template concentration. The challenge of using small molecule is that they can easily result in irreversible nanoparticle aggregation. Fortunately, it has been shown that some of those that are sensitive to pH or temperature can leads to interesting applications in reversible self-assembly [18, 19]. A more interesting approach was proposed for reversible clustering of gold nanoparticles functionalized with molecules containing active guest units that interact with a template containing host units [20]. Via cyclic redox process, this host-guest interaction can lead to fully reversible assembly in solution, and by varying the initial symmetry of template allows the assembly into dimers, trimers and tetramers. This concept was further extended by combining the host units with linear polymers [21], so that more complex network of nanoparticles cross-linked with polymer could be obtained.

The idea of using DNA for directing nanoparticle self-assembly has become popular in the past two decades since it was proposed [22–28]. It has been shown that using oligonucleotide

as backbone for nanoparticle deposition to the selective sites can result in different symmetries of nanoparticle assemblies [23]. Nanoparticles made out of gold, which has great compatibility with DNA, can be functionalized with DNA strands to form either network materials or discrete assemblies. In this case, gold nanoparticles tethered with non complementary DNA strands will spontaneously aggregate upon the addition of double-complementary DNA strand. This coupling interaction between the complementary strands can be "switched off" when the system is heated above the DNA melting temperature which leads to spontaneous disassembly of the aggregates. A temperature responsive device can thus be achieved using this concept. A similar idea was employed by attaching single-stranded DNA-modified nanoparticles onto an unmodified DNA template strand [25]. By attaching similar and different-sized nanoparticles onto the DNA strand, different final configurations of assemblies can be achieved. In addition to simple linear DNA-nanoparticle composites, more complex structures can also be fabricated using a similar approach. For instance, DNA-modified gold nanoparticles can assemble into uniform linear chains surrounding a template consist of DNA-functionalized Navicula diatom [29].

The discussion above has shown that the control of nanoparticle self-assembly can be achieved over nanoscale distances. However, as the needs for technological applications may require control over longer length-scale, the above tactics of exploiting short-ranged interparticle interaction forces may not be applicable. Block copolymer offers feasible routes to control organization over longer distances, and their well-defined microphase-separated domains provide an ideal platform for directing nanoparticle assembly over macroscopic distance [30]. This process requires surface modification of nanoparticles with polymers compatible with either side of the copolymer. Nanoparticles with surface-modification will therefore migrate to its favored domain and be constrained at the center or at the edge of the specific matrix domain depending on the size. It is known that grafted particles of bigger sizes would tend to locate at the center of the domain for less conformational entropic loss, while smaller particles in contrary would tend to stay at the edge of the domain to minimize the interfacial energy between two distinct monomer layers. Initially, nanoparticle assemblies are arranged in a low degree of order.

However, after thermal annealing above a certain temperature, nanoparticle assemblies become ordered and aligned in the direction parallel to the polymer matrix blocks. It was also shown that upon continuous quenching, the monolayer of nanoparticle assembly will gradually transform into double layer assemblies [31].

1.1.2 Directed Self-Assembly Without Template

In the previous section, the nanoparticles were assembled into specific positions or relative positions based on the external scaffolding molecules or domains (template). However, particles can also be made to assemble into specific configurations through their interparticle interactions without the help of external template by functionalizing the particles with small molecules, polymers, or DNA (capping agents). The distribution of the capping agents on the surface of nanoparticles is especially important, as asymmetric distribution can result in patchy nanoparticles and therefore leads to anisotropic assembly.

As previously mentioned, the utilization of complementary DNA strands to direct nanoparticle assembly has led to many interesting applications [32, 33]. It has been shown that asymmetric distribution of DNA on the surface of nanoparticle can result in anisotropic self-assembly. With rational control of the synthesizing process or modulating the cDNA grafting density, the shape of the assembly can be manipulated from dimer [24] to dendrimer [34]. Certain groups of organic molecules has been found to change their physical properties under light irradiation [35]. When irradiated with light of a specific wavelength, they become polar, which lead to particle self-assembly. While under light irradiation with different wavelengths, they return to nonpolar, and thus particles segregate. This is because these molecules possess special property of photoisomerization that allows them to transit from a more stable trans state into the cis state, thereby the induced dipole-dipole attraction drives nanoparticles into assemblies.

Stacking interactions between NPs tethered with π-conjugated polymers has also been found to provide good control for directing nanoparticle self-assembly [36]. By changing the

fraction of the polar component, the shape of the nanoparticle clusters will also transform. It has been shown that solvent mixture fraction can also play a crucial role. For example, gold nanorod assembly in a DMF/THF-water mixtures changes its shape from dimer, chainlike structures, to spherical aggregates by changing the water volume fraction [37].

1.1.3 Self-Assembly Directed by External Fields

Nanoparticle assembly in electric fields occurs due to induced dipole-dipole interactions. The reason that most particles polarized in electric field arise from the mismatch of their dielectric properties. When particles are polarized, the induced field surrounding them takes the form of a dipole and leads to anisotropic dipole-dipole interaction between them. When this interaction is sufficiently stronger than thermal energy $k_\mathrm{B}T$, particles will form dipolar chains whose length increases with time. The challenge is that when the size of the particle approaches nanoscale, the magnitude of the dipole-dipole interaction also decreases accordingly which prevents nanoparticle aggregation. However, it has been shown that applying stronger field gradient arising from the dielectric difference can lead to successful crystallization of nanoparticles [38]. Even though most studies have used spherical particles, it has been shown that using non-spherical particles can lead to interesting ordering of particles in external fields. For instance, at lower concentration, Janus particles under AC field will form staggered chain structure [39]. In another instance, polarizable ellipsoids in electric fields form zig-zag chains at low density but centered rectangular structures at higher density [40].

In a system comprised of two immiscible fluids, the natural tendency of a neutral nanoparticle is to migrate to the fluid interface to reduce the interfacial energy. Thus a fluid interface can also be considered as a template for nanoparticle assembly. It is especially powerful for directing self-assembly of particles with nonspherical shapes by constraining the particle clusters to 2D space. Nonspherical particles, say prolate and oblate, will be forced to lay flat at the interface, and unable to flip up without sufficiently high surface pressure [41, 42]. Using the

same concept, by controlling the aspect ratio, surface properties and concentration, it is possible to generate different orientations and structures of nanorods. Furthermore, it has been shown that silver nanocrystals at air-water interface tend to form spherical aggregations at lower density and stripelike aggregation at higher density [43].

1.2   Control over Interparticle Spacing and Orientation

As the electromagnetic properties of nanoparticle-polymer composites strongly depend on the distance between neighboring particles, strong control over interparticle distances is key to applications in fields such as plasmonics, optoelectronics and sensing. Polymers can serve as good separators in different forms for keeping nanoparticle assemblies in the desired interparticle distances.

1.2.1   Polymer Size Determined NP Spacing and Orientation

A common route to controlling interparticle distances involves tethering polymer ligands onto the surface of nanoparticle to create a protecting monolayer with specific thickness to avoid close-packed aggregation of nanoparticles. Due to the presence of depletion force, the polymer-tethered nanoparticles will still aggregate, but maintain an interparticle distance roughly equal to twice the thickness of the protecting monolayer. As a result, the interparticle spacing can be tuned by the length of the polymer ligands and the grafting density.

It has been shown by Ohno et al. that gold nanoparticles coated with well-defined high-density polymer brushes can be a potential building blocks for optical applications [44]. The interparticle distance in this case is determined by the graft chain length of poly(methyl methacrylate) (PMMA) which led to a tunable gap range from 10 nm to over 40 nm. They also observed a blue shift of surface plasmonic absorption becoming more significant with increasing PMMA chain length. Norsten et al. employed similar strategy by altering the chain lengths of

the terpy ligands and the supporting monolayer to systematically control the interstitial distance between terpyridine capped gold nanoparticles [45]. Their results examined by using small angle X-ray scattering show that the control over this spacing is very subtle in the range of sub-nanometer scale.

Shaped nanoparticles are also important building blocks for constructing functional complex devices. Different from spherical particles, changes in interparticle spacing within shaped nanoparticle clusters by altering the length of ligands is also usually accompanied by orientation changes. Taking nanocubes for instance, when there is no polymer ligands grafted or only short ligands grafted, nanocubes organize into close-packed face-to-face clusters to maximize van der Waals interactions. However, face-to-face configuration becomes disfavored when the number or length of grafted polymers increase leading to increasing steric repulsion between the grafted chains, which eventually results in edge-to-edge configuration. This interesting phenomenon has been experimentally demonstrated and theoretically modeled by Gao et al. [46]. Moreover, they have also shown that this strategy can be applied on other anisotropic particles such as nanorods and triangular nanoprisms, and if implemented in membrane, can even be achieved on isotropic nanoparticles (i.e. spheres) [47].

1.2.2 "Brick and Mortar" Approach

Another route to regulate interparticle spacing is through the so-called "brick and mortar" approach that generally employs dendrimers to promote nanoparticle assembly [48]. In this approach, funtionalized nanoparticles act as "brick" and polyamidoamine (PAMAM) dendrimers of different generations as "mortar". The salt-bridge formation between PAMAM and nanoparticles lead to electrostatic self-assembly which results in periodic nanocrystal thin films. The interstitial distance between two nanoparticles is therefore determined by the generation (number size) of the dendrimer. This approach offers great control over interparticle spacing for 3D structures with efficient scale-up and periodic patterns. Ordered mesoporous nanocomposites

with tunable mesopore sizes in the scale of sub-20 nm can thus be achieved with potential applications in energy storage [49–52]. However, the power of this approach is limited to 3D assembly as the "mortar" can randomly attach on any active site on the "brick", eventually leading to isotropic assembly. To further extend the applicability of this approach, introduction of anisotropic interactions is required. The idea of employing polymers as separating entities has been also achieved using block copolymers or patterned surfaces that lead to 1D or 2D assembly with tunable spacing between nanoparticle clusters, which will be discussed in the following sections.

The versatility of polymer dendrimers has also gained attention from the simulation fields. Paulo et al. performed molecular dynamic simulations of charged PAMAM dendrimers with low to intermediate half-genereation using optimized potential for liquid simulations force field that shows great agreement with experimental data [53]. On the other hand, Lee et al. employed the MARTINI coarse-grained force field [54] for higher generation of PAMAM dendrimers which results in better accuracy as it distinguish nodes and branches in interior parts [55]. Despite advances in dendrimer modeling, a quantitative understanding of the ability of dendrimers to tune the interparticle spacing is rather poor.

1.2.3 Spacing Control With Environmental Constraints

While interparticle spacing can be well controlled using the approaches mentioned in the previous sections, the size of this spacing is limited by the size of the mediated polymer, usually less than 10 nanometers. Thus, nanoparticle self-assembly via environmental constraints plays an important role to extend interparticle or intermolecular distance from nanometer to micrometer scales. This can be achieved by intergrating nanoparticles with immiscible bilayer stacks where nanoparticles are designed to be selectively compatible to one side of the layer, or by nanoparticles deposition onto patterned templates with predefined spacing patterns. Additional advantages of these approaches include allowance for on-chip fabrication, 1D and 2D ordered

particle organization, and massive scalability.

Diblock copolymers, polymer consisting of two long sequence of distinct co-monomers, have been widely used for fabricating ordered 1D, 2D and 3D nanopaticle arrays. The unique feature of their periodic lamellar structure has also been employed for manipulating interparticle spacing. The idea is to induce self-assembly of nanoparticles within one of the domains formed by the block copolymer. Ideally, nanoparticles will assemble into organized linear or planar structure parallel to each lamellar domain. Binder et al. demonstrated a different approach to controlling interparticle spacing by selectively binding surface-modified nanoparticles onto specific regions of microphase-separated block copolymer thin films [56]. However, at the time, the separation of nanoparticle assembly among each domain was not as clear. Later on, Zhao et al. demonstrated a novel approach to produce hierarchical assemblies of nanoparticles by combining small molecules and block copolymer without the need of chemical modification of either nanoparticles or block copolymers [57]. The addition of small molecules provides new possibilities in directing interparticle ordering. Interestingly, their results show that the separation of particle layers is responsive to heat. At low temperature, nanoparticles reside in the center layer of each favored lamellae forming parallel and periodic nanoparticle layers with separation distance about the period of lamellae. When the temperature rises up, they migrate to the interface between two distinct lamellaes. The separation distance between nanoparticle layers was found to be around half of the lamellar period. They also found that this process is reversible and applicable to a wide range of nanoparticles. Furthermore, they showed that this approach can be extended to hexagonal grid of block copolymer structure that lead to periodic patterns of nanoparticles preferentially sequestered in the corners of the hexagons.

Despite that block copolymers provides versatile approaches to manipulation of interparticle spacing, their limited ability to create vertically stacked lamellae with respect to substrate can limit their utility in optical and electromagnetic applications.

1.3   Motivations for Dissertation Work

We outlined several key aspects of nanoparticle assembly in terms of achieving structural and morphological control over nanoparticle higher-order assemblies. In particular, we highlighted the use of polymers and external fields to direct nanoparticle assembly. Functionalized polymers can be used to induce anisotropic ordering of nanoparticles, tune interparticle spacing, and control over assembly shape, size, and porosity. Some of the polymers respond to external stimuli such as pH, temperature, solvent polarity and light, which can be further applied to fabricate particle assemblies with reversible properties. External fields can be used for efficient scale-up of ordered nanoparticle assembly and to increase the morphological consistence. Moreover, nanoparticle assembly can present unusual alignment coupling with external fields and therefore yield more complex nanocomposite structure.

Despite the success in controlling the structure and morphology of nanoparticle assembly to some extent, there are still various challenges to be resolved. For instance, isotropic nanoparticles were originally thought to be incapable of forming aggregates other than isotropic, close-packed structured (under equilibrium assembly conditions). Although it has been recently demonstrated that isotropic nanoparticles can form anisotropic aggregates like 1D strings and 2D monolayers, the mechanism was unclear. Furthermore, strategies to trap and direct the assembly of isotropic nanoparticles into more unique and anisotropic higher order structures are rare. There is also relatively little research focusing on directing nanoparticle assembly at the polymer/polymer interface without resorting to strongly charged polymers possibly due to our limited ability in fabricating stable polymer layer stacks. The techniques for generating stable polymer layer stacks have improved significantly, but researchers have yet to investigate how nanoparticles might assemble within such stacks. All of these topics will be addressed in this dissertation using coarse-grained models and molecular dynamics simulations. Finally, a close collaborative research with experimentalists showcases the ability of our approaches not only in effectively reproducing experimental results but also in providing new insights and interpretation

of the experiments.

Chapter 2

Anisotropic 3-Particle Interactions Between Spherical Polymer-Grafted Nanoparticles in a Polymer Matrix

2.1 Introduction

An emerging concept in materials science is the engineering of anisotropic interactions between nanoparticle (NP) building blocks to drive their self-assembly into higher-order structures more complex than the random aggregates or simple close-packed lattices nominally obtained from spherical NPs [58, 59]. Anisotropic interactions are most intuitively achieved by using particle shapes that go beyond simple spheres [60], that is, by exploiting the inherent anisotropy in the excluded volume interactions between "shaped" NPs. Materials chemists are now able to synthesize a rich variety of particle shapes, ranging from simple rods and discs to more exotic ones like cones, tetrapods, and various kinds of polyhedra [60–64], and assemble them into anisotropic structures with some degree of success [46, 65, 66]. Alternatively, the surface of NPs may be grafted or coated with chemical ligands in an anisotropic manner to produce gradients or discrete patches of ligands. Such "patchy" NPs may be designed to exhibit anisotropic steric

repulsion through polymer grafting [67, 68], anisotropic attraction through grafting of sticky molecules such as single-stranded DNA [69], or anisotropic response to external fields like magnetic fields [70].

Recent studies however suggest that even NPs exhibiting isotropic two-body interaction potentials may assemble into anisotropic structures [43, 71, 72]. The most striking evidence comes from recent experiments on the assembly of spherical silica NPs uniformly grafted with polystyrene chains within a polystyrene matrix [72]. It was found that in addition to exhibiting dispersed and densely-packed aggregate phases expected of isotropic particles, these NPs also assembled into anisotropic structures like 1D strings and 2D sheets, depending on the length and surface density of their polymer grafts. Similar anisotropic phases have been observed in other grafted-NP systems as well [73–76] and also realized in molecular dynamics and Monte Carlo simulations of simplified models of polymer-grafted NPs [72, 73, 77]. To explain the observed "phase diagram", it was proposed that the free energy of each phase is determined by a competition between favorable enthalpic energy gained by forming contacts between NPs and the entropic cost associated with compressing the polymer grafts to form such contacts [77]. In general, the higher the dimensionality of a phase, the larger the number of favorable contacts its NPs exhibit and the stronger the confinement that their grafted chains experience. By using simple scaling relationships for the two effects, structures with the lowest free energy were determined at various points across the parameter space, yielding a phase diagram that qualitatively agreed with that observed experimentally.

Key to the unusual stability of anisotropic structures in polymer-grafted NPs is the anisotropic distribution of polymer grafts that is supposed to develop when NPs come into close contact [72, 73, 77]. Specifically, approaching NPs push aside the intervening polymer grafts, causing an increase in polymer density near the contact region of the NPs. This effect is believed to introduce an anisotropic steric repulsion felt by a third approaching NP, wherein the dimer becomes more susceptible to binding by the third NP at its two poles on the longitudinal axis as compared to the contact region, thus providing a natural driving force for the assembly of NPs

14

into 1D strings. One would also presume that this steric repulsion increases as one moves away from the NP poles and towards the contact region, and hence, binding of NPs at other locations along this path may be favored if the steric repulsion at those locations can be compensated by additional favorable contacts between the ensuing higher-order structures. Indeed, in the absence of any such emergent 3-body anisotropic interactions arising from the polymer, the NPs would either assemble into 3D hexagonally close-packed ("isotropic") structures that maximize the number of attractive contacts between NPs or else remain dispersed if the attraction was sufficiently weak.

Here we investigate such polymer rearrangement-based origin of anisotropic interactions between polymer-grafted NPs, a key *hypothesis* that has surprisingly not been tested thus far. Our approach involves using molecular dynamics (MD) simulations of coarse-grained models of the NP-polymer system to directly compute the potential of mean force of interaction between an isolated NP and a NP dimer as a function of their relative separation and orientation, and to relate any observed anisotropy in the computed interaction to that in the polymer conformations and density. Our results provide the first direct confirmation of the above hypothesis and reveal new insights into how the grafted and matrix polymer conspire to produce anisotropic interactions between NPs. We further demonstrate how variations in anisotropic interactions with respect to parameters like NP-graft length, grafting density, and interparticle-attraction strength lead to intriguing "phase behavior" among various NP cluster configurations, including a novel globally-stable dimer phase whose existence remains to be tested experimentally.

2.2   Computational Methods

2.2.1   System Design and Configuration

Our aim is to investigate the anisotropy in the free energy of interactions—the potential of mean force (PMF)—between an isolated polymer-grafted NP termed "test" NP and a
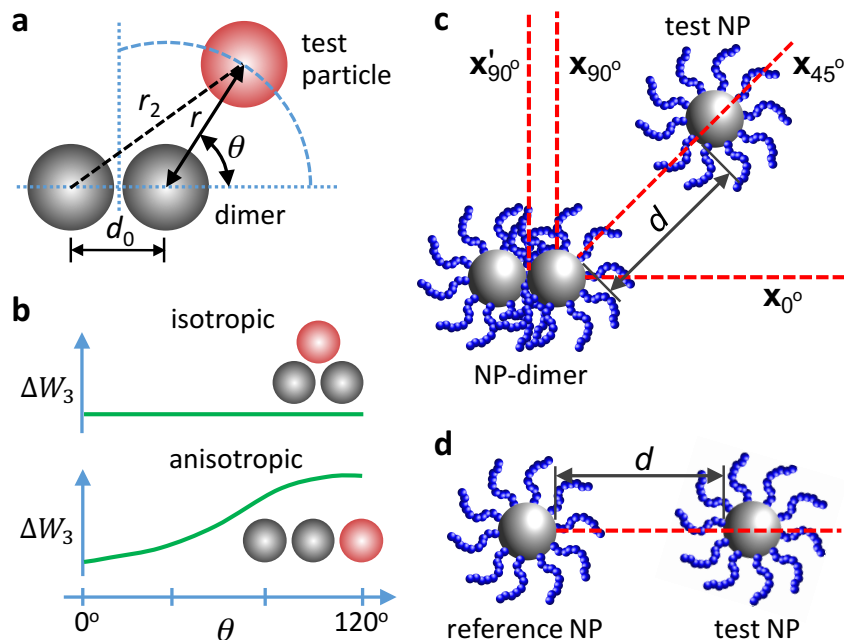
Figure 2.1: (a) Coordinate system used for describing anisotropic interactions in a 3-particle system. The test and dimer particles are identical but shown in different color for clarity. (b) Schematic illustrating how a strong angular-dependence (anisotropy) in the 3-body PMF ΔW_3 can cause particles to assemble into anisotropic structures. (c) Schematic showing the four reaction coordinates chosen for examining the anisotropy in 3-particle interactions between polymer-grafted NPs. The NP cores are shown as grey circles and the polymer grafts as blue chains. The polymer matrix is not shown for clarity. (d) Schematic showing the reaction coordinate used for computing the isotropic 2-particle interactions. All interactions were computed as a function of the surface-to-surface distance d between the test NP and the reference NP cores (or those of the nearest dimer NP).

pre-assembled dimer of polymer-grafted NPs in a polymer matrix and to examine how such interactions lead to anisotropic structures. Due to the symmetry of the dimer, the PMF can be described in terms of two coordinates: the center-to-center distance r between the test NP and the right-hand-side dimer NP, and the angle θ subtended by the line connecting the centers of these two NPs with the longitudinal axis of the dimer for characterizing the anisotropy in the system. Note that the angle varies in the range $\theta = \left[0, \pi - \cos^{-1}(d_0/2r)\right]$, where d_0 is the fixed center-to-center distance between the two dimer NPs (Fig. 2.1a).

To define "anisotropic structures" and "anisotropic interactions" in the context of such a 3-particle system, we consider a simpler example where we replace the polymer matrix with

vacuum and replace the polymer-grafted NPs with single particles that interact with each other via a pairwise-additive isotropic potential $U(r)$ that exhibits a single minimum at $r = r_{\min}$. Since the interaction depends on a single degree of freedom (r), the 2-body PMF $W_2(r)$ for this interaction is simply equal to $U(r)$. The *overall* 3-particle PMF $W(r, \theta)$ for the interaction between the test particle and the dimer is equal to the sum of the 2-body PMFs of the test particle with each of the two dimer particles: $W(r, \theta) = W_2(r) + W_2(r_2)$, where r and $r_2 \equiv r_2(r, \theta)$ are the separation distances between the test particle and the two dimer particles. Thus, the overall PMF depends on the orientation angle θ (due to the interaction $W_2(r_2)$ arising from the left-hand-side dimer particle) and is therefore anisotropic. The most stable state of such a system is obviously one in which the test particle sits symmetrically atop the dimer at a separation distance of $r = r_2 = r_{\min}$ and $\theta = \pi - \cos^{-1}(d_0/2r_{\min})$ coinciding with the minima of both the 2-body PMFs. We define this compact, assembled state of particles as the "isotropic structure" for the 3-particle system, and all other configurations such as the linear configuration of the three particles (where $\theta = 0$) are termed as "anisotropic structures".

The above example clearly demonstrates that: (1) the anisotropy in the overall PMF $W(r, \theta)$ is *not* the most appropriate indicator of the formation of anisotropic structures, and (2) overall PMFs that can be written as the pairwise sum of isotropic 2-body PMFs exhibiting a single energy minimum will always form isotropic structures. Anisotropic structures in such systems must therefore arise from multi-body contributions, or 3-body contributions in the context of 3-particle systems. The overall 3-particle PMF is then given by $W(r, \theta) = W_2(r) + W_2(r_2) + \Delta W_3(r, \theta)$, where ΔW_3 represents the 3-body contribution that likely depends on r and θ. Thus, if ΔW_3 exhibits a strong angular dependence (anisotropy), it allows for the possibility of anisotropic structures becoming more stable than isotropic structures, e.g, when ΔW_3 is much larger for isotropic than anisotropic configurations (Fig. 2.1b). Hence, we define "isotropic interactions" by interactions that either lead to negligible $\Delta W_3(r, \theta)$ or angle-independent $\Delta W_3(r, \theta) \approx \Delta W_3(r)$, whereas "anisotorpic interactions" are defined in terms of the strength and anisotropy in $\Delta W_3(r, \theta)$. In our polymer-grafted NPs, we expect $\Delta W_3(r, \theta)$ to arise

from the expulsion of polymer grafts from in between the two dimer NPs.

We aim to compute and analyze the distance- and orientation-dependent behavior of the overall PMF $W(r,\theta)$ as well as its 3-body contribution $\Delta W_3(r,\theta)$. The first quantity provides a measure of the overall free energy of the 3-particle system and helps determine the stability of the various assembled configurations of the system, both isotropic and anisotropic. The latter quantity provides a measure of the "anisotropicity" in the interactions between the test NP and the NP-dimer and its underlying source. However, traversing such a two-dimensional coordinate space in r and θ would entail prohibitive computational costs. To this end, we computed the PMF along four representative "reaction coordinates" spanning the relevant angular space around one of the dimer NPs (Fig. 2.1c): (1) longitudinal axis of the NP dimer (denoted by $\mathbf{x}_{0^\circ}$), (2) tilted axis oriented 45° with respect to the longitudinal axis denoted by ($\mathbf{x}_{45^\circ}$), (3) perpendicular axis oriented 90° with respect to the longitudinal axis denoted by ($\mathbf{x}_{90^\circ}$), and (4) different perpendicular axis that passes through the dimer center of mass rather than through the NP center ($\mathbf{x}'_{90^\circ}$). The PMFs were obtained as a function of the surface-to-surface distance d between the cores of the test NP and the closest dimer NP, and *not* the center-to-center distance as typically used. For comparison, we also computed "2-particle" PMF between a test NP and an isolated or "reference" NP as a function again of their surface-to-surface distance d (Fig. 2.1d).

2.2.2   Coarse-Grained Model

To compute the PMFs between polymer-grafted NPs in a polymer matrix, we adopted a coarse-grained model (Fig. 2.2a) similar to one we previously used for investigating the viscoelastic properties of polymer-nanoparticle composites [78]. The model is simple, computationally efficient, and captures the essential physics of free and grafted polymer chains and the interactions between NP cores.

According to this model, segments of the grafted and matrix polymer chains were treated as beads of size σ and mass m (Fig. 2.2b) [79]. Adjacent segments in each chain were connected

18

by a finitely extensible nonlinear elastic (FENE) spring with potential energy given by

$$U_{\text{FENE}} = -\frac{k}{2}R_0^2 \ln\left[1 - \left(\frac{r}{R_0}\right)^2\right],$$ (2.1)

where r is the separation distance between the bonded segments, $R_0 = 1.5\sigma$ is the maximum possible length of the spring, $k = 30\varepsilon/\sigma^2$ is the spring constant, and ε is the characteristic energy parameter of the system. The above choice of parameters ensures that chains do not cross each other. Excluded volume interactions between all pairs of polymer segments, bonded or nonbonded, were treated using a short-range, purely repulsive potential [80]

$$U_{\text{ev}} = \begin{cases} 4\varepsilon\left[\left(\frac{\sigma}{r}\right)^{12} - \left(\frac{\sigma}{r}\right)^6 + \frac{1}{4}\right] & r \leqslant 2^{1/6}\sigma \\ 0 & r > 2^{1/6}\sigma \end{cases},$$ (2.2)

where r is the distance between the segments. While highly simplified, this polymer model captures well various experimentally measured structural and dynamical properties of simple polymeric melts spanning the Rouse and reptation regimes, including the chain-length dependence of the diffusion coefficient and the relaxation of the structure factor [79]. In this study, we examined graft chains of lengths L_{g} (in terms of number of segments) in the range 5 to 20 and matrix chains of lengths L_{m} in the range 1 to 40 segments. Apart from possible differences in their lengths, the grafted and matrix chains were considered to be chemically identical, that is, their segments exhibit identical interactions.

The NP cores were treated as spheres of diameter $D_{\text{c}} = 6\sigma$ constructed out of a rigid simple cubic lattice of "atoms" (Fig. 2.2c). The total van der Waals (vdW) interactions between two NP cores was then calculated as the sum of individual vdW interactions between pairs of atoms *across* the two NP cores with each interaction treated using the Lennard-Jones (LJ) potential

$$U_{\text{LJ}} = 4\varepsilon_{\text{c}}\left[\left(\frac{\sigma_{\text{c}}}{r}\right)^{12} - \left(\frac{\sigma_{\text{c}}}{r}\right)^6\right],$$ (2.3)
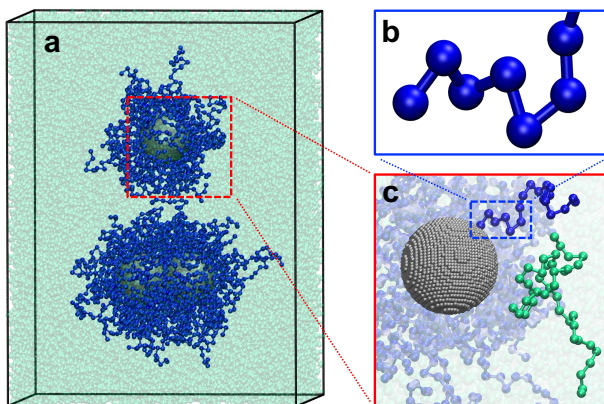
Figure 2.2: (a) Schematic of the simulation setup used for computing 3-particle PMFs between polymer-grafted NPs within a polymer matrix. (b,c) Grafted polymer chains (blue) and matrix chains (green) are treated as coarse-grained bead-chains. NP cores (gray) are treated as spheres constructed from a rigid simple-cubic lattice of atoms.

where r is the distance between the interacting atoms, and σ_c and ε_c are the atomic size and energy parameters, respectively. Such atom-level treatment of NP cores allows us to accurately capture the variation in the vdW interactions between NPs as a function of their separation distance; note that an analytical expression for such interactions between spheres is available for only very short or very large distances. The precise values of the lattice constant and atom size are not important as long as they are sufficiently small to minimize discretization (faceting) effects. We found that lattice constant λ and atom size σ_c set equal to 0.35σ yielded reasonably isotropic energies, with less than 10% variation in the total vdW energy across different orientations of the NP cores. The strength of vdW interactions can also be conveniently tuned by varying the value of ε_c. To calculate the surface-to-surface distance d between NP cores, we define their "surface" as the smallest spherical surface that encloses all their atoms, accounting for their vdW radii σ_c. Because the NP cores are rigid and near-isotropic, the interaction potential energy between two NP cores is a function of only their surface-to-surface separation distance. The potential energy profile therefore needs to be computed and tabulated just once before the MD simulations, which allowed us to avoid the use of a LJ cutoff that is typically employed in simulations.

The grafted chains were attached to the surface of each NP core also using FENE springs

(Eq. (2.1)). The grafting points were generated at the desired grafting density Γ_g using an algorithm [81, 82] that yields a pseudo-uniform distribution of points on the surface of each NP core. The grafting points were treated as virtual beads, and held fixed relative to each other and to their NP core center by using rigid body constraints. Excluded volume interactions between NP cores and the polymer segments were also treated via a short-range, purely repulsive potential

$$
U_{\text{shift-LJ}} \quad = \quad
\begin{cases}
4\varepsilon \left[\left(\frac{\sigma}{r - r_{\text{ev}}} \right)^{12} - \left(\frac{\sigma}{r - r_{\text{ev}}} \right)^{6} + \frac{1}{4} \right] & r - r_{\text{ev}} \leqslant 2^{1/6}\sigma \\
0 & r - r_{\text{ev}} > 2^{1/6}\sigma
\end{cases}
, \qquad (2.4)
$$

where r is the distance between the centers of the interacting NP and the polymer segments and the distance shift of $r_{\text{ev}} = (D_c - \sigma)/2$ ensured that the polymer segments and NP cores did not penetrate each other.

All simulation parameters and quantities are henceforth reported in units of σ, m, and ε, which set the length, mass, and time scales, respectively.

2.2.3 Potential of Mean Force Calculations

The PMFs along each of the four reaction coordinates shown in Fig. 2.1c were computed using the so-called "blue moon ensemble" method [83, 84]. This method involves the use of constrained MD simulations to confine a molecular system defined by atomic coordinates $\mathbf{r}^N$ to a sub-ensemble in which the reaction coordinate $\xi(\mathbf{r}^N)$ is held fixed at a particular value ξ'. The PMF is calculated by thermodynamic integration of the "mean force" (the negative of the ensemble-averaged gradient of the Hamiltonian with respect to the reaction coordinate) collected from multiple such simulations conducted at different fixed values of the reaction coordinate. Accordingly, we performed MD simulations of the polymer-NP system in which the centers of the dimer NPs were held fixed and the test NP was held fixed at different positions ξ' along the examined reaction coordinate. While calculation of this mean force can become tedious for reaction coordinates that depend in a complex, nonlinear manner with atom positions,

the calculation is relatively straightforward in our systems, where it reduces to evaluating the time-average of the *component* of the true force $\mathbf{F}(\xi')$ experienced by the test NP from the reference NP or NP-dimer along the direction of the reaction coordinate, which we denote by $\langle F(\xi') \rangle$ [85, 86]. The mean forces obtained from simulations conducted at different values of ξ' were then be integrated to obtain the PMF at any position d along the reaction coordinate:

$$W(d) = W(d_0) - \int_{d_0}^{d} \langle F(\xi') \rangle \, d\xi', \tag{2.5}$$

where $W(d_0)$ is the value of the PMF value at some reference point d_0 on the reaction coordinate. Choosing d_0 to be a sufficiently large distance ensures that the test NP does not interact with the NP dimer whereupon $W(d_0) \approx 0$. We refer to the above PMF involving three NPs as "3-particle" PMFs. A similar approach was used for computing "2-particle" PMF between a test NP and an isolated or "reference" NP as a function of their surface-to-surface distance d (Fig. 2.1d). To characterize the degree of anisotropy in these interactions, we also computed the 3-body contribution to the overall 3-particle PMFs via

$$\Delta W_3(d) = W(d) - W_2(d) - W_2(d') \tag{2.6}$$

where $W_2(d)$ and $W_2(d')$ are the values of the 2-particle PMFs computed at the separation distances d and d' of the test NP from each of the two dimer NPs.

We also dissected the overall PMF into six different contributions arising from the interaction between: NP-dimer cores and test-NP core [$W_{c \to c}(d)$]; NP-dimer grafts and test-NP core [$W_{g \to c}(d)$]; NP-dimer cores and test-NP grafts [$W_{c \to g}(d)$]; NP-dimer grafts and test-NP grafts [$W_{g \to g}(d)$]; polymer matrix and test-NP core [$W_{m \to c}(d)$]; and matrix and test-NP grafts [$W_{m \to g}(d)$]. Each of these contributions were also computed via Eq. (2.5), by replacing the net force $\langle F(\xi') \rangle$ with the force component corresponding to the interaction being probed. Note that all components of the PMF *except* $W_{c\text{-}c}(d)$ involve some type of polymer-mediated

interaction. Therefore, we can categorize the total PMF into a NP core-mediated component, which we denote as $W_c(d) \equiv W_{c\text{-}c}(d)$, and a polymer-mediated component, which we denote as $W_p(d) \equiv W_{g \to c}(d) + W_{c \to g}(d) + W_{g \to g}(d) + W_{m \to c}(d) + W_{m \to g}(d)$. Note that $W_c(d)$ is simply equal to $U_{vdW}(d)$, the total vdW interactions between the atoms of the interacting NP cores.

In all 3-particle PMF calculations, the dimer NPs were held fixed with their cores contacting each other, and they were not allowed to relax to their equilibrium separation distance while the test NP was brought closer to the dimer along a reaction coordinate. This allowed us to maintain a fixed reference configuration of the NP-dimer, thereby ensuring that all variations in the PMFs observed with respect to the different parameters investigated here can be attributed solely to variations in the graft conformations with respect to these parameters and not to changes in the internal configuration of the dimer itself. Also, allowing for variations in the dimer configuration would amount to computing two-dimensional PMFs, as a function of the separation distance between the dimer NPs in addition to the position ξ' of the test NP along the reaction coordinate, which would increase the computational cost by an order of magnitude. As we demonstrate later, grafted NPs that assemble into stable dimers in this study do so with their cores almost touching each other. Hence, the PMFs computed with relaxed dimers resemble quite closely those computed using fixed dimers.

2.2.4   Molecular Dynamics Simulations

The MD simulations were carried out in the canonical ensemble using a rectangular simulation box employing periodic boundary conditions in all three directions. The box dimensions were taken to be large enough to accommodate the polymer-grafted NPs in their most spread-out configuration for the PMF calculation along each reaction coordinate; this was achieved by employing a padding of at least 2.5σ along the six directions. The NP-polymer system was simulated in a melt-like state with a density of $\rho_p \equiv n_b/V_b = 0.82$, where n_b is the total number of grafted and matrix chain segments and V_b is the volume available to these segments, i.e., volume

of the simulation box minus the volume of the NP cores. The equations of motion were integrated by using a velocity-Verlet algorithm with a time step of $\Delta t = 0.002$. A Nosé-Hoover thermostat [87] with a time constant of $\tau = 1$ was used for maintaining the temperature at $T = 1$ (in units of ε/k_B), though it should be noted that our polymer chains are largely athermal. All simulations were performed using the LAMMPS package developed by Sandia National Laboratories [88].

The simulations were initialized by placing the grafted NPs and the polymer chains in a simulation box 50–100 times larger than the required dimensions to prevent overlap amongst the chain segments and NP cores. The box was then gradually compressed in each direction until the targeted box dimension or polymer density was reached. Next, the NPs were assembled into a configuration used for initiating the PMF calculations: We slowly moved two of the NPs into the dimer configuration with their cores touching each other, i.e., their centers are D_c apart (Figs. 1 and 2), and simultaneously moved the third NP to a distance $d = d_0 \equiv 12$ along the reaction coordinate being probed, a separation distance large enough to prevent the NP from interacting with the dimer. This initialization procedure was carried out over a period of 0.2–0.5 million time steps. Thereafter, the centers of the dimer NPs were held fixed.

To compute the PMF profile, the center of the third test NP was moved in a step-wise manner along the reaction coordinate towards the NP dimer, first at steps of $\Delta\xi' = 1$ until a distance of $\xi' = 4$ was reached, and then at steps of $\Delta\xi' = 0.25$ until contact. During the mobile phase of each step, the NP center was moved at a velocity of 0.00001σ per time step until the target $\Delta\xi'$ was reached. The NP center was held fixed for a time period of 0.6 million time steps during the stationary phase of each step. The ensemble-averaged force $\langle F(\xi') \rangle$ and the ensemble averaged components of the force experienced by the test NP were computed from the last 0.5 million time steps of this stationary phase. The test NP and the dimer NPs were allowed to rotate throughout the simulations. The simulations along each reaction coordinate were repeated four times to improve accuracy and facilitate the calculation of error bars. A similar procedure was used for calculating the 2-particle PMFs. The NP centers were fixed or moved fixed using "hard" restraints implemented through the "fix move" command in LAMMPS; particles restrained in

this manner are no longer influenced by forces from adjacent particles or from the thermostat.

Since the atomic lattice comprising the cores of the test and dimer NPs and their centers are also held fixed using hard restraints in each MD simulation at fixed distance ξ', the net vdW interaction energy $U_{\mathrm{vdW}}(\xi')$, or vdW force $F_{\mathrm{vdW}}(\xi')$, between the cores remains fixed during each such simulation. This feature allows for significant computational savings because the vdW portion of the PMF $W_{\mathrm{c}}(d) \equiv U_{\mathrm{vdW}}(d)$ can be calculated separately just once before or after the simulation via Eq. (2.3); this $W_{\mathrm{c}}(d)$ can then be added back onto the portion of PMF $W_{\mathrm{p}}(d)$ arising from polymer-mediated forces that fluctuate during the simulations at fixed ξ' to yield the overall PMF $W(d)$. Furthermore, since the computed $U_{\mathrm{vdW}}(d) \propto \varepsilon_{\mathrm{c}}$, one can calculate it for the reference $\varepsilon_{\mathrm{c}} = 1$ to yield a reference $U^0_{\mathrm{vdW}}(d)$, which can then be used to obtain $U_{\mathrm{vdW}}(d)$ for any arbitrary value of ε_{c} via $U_{\mathrm{vdW}}(d) = \varepsilon_{\mathrm{c}} \times U_{\mathrm{vdW}}(d)$. This allows us to explore arbitrary strengths of core/core interaction without actually performing simulations at each of those ε_{c} values.

2.2.5   Systems and Parameters Investigated

To explore how NP interactions are affected by various attributes of the grafted NPs and the polymer matrix, we computed the PMFs for a range of NP-polymer systems listed in Table 2.1. To keep the number of systems investigated to a manageable amount, the NP core diameter was fixed at $D_{\mathrm{c}} = 6$ and the interactions mediated by the grafts and matrix chains were fixed according to Eqs. 1-4. The former ensures that the NPs are much larger than the polymer segments, consistent with most experimental systems, and the latter ensures that the grafted and matrix polymer are chemically identical and that they interact with each other and with the NP cores via excluded volume interactions. We explored the effect of four parameters considered to affect the morphology of self-assembled NP structures [77]:

- *Matrix chain length.* Four different values were examined: $L_{\mathrm{m}} = 1, 5, 20,$ and 40 (note that value 1 corresponds to a "monomeric" solvent), yielding chain radii of gyration of $R_{\mathrm{g}} = 0.5, 1.12, 2.15,$ and 3.15. This allowed us to probe four different NP-to-matrix size

Table 2.1: Details of simulation systems examined in this study.

System no.[a]	$L_g{}^b$	$L_m{}^c$	$\Gamma_g{}^d$	$n_g{}^e$	$n_m{}^{f,h}$	$V^{g,h}$
				Reference system		
1[i]	20	40	0.4	45	916, 1011, 1080	47216, 52949, 56315
				Effect of polymer grafts		
1	20	40	0.4	45	916, 1011, 1080	47216, 52949, 56315
2	10	40	0.4	45	418, 471, 520	21714, 24961, 27351
3	5	40	0.4	45	138, 156, 192	7507, 8772, 10528
4	20	40	0.2	23	938, 1044, 1112	47104, 52949, 56266
5	10	40	0.2	23	430, 486, 540	21763, 24888, 27522
6	5	40	0.2	23	142, 165, 200	7434, 8809, 10516
7	20	40	0.1	11	950, 1065, 1136	47104, 53095, 56559
8	10	40	0.1	11	436, 495, 548	21763, 24888, 27473
9	5	40	0.1	11	146, 171, 204	7482, 8882, 10492
				Effect of polymer matrix		
1	20	40	0.4	45	916, 1011, 1080	47216, 52949, 56315
10	20	20	0.4	45	1832, 2022, 2160	47216, 52949, 56315
11	20	5	0.4	45	7328, 8088, 8640	47216, 52949, 56315
12	20	1	0.4	45	36640, 40440, 43200	47216, 52949, 56315
13	20	0	0.4	45	0, 0, 0	47216, 52949, 56315

[a]Index identifying the simulation system from a total of 13 studied systems. [b]Length of grafted chains. [c]Length of matrix chains. [d]Grafting density. [e]Number of grafted chains per NP. [f]Number of matrix chains in simulation box. [g]Volume of simulation box. [h]Values correspond to simulations used for computing PMFs along 2- and 3-particle ($\mathbf{x}_{0°}$, $\mathbf{x}_{90°}$) reaction coordinates; values used for computing PMFs along $\mathbf{x}'_{90°}$ are identical to those along $\mathbf{x}_{90°}$. [i]For this reference system we computed the PMF along an additional reaction coordinate ($\mathbf{x}_{45°}$) for which we employed $n_m = 1119$ and $V = 58189$.

ratios $D_c/2R_g = 0.95$, 1.4, 2.7, and 6 without altering NP size. This size ratio is known to affect the morphology of NP structures, with larger values leading to higher-dimensional structures, and is therefore also expected to affect NP/NP interactions. We *also* examined the impact of complete removal of matrix chains, that is, polymer-grafted NPs interacting in vacuum.

- *Graft chain length*. Three different chain lengths $L_g = 5$, 10, and 20 were examined, which together with variations in the grafting density described below, allow us to explore a wide

range of grafting regimes known to affect the interactions between polymer-grafted NPs.

- *Grafting density*. Three different values $\Gamma_g = 0.1$, 0.2 and 0.4 were examined. To characterize the conformation of the grafts, we computed the dimensionless surface coverage parameter $\Gamma_g^* \equiv \Gamma_g R_g^{*2}$, where R_g^* is the unperturbed radius of gyration of the grafts (free chains not grafted to NP surface) [78]. Our calculations indicate that we explored conformations ranging from the mushroom regime ($\Gamma_g^* = 0.1$) to the dilute brush regime ($\Gamma_g^* = 1.85$).

- *NP core/core interaction strength*. This is dictated solely by the magnitude of the energy parameter ε_c. As explained earlier, we can explore potentially any arbitrary value of ε_c for every combination of L_m, L_g, and Γ_g investigated here (Table 2.1) without performing any additional simulations. In general, we considered values of ε_c in the range 0.5 to 3 that allowed us explore both stable and unstable configurations of associated NP clusters.

In all systems studied here, the grafted and matrix polymer chains are chemically identical and modeled using FENE bonds and short-ranged, purely repulsive non-bonded interactions. In this study, we refrained from exploring attractive non-bonded interactions and also studying systems with chemically different NP-grafts and matrix chains. Examining such effects would entail significantly higher computational costs, not only due to the slower conformational sampling of attractive systems via MD simulations, but also due to the introduction of additional parameters in the system associated with graft-graft, graft-matrix, and matrix-matrix interactions. It was recently shown that replacing the repulsive non-bonded potential in the above model with an attractive Lennard-Jones potential had negligible effect on the structure and dynamics of polymer chains simulated at melt-like densities and temperatures at least twice as large as the glass transition temperature T_g [89]. Thus, we do *not* expect the introduction of uniformly attractive interactions across grafted and matrix polymer chains to have any significant effect on computed PMFs given that we performed our simulations in the melt phase at $T = \varepsilon/k_B$, much higher than T_g ($\sim 0.4\varepsilon/k_B$). However, differences in interactions amongst and between grafts

and matrix chains should affect the PMFs; for instance, if the matrix-graft interactions were attractive while the graft-graft and matrix-matrix interactions were repulsive, then one would expect the grafted-NPs to exhibit less attraction (or more repulsion) with each other as compared to systems with chemically identical grafts and matrix chains.

2.3   Results and Discussion

2.3.1   Anisotropy in NP Interactions

To determine if and how the interactions between two polymer-grafted NPs become anisotropic when a third NP is in close proximity to one of the NPs, we computed using molecular dynamics (MD) simulations the potential of mean force (PMF) between a test NP and a NP-dimer along four distinct reaction coordinates spanning the angular space around the dimer. Though we computed such PMFs for a range of NP-polymer systems, we present below results computed for one representative system comprising of NPs grafted with polymer chains of length $L_m = 40$ at a grafting density of $\Gamma_g = 0.4$ surrounded by a polymer matrix of chain length $L_g = 20$ (Table 2.1, system 1). As discussed later, this system with long and dense NP-grafts displays strong anisotropic interactions, making it an ideal system for showcasing this phenomenon and elucidating its physical basis.

Figures 3a and 3b show the core- and polymer-mediated components $W_c(d)$ and $W_p(d)$ of the overall PMF computed along the four chosen reaction coordinates. For comparison, we also plot for the same system the two components of the 2-particle PMF. The core-mediated component $W_c(d)$ scales linearly with the LJ energy parameter ε_c of the NP-core atoms and is thus plotted in units of ε_c (Fig. 2.3a). As expected, this component is always attractive for distances $d > 0$ where all core atoms interacting across the test and dimer NPs are separated by a distance greater than σ_c. At smaller distances $d < 0$, some of these atoms begin to overlap and W_c rises and becomes repulsive. All $W_c(d)$ exhibit a minimum close to contact, at roughly
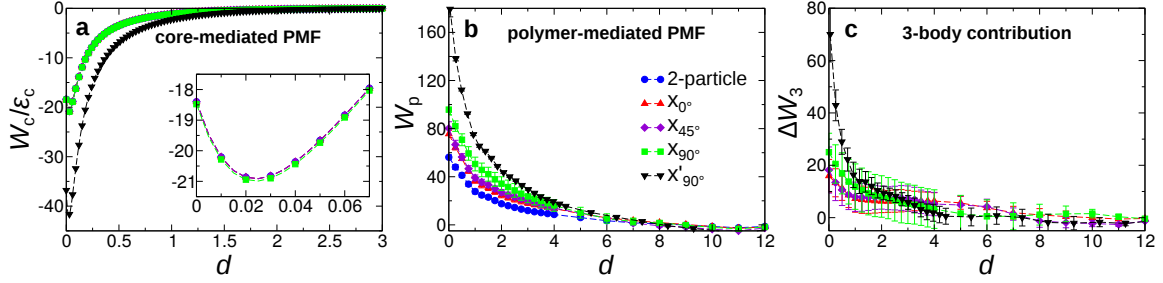
Figure 2.3: (a-b) Core and polymer-mediated components of the overall PMF computed along the 2- and the 3-particle reaction coordinates for the representative NP-polymer system with $L_g = 20$, $\Gamma_g = 0.4$, and $L_m = 40$. (a) Core-mediated component normalized by interatomic energy parameter ε_c. Inset shows closeup of the profiles at small d. (b) Polymer-mediated component. (c) 3-body contribution to the overall PMF.

$d = 0.024\sigma$, which is consistent with notion that the NP cores can further lower their vdW energy by getting closer than $d = (2^{1/6} - 1)\sigma_c \equiv 0.043\sigma$ (location of the energy minimum for the interaction between the closest pair of atoms on different cores directly facing each other) to increase favorable interactions between the remaining atoms of the interacting cores. The 3-particle $W_c(d)$ profiles along all reaction coordinates *except* $\mathbf{x}'_{90°}$ are almost identical to the profile obtained for the 2-particle configuration. The reason is that the LJ interaction between the NP-core atoms is short-ranged and none of these reaction coordinates allow the test NP to simultaneously contact both NPs of the dimer. Each of these profiles exhibit an attractive well whose depth scales as $\approx 21\varepsilon_c$. The $W_c(d)$ profile along $\mathbf{x}'_{90°}$ is exactly twice in magnitude to that of the 2-particle PMF given that the test NP now feels exactly the same attraction from both NPs of the dimer, which also implies that the 3-body contribution ΔW_3 is exactly zero, as expected for rigid cores. Also as expected, the 3-body contribution to the $W_c(d)$ for the remaining three profiles is zero as well.

The polymer-mediated PMF component $W_p(d)$, on the other hand, are all repulsive and decrease much slower than $W_c(d)$ with increasing separation distance d (Fig. 2.3b). By $d \sim 7$–8, the polymer grafts of the interacting NPs are out of reach of each other and W_p approaches zero. Importantly, the $W_p(d)$ profiles for the 3-particle PMFs are substantially more repulsive than that of the 2-particle PMF. More importantly, the polymer-mediated repulsion displays large variation

across the four reaction coordinates. In particular, the degree of repulsion increases in the order $\mathbf{x}_{0°} < \mathbf{x}_{45°} < \mathbf{x}_{90°} < \mathbf{x}'_{90°}$. Thus, while $W_c(d)$ is largely independent of the orientation of the test NP with respect to the NP dimer, except for the sharp enhancement close to the perpendicular axis of the dimer, $W_p(d)$ shows a more uniform increase with the orientation angle away from the poles of the NP dimer.

In Fig. 2.3c, we have plotted the 3-body contribution ΔW_3 to the overall PMF, which arises completely from polymer-mediated interactions, as the core-mediated PMF does not have any 3-body contribution. We find that ΔW_3 is substantial and contributes 30–40 % of the overall polymer-mediated repulsion (W_p) at near-contact $d \approx 0$, and as expected, this contribution becomes smaller with further distance. Furthermore, ΔW_3 increases in the order $\mathbf{x}_{0°} < \mathbf{x}_{45°} < \mathbf{x}_{90°} < \mathbf{x}'_{90°}$ with respect to the four reaction coordinates, i.e., the 3-body contribution becomes larger as the test NP moves from the pole of the dimer ($\theta = 0$) to the contact point of the two dimer NPs ($\theta \approx 4\pi/3$; see Fig. 2.1a).

Fig. 2.4 shows the overall 3-particle PMF $W(d)$ for two representative values of the energy parameter ($\varepsilon_c = 3$ and 7) depicting intermediate and strong core-core attraction; Note that for much smaller or much larger values of ε_c, $W(d)$ converge to $W_p(d)$ and $W_c(d)$, respectively. Compared to the two components, the overall PMFs exhibit a more complex dependence with distance and reaction coordinate. First, for sufficiently strong core/core attraction, the overall PMFs exhibit an energy barrier at short distances, which separates the stable (or metastable) bound state of the test NP from its dispersed state. The height of this energy barrier depends on the strength of the core-core attraction. Second, the overall PMFs no longer necessarily exhibit monotonic variations in the strength of attraction (or repulsion) with orientation as exhibited by $W_p(d)$ and $W_c(d)$. For example, the most stable bound state of the test NP occurs along the $\mathbf{x}'_{90°}$ coordinate when $\varepsilon_c = 7$, whereas it occurs along $\mathbf{x}_{0°}$ when $\varepsilon_c = 3$. Indeed, it is such variations in the relative stability of the different bound states of NPs that leads to the rich and complex phase behavior exhibited by polymer-grafted NPs, as discussed in more detail further below. Interestingly, all PMFs $W(d)$ that exhibit an energy minimum do so at a distance close to the
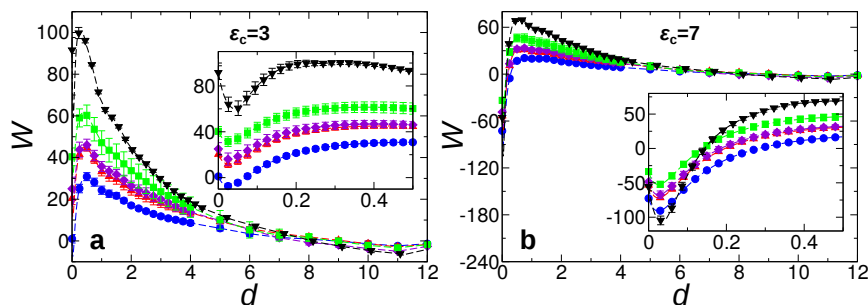
Figure 2.4: Overall PMFs computed along the 2- and the 3-particle reaction coordinates for the representative NP-polymer system with $L_g = 20$, $\Gamma_g = 0.4$, and $L_m = 40$. The PMFs have been computed for (a) $\varepsilon_c = 3$ and (b) $\varepsilon_c = 7$. Insets show closeups at small d.

location of the minimum exhibited by the core-mediated PMF $W_c(d)$. This observation is not surprising given the sharp, shorter-ranged decay of the vdW core/core attraction as compared to the flatter, longer-ranged decay of polymer-mediated repulsion, which causes the cores to position themselves close to each other to take advantage of the strong vdW attraction without sacrificing much steric repulsion.

The overall PMFs also importantly reveal that the dimer NPs prefer to assemble with their cores almost touching each other ($d \approx 0.024\sigma$), very similar to the contact configuration ($d = 0$) we used for computing 3-particle PMFs. Given that this difference in the dimer configuration is much smaller than even the size of a single polymer segment (σ), we expect the 3-particle PMFs computed here to closely approximate the "true" 3-particle PMFs obtained from calculations in which the dimers are allowed to relax. To confirm this, we conducted additional simulations to compute the 3-particle $W_p(d)$ with dimer NPs separated by 0.024σ. Our results plotted in Sup. Fig. 2.13 showed that the PMFs are very close to each other.

2.3.2 Monomer Density Distribution

It was previously proposed [72, 73, 77] that the anisotropic assembly of spherical grafted NPs could putatively arise from the displacement of polymer grafts from in between the interacting NPs, potentially leading to anisotropic distribution of polymer chains around the NPs. To investigate if the observed anisotropy in the overall polymer-mediated repulsion $W_p(d)$, and in

its 3-body contribution $\Delta W_3(d)$ (Fig. 2.3b,c) is related to any such changes in polymer density, we computed the position-dependent segmental density around a NP-dimer, defined here as the number of polymer chain segments (beads) per unit volume. For this purpose, we carried out separate MD simulations of the NP-dimer in the same polymer matrix, *but* without the test NP, and computed three kinds of densities: the *overall* segmental density $\rho_{g+m}(x,r)$ (Fig. 2.5a) arising from both grafted and matrix chains, the *graft* segmental density $\rho_g(x,r)$ (Fig. 2.5b) arising from grafted chains alone, and the *matrix* segmental density $\rho_m(x,r)$ (Fig. 2.5c) arising from matrix chains alone, each of which were computed as a function of the longitudinal (x) and radial coordinate (r) relative to the NP dimer. To more directly relate these densities to the computed $W_p(d)$ and $\Delta W_3(d)$, we also obtained 1D segmental density profiles $\rho_{g+m}(r')$ (Fig. 2.5d), $\rho_g(r')$ (Fig. 2.5e), and $\rho_m(r')$ (Fig. 2.5f) as a function of the radial distance r' to the center of the dimer NP(s) along the reaction coordinates introduced earlier. Because W_p (and $\Delta W_3(d)$) and the density profile along $\mathbf{x}_{45°}$ are only marginally different from that along $\mathbf{x}_{0°}$, we present only the density profiles along the three reaction coordinates $\mathbf{x}_{0°}$, $\mathbf{x}_{90°}$, and $\mathbf{x}'_{90°}$. For comparison, we also computed the density profile around a single NP computed from a separate MD simulation of an isolated NP in a polymer matrix.

The overall segmental density shows enhancement and oscillations close to the surface of the dimer (Fig. 2.5a) that are more apparent in the $\rho_{g+m}(r')$ profiles (Fig. 2.5d). This behavior is caused by a combination of two effects: the tethering of the terminal graft segment to the NP core and the layering of particles (segments) with excluded volume next to an impenetrable wall (NP cores). Sufficiently far from the dimer surface ($> 3\sigma$), the densities asymptote to the bulk density. More importantly, we observe minimal variations in $\rho_{g+m}(x,r)$ around either of the two dimer NPs with respect to the angular coordinate. In particular, $\rho_{g+m}(r')$ profiles along the three reaction coordinates $\mathbf{x}_{0°}$, $\mathbf{x}_{90°}$ and $\mathbf{x}'_{90°}$ all remain similar to the density profile obtained for the isolated NP. These results indicate that the observed anisotropy in polymer-mediated repulsion between NPs might *not* arise from any enhancement in the overall segmental density near the contact region of the dimer.
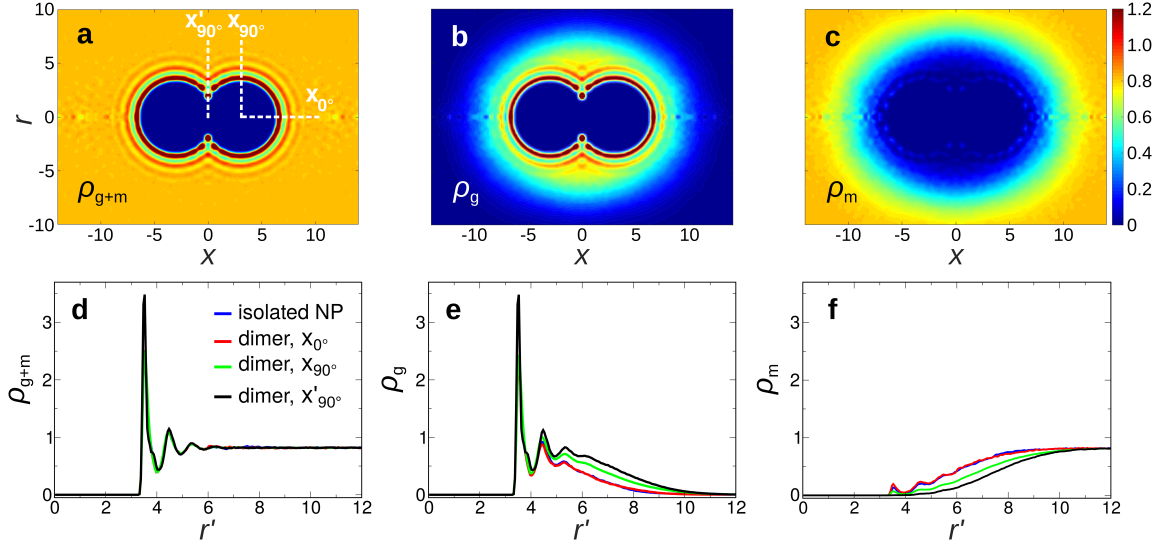
Figure 2.5: 2D contour maps of (a) overall segmental density $\rho_{g+m}(x,r)$, (b) graft segmental density $\rho_g(x,r)$, and (c) matrix segmental density $\rho_m(x,r)$ surrounding the NP-dimer. Color bars denote the density magnitude in units of segments/σ^3. (d) Overall segmental density $\rho_{g+m}(r')$, (e) graft segmental density $\rho_g(r')$, and (f) matrix segmental density $\rho_g(r')$ profiles along the three reaction coordinates labeled in (a) plotted as a function of radial distance r' from the center of the dimer NP. The "reference" density profile around an isolated NP as a function of radial distance from its center is shown in blue.

The segmental density associated with grafts only, in contrast, displays strong anisotropy, as noted from the angle-dependence of $\rho_g(x,r)$ (Fig. 2.5b) or from differences in $\rho_g(r')$ across the three reaction coordinates (Fig. 2.5e). In particular, the region around the dimer that displays high to moderate density ($\rho_g \gtrsim 0.4$), as depicted by the green-cyan halo in Fig. 2.3b, extends farther into the matrix along the perpendicular than the longitudinal coordinate. The $\rho_g(r')$ profiles show that the density rises monotonically from the dimer poles to the contact region, i.e., in the order $\mathbf{x}_{0°} < \mathbf{x}_{90°} < \mathbf{x}'_{90°}$ (Fig. 2.5e). These results suggest that when two NPs come into contact, as in the case of the dimer, their intervening grafts get pushed outwards into the region immediately surrounding the contact point, causing a strong enhancement in the graft segmental density along the perpendicular axis passing through the contact point. The displaced grafts encroach on their neighboring grafts, causing them to extend outwards and sideways, triggering a "domino effect" that propagates outwards from the contact point to the dimer poles. That the density along $\mathbf{x}_{0°}$ is only slightly higher than that for a single NP (Fig. 2.5e) indicates that the

propagation eventually subsides, with the grafts at either of the two dimer poles remaining mostly unaffected by the presence of the other dimer NP. We also observe that the $\rho_g(r')$ profiles along the three reaction coordinates increase in the same sequence as the 3-particle $W_p(r')$ profiles and that the $\rho_g(r')$ profile along $\mathbf{x}_{0°}$ is only slightly higher than its 2-particle counterpart, also similar to $W_p(r')$ (see Fig. 2.3b). This close analogy between $W_p(r')$ and $\rho_g(r')$ suggests that the anisotropy in polymer-mediated PMFs may be caused by the anisotropy in the graft segmental density, thereby providing direct support for the hypothesis that the anisotropic interactions between NPs could indeed arise from the conformational rearrangement of grafted chains at the contact region.

Lastly, the segmental density arising from the matrix chains shows the opposite trends compared to those exhibited by the density arising from the grafts. In this case, $\rho_m(x,r)$ gets increasingly depleted as one gets closer to the dimer surface, evidently due to increased exclusion by the polymer grafts. Also, the depletion of matrix chains is most severe along $\mathbf{x}'_{90°}$ and gets weaker as one rotates towards the dimer axis, the $\mathbf{x}_{0°}$ coordinate. As discussed below, this anisotropy in the depletion of matrix chains around the dimer will lead to an anisotropy in the depletion forces between test NP and the dimer.

2.3.3   Steric versus Depletion Interactions

Polymer-mediated interactions between grafted NPs in a polymeric matrix arise from a combination of steric repulsion due to compression of the grafted chains and depletion attraction due to osmotic pressure of the matrix chains. To evaluate the role of steric and depletion forces in producing the anisotropic polymer-mediated repulsion between NPs, we dissected $W_p(d)$ into components arising from the interactions between: (1) NP-dimer grafts and test-NP grafts, $W_{g \to g}(d)$; (2) dimer cores and test-NP grafts, $W_{c \to g}(d)$; (3) dimer grafts and test-NP core $W_{g \to c}(d)$; (4) polymer matrix and test-NP grafts $W_{m \to g}(d)$; and (5) polymer matrix and test-NP core $W_{m \to c}(d)$. The first three components involving the polymer grafts of the test or dimer NPs
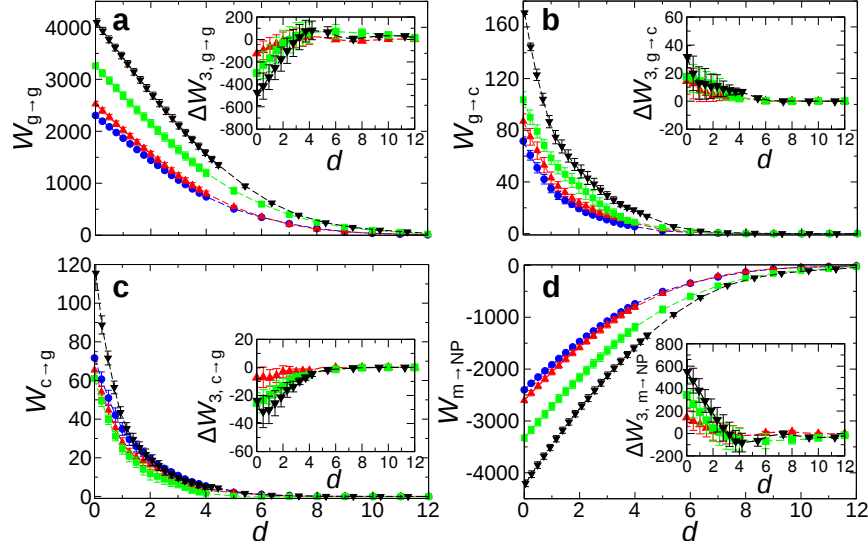
Figure 2.6: Breakdown of the net polymer-mediated repulsion W_p into its four components: $W_{g\to g}$, (b) $W_{g\to c}$, (c) $W_{c\to g}$, and (d) $W_{m\to NP}$. Each component is plotted as a function of position d along the 2- and 3-particle reaction coordinates. The insets provide the 3-body contributions for each of these components.

constitute "steric" interactions, while the last two components arising from the polymer matrix constitute "depletion" interactions.

We begin by examining how these individual components vary with respect to the reaction coordinate. Incidentally, the computed $W_{m\to c}(d)$ were substantially smaller than $W_{m\to g}(d)$ and had a large statistical uncertainty, which made it difficult to glean any statistically significant trends. To this end, we combined both these matrix-centered terms into a single term that we denote by $W_{m\to NP}(d)$ corresponding to the net depletion force acting on the *entire* test NP. Figure 2.6 shows the four components $W_{g\to g}(d)$, $W_{c\to g}(d)$, $W_{g\to c}(d)$, and $W_{m\to NP}(d)$ corresponding to the 2-particle PMF and the 3-particle PMFs along $\mathbf{x}_{0°}$, $\mathbf{x}_{90°}$, and $\mathbf{x}'_{90°}$. The insets provide the 3-body contributions $\Delta W_{3,g\to g}(d)$, $\Delta W_{3,g\to c}(d)$, $\Delta W_{3,c\to g}(d)$, and $\Delta W_{3,m\to NP}(d)$ for each of these four interactions along $\mathbf{x}_{0°}$, $\mathbf{x}_{90°}$, and $\mathbf{x}'_{90°}$.

The PMF component $W_{g\to g}(d)$ arising from graft-graft interactions (Fig. 2.6a) is found to be extremely repulsive, approaching 1000s of $k_B T$ at contact ($d = 0$). Decomposing $W_{g\to g}(d)$ further into its energetic and entropic contributions using an approach described elsewhere [86]

(Sup. Fig. 2.14) reveals that most of this repulsion arises from the huge entropic loss incurred by the grafts that get increasingly squeezed in between the NP cores as they approach each other. Furthermore, the repulsion is stronger for the 3-particle configurations and increases in the order $\mathbf{x}'_{0°} < \mathbf{x}_{90°} < \mathbf{x}'_{90°}$, with the former approaching the 2-particle $W_{g \to g}$. Clearly, the strong enhancement in graft segmental density along $\mathbf{x}'_{90°}$ (Fig. 2.5b,e) is responsible for the strong graft-graft repulsion along this reaction coordinate. The smaller enhancements along $\mathbf{x}_{90°}$ and $\mathbf{x}_{0°}$ leads to concomitantly smaller degrees of repulsion along those reaction coordinates. Interestingly, the 3-body contributions to graft-graft repulsion are all negative (attractive), suggesting that the cumulative graft-graft repulsion arising from the two dimer NPs in isolation is stronger than that arising from the dimer. This result is likely related to the cumulative graft segmental density arising from two isolated dimer NPs being much higher than that from the dimer (see Fig. 2.5e), which despite the anticipated stronger-than-linear dependence of steric repulsion with graft segmental density, leads to stronger graft/graft repulsion. In addition, the 3-body contributions are found to become increasingly negative in the order $\mathbf{x}'_{0°}$, $\mathbf{x}_{90°}$, and $\mathbf{x}'_{90°}$.

The two components $W_{g \to c}(d)$ and $W_{c \to g}(d)$ arising from interactions between NP grafts and cores are also purely repulsive, but more than an order of magnitude weaker than $W_{g \to g}(d)$ due to the strong shielding of NP cores by their grafts (Figs. 6b and 6c). Similar to $W_{g \to g}(d)$, the $W_{g \to c}(d)$ repulsion also increases in the order $\mathbf{x}_{0°} < \mathbf{x}_{90°} < \mathbf{x}'_{90°}$ with the repulsion along $\mathbf{x}_{0°}$ approaching that in the 2-particle configuration. This trend is expected given that the graft segmental density around the dimer NPs also increases in the same sequence, leading to more interactions between the dimer grafts and the test NP core along the two perpendicular directions as compared to the longitudinal direction. However, $W_{c \to g}(d)$ exhibits a somewhat different trend in that the repulsion along $\mathbf{x}_{0°}$ is weaker than that for the 2-particle configuration, and becomes even weaker along $\mathbf{x}_{90°}$. The reason is that the increasing graft segmental density along $\mathbf{x}_{0°}$ and then $\mathbf{x}_{90°}$ shields the dimer NP core from interacting with the test NP grafts. Interestingly, the repulsion rises up again along $\mathbf{x}'_{90°}$ because both dimer cores are now able to interact with the grafts of the test-NP. The 3-body contributions to $W_{g \to c}(d)$ are all positive. The positive

contribution arises from the enforced interactions of polymer grafts from the dimer with the surface of the test NP core due to their inability to escape from the tight confinement in between the test and dimer NPs. Comparatively, polymer grafts from isolated dimer NPs have much more freedom to get displaced. In contrast, the 3-body contributions to $W_{c\rightarrow g}(d)$ are all negative, which is likely due to the increased cumulative ability of test NP grafts to interact with the surface of the dimer NPs when isolated as compared to the dimer that excludes a large fraction of the dimer NPs from interacting with the grafts. As usual, the magnitude of the 3-body terms for both these interactions increase in the order $\mathbf{x}_{0^\circ} < \mathbf{x}_{90^\circ} < \mathbf{x}'_{90^\circ}$.

The last component $W_{m\rightarrow NP}(d)$ due to depletion interactions is strongly attractive (Fig. 2.6d). The main source of this attraction is the difference in the osmotic pressure that develops across the two halves of the test NP (facing toward and away from the dimer) due to exclusion of matrix chains from in between the test NP and the dimer. This component is so strong that it almost counterbalances the graft-graft repulsion. In addition, the magnitude of depletion attraction increases in the order $\mathbf{x}_{0^\circ} < \mathbf{x}_{90^\circ} < \mathbf{x}'_{90^\circ}$ with the former approaching the 2-particle $W_{m\rightarrow NP}(d)$. This trend is consistent with that of the graft segmental density in the region in between the test and dimer NPs (Fig. 2.5b,d), which rises in the same order with respect to the reaction coordinates, leading to increasing exclusion of the matrix chains from this region, and thereby higher depletion attraction. The 3-body contributions to depletion attraction are all positive. This can be explained in terms of the overlap between the excluded volumes of the test NP and NP dimer being smaller than the sum of the overlaps between the excluded volumes of the test NP and the dimer NPs individually. The magnitude of 3-body contributions again increase in the order $\mathbf{x}'_{0^\circ}$, $\mathbf{x}_{90^\circ}$, and $\mathbf{x}'_{90^\circ}$.

The rise in polymer-mediated repulsion $W_p(d)$ with increased tilting of the reaction coordinate from the dimer longitudinal axis may now be explained in terms of a competition between the net steric repulsion $W_{ster} \equiv W_{g\rightarrow g} + W_{g\rightarrow c} + W_{c\rightarrow g}$ and depletion attraction $W_{depl} \equiv W_{m\rightarrow NP}$. Figure 2.7a compares the net steric repulsion against depletion attraction for the 2- and 3-particle configuration. While both interactions become stronger with increased tilting
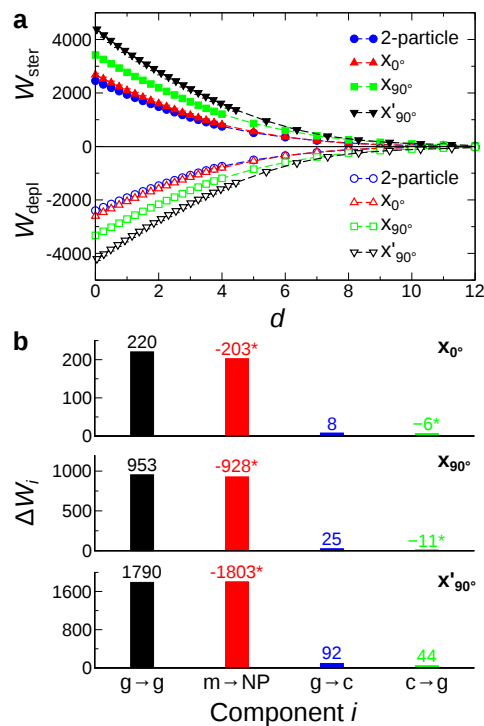
Figure 2.7: (a) Comparison of the net steric repulsion and depletion attraction experienced by the test NP along the 2- and 3-particle reaction coordinates. The two components nearly cancel each other and the resulting PMF $W(d) = W_{\text{ster}}(d) + W_{\text{depl}}(d)$ for the different reaction coordinates are shown in Fig. 2.3b. (b) Bar-chart of the differences $\Delta W_i|_j \equiv W_i(0)|_{\text{3-particle},j} - W_i(0)|_{\text{2-particle}}$ in the values (specified above each bar) of the four PMF components $i \equiv$ g→g, m→NP, g→c, and c→g between the 3- and the 2-particle configurations, calculated for each of the reaction coordinates $j \equiv \mathbf{x}_{0°}, \mathbf{x}_{90°}, \mathbf{x}'_{90°}$ at contact ($d = 0$).

of the reaction coordinate, as explained above in terms of the gradient in the graft segmental density from dimer contact point to poles, the increase in steric repulsion always exceeds that in depletion attraction, causing an increased net repulsion with increased tilting of the reaction coordinate; A possible explanation for this observation is provided further below.

To further evaluate the contribution of the three components of steric repulsion $W_{\text{g}\rightarrow\text{g}}$, $W_{\text{g}\rightarrow\text{c}}$, and $W_{\text{c}\rightarrow\text{g}}$ to the increase in overall repulsion with tilting of the reaction coordinate, we calculated the difference $\Delta W_i|_j \equiv W_i(0)|_{\text{3-particle},j} - W_i(0)|_{\text{2-particle}}$ in the value of the four PMF components $i \equiv$ g→g, g→c, c→g, m→NP *between* the 3- and the 2-particle configurations; These differences were calculated for each of the three reaction coordinates $j \equiv \mathbf{x}_{0°}, \mathbf{x}_{90°}, \mathbf{x}'_{90°}$ at the contact distance $d = 0$, where the repulsion $W_{\text{p}}(d)$ is the strongest. This analysis, presented in

Fig. 2.7b, reveals that the stronger repulsion $W_p(d)$ along $\mathbf{x}_{0°}$ (compared to the 2-particle scenario) (Fig. 2.3b) occurs primarily due to the increase in the steric repulsion between grafts (Fig. 2.7b, top panel) overriding the corresponding increase in depletion attraction. The corresponding changes in the remaining two components—graft-to-core and core-to-graft repulsion—are smaller and in opposite directions, and effectively cancel each other out. However, this is not the case for repulsion along $\mathbf{x}_{90°}$, where the increase in graft-to-core repulsion is larger in magnitude than the decrease in the core-to-graft repulsion (middle panel). The residual repulsion from core-graft interactions, combined with the stronger graft-graft repulsion versus depletion attraction, as in the case of $\mathbf{x}_{0°}$, leads to even stronger repulsion along $\mathbf{x}_{90°}$ as compared to $\mathbf{x}_{0°}$ (Fig. 2.3b). The situation is entirely different for the repulsion along $\mathbf{x}'_{90°}$. Here, the increase in graft-to-graft repulsion is more than counterbalanced by the depletion attraction and the core-to-graft repulsion now increases instead of decreasing as in the case of $\mathbf{x}_{0°}$ and $\mathbf{x}_{90°}$ (bottom panel). Moreover, the core-to-graft and graft-to-core repulsion are both fairly strong and become the primary contributors to the very strong repulsion observed along $\mathbf{x}'_{90°}$.

2.3.4   Effects of Polymer Grafts and Surrounding Matrix

To gain further insight into the influence of polymer grafting on the anisotropic interactions between the NPs, we extended our study to additional NP-polymer systems differing in the grafting density and/or graft length. Specifically, we examined nine different systems (Table 2.1, systems 1–9), resulting from combining three different grafting densities ($\Gamma_g = 0.1$, 0.2, and 0.4) and three different graft lengths ($L_g = 5$, 10, and 20), that includes the representative system with $\Gamma_g = 0.4$ and $L_g = 20$ discussed so far. Figure 2.8 compares the polymer-mediated repulsion $W_p(d)$ computed for these systems along $\mathbf{x}_{0°}$, $\mathbf{x}_{90°}$, and $\mathbf{x}'_{90°}$. We find that the repulsion is very strong and differs significantly between the three reaction coordinates for large values of Γ_g and L_g. As these grafting parameters become smaller, the repulsion weakens and the $W_p(d)$ profiles for the three reaction coordinates become increasingly similar to each other. In other words, the

Figure 2.8: Polymer-mediated component of the PMF computed along the 2- and 3-particle reaction coordinates for nine distinct NP-polymer systems differing in NP graft length ($L_g = 5$, 10, 20) or grafting density ($\Gamma_g = 0.1, 0.2, 0.4$). Insets show the corresponding 2D contour maps of graft segmental density surrounding an isolated dimer (scale bar = 6σ).

polymer-mediated repulsion is strongly anisotropic for long grafts and high grafting densities and becomes more isotropic as the grafts become shorter and more sparsely grafted. To further characterize this anisotropy as a function of graft length and grafting density, we computed the 3-body contributions $\Delta W_3(d)$ for four of these NP-polymer systems differing in graft length and grafting density. Our results plotted in Fig. 2.3 indicate that the interactions become increasingly anisotropic with increasing graft length and grafting density. In fact, for the lowest grafting density studied here ($\Gamma_g = 0.1$), the 3-body contributions are negligible, even for relatively long grafts (Fig. 2.9c,d).

The observed reduction in anisotropy with decreasing graft length and grafting density is easily explained from the graft segmental density maps $\rho_g(x,r)$ (Fig. 2.8 insets): When either
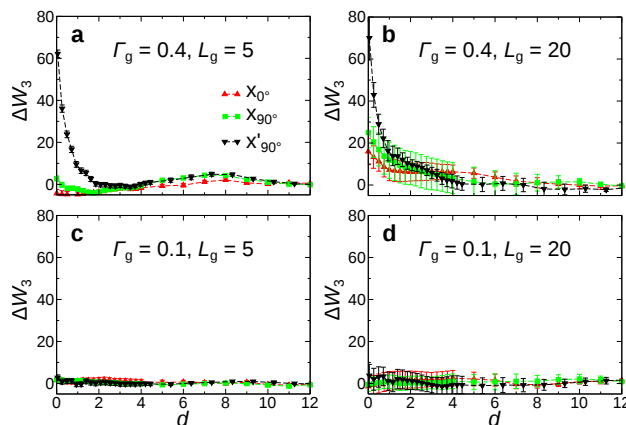
Figure 2.9: 3-body contribution $\Delta W_3(d)$ for four different NP-polymer systems differing in graft length and grafting density as specified in the figures along $\mathbf{x}_{0°}$, $\mathbf{x}_{90°}$, and $\mathbf{x}'_{90°}$.

of the two grafting parameters is reduced, the high-density region depicted by the yellow-cyan halo around the NP cores changes from an anisotropic elliptical shape to a more isotropic shape that closely "hugs" the dimer surface. The strong correlation between the density contours and the PMFs reemphasizes the strong connection between anisotropy and graft segmental density. As expected, the overall segmental density (Sup. Fig. 2.15) remains almost identical across all systems, again confirming the little-to-no correlation between anisotropy and overall segmental density. Dissecting $W_p(d)$ into steric and depletion contributions (Sup. Fig. 2.16) reveals that both components are substantial for systems with high grafting density and long grafts, and that the dominance of steric repulsion over depletion attraction results in strong polymer-mediated repulsion and large differences in the repulsion over the three reaction coordinates. As the grafting density and/or graft lengths become smaller, both components become weaker, leading to weaker overall repulsion and smaller differences in repulsion between the different reaction coordinates.

Our calculations have shown that the matrix chains produce strong depletion attraction between the NPs that negates much of the steric repulsion between them (Fig. 2.7a). To further investigate the impact of the surrounding medium on the polymer-mediated repulsion between NPs, we examined the effects of replacing the matrix chains, currently of length $L_m = 40$, with
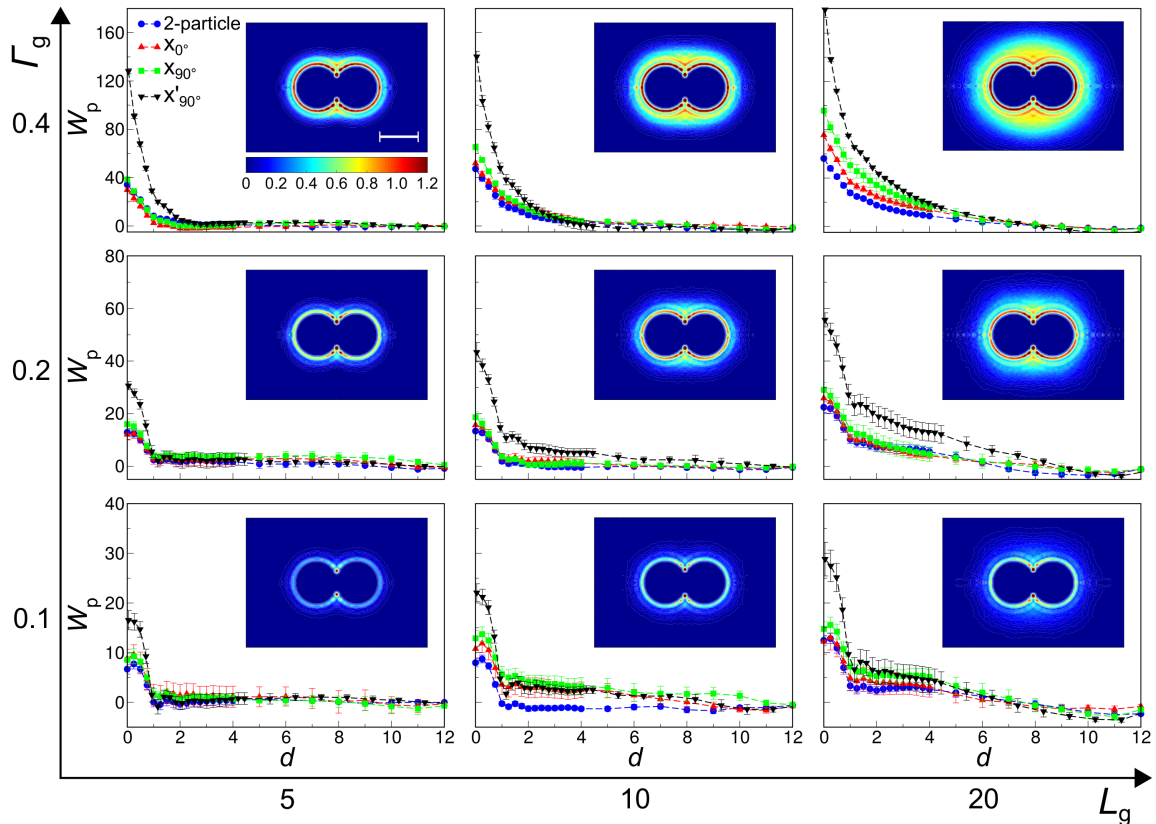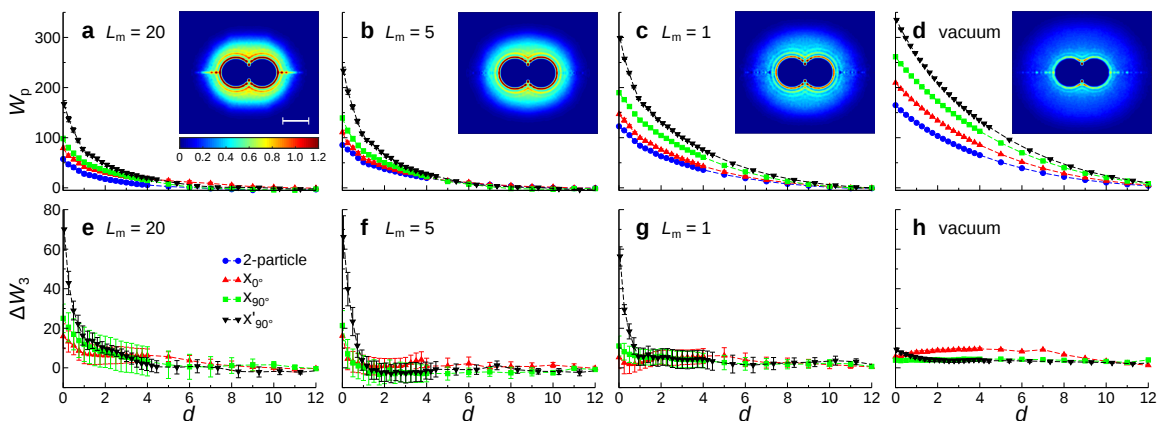
Figure 2.10: Polymer-mediated component of the PMF computed along the 2- and 3-particle reaction coordinates for NPs interacting across a polymer matrix of chain length (a) $L_m = 20$, (b) $L_m = 5$, (c) $L_m = 1$, and (d) $L_m = 0$ (vacuum). Insets show the corresponding 2D contour maps of graft segmental density surrounding an isolated dimer (scale bar = 6σ).

shorter chains of length $L_m = 20$, 5, and 1, the last of which represents a "monomeric" solvent (Table 2.1, systems 10–12); We also examined the effect of removing the matrix altogether by considering NP interactions in vacuum (system 13). Figure 2.10 presents the $W_p(d)$ profiles computed for these new systems along $\mathbf{x}_{0°}$, $\mathbf{x}_{90°}$, and $\mathbf{x}'_{90°}$. Comparing against the profiles obtained for the reference system (Fig. 2.3b), we find that decreasing the matrix chain length to $L_m = 20$ (Fig. 2.10a) has no measurable effect on $W_p(d)$, and a further decrease to $L_m = 5$ leads to some ($\sim$40%) increase in repulsion (Fig. 2.10b). However, dissolving the bonds between the matrix chain segments ($L_m = 1$) leads to a significant increase in repulsion, roughly twice in magnitude along each reaction coordinate (Fig. 2.10c). The removal of matrix chains altogether leads to further increase in the strength of repulsion (Fig. 2.10d). We note that each increase in the strength of repulsion with chain shortening is also accompanied by an outward extension in the range of repulsion. Also plotted in Fig. 2.10 are the 3-body contributions to the PMF, which are observed to decrease with the decreasing matrix chain length (Fig. 2.10e–g) and, somewhat interestingly, become quite small when the matrix chains are removed altogether (Fig. 2.10h). Thus, the presence of a matrix surrounding the polymer-grafted NPs seems to play an important role in their enhancing 3-body interactions between them.

To investigate the origin of this increase in the strength and range of repulsion with reduction in the length of the matrix chains and their subsequent removal, we turn to the graft segmental density maps (Fig. 2.10 insets) and the steric and depletion components of $W_p(d)$ (Sup. Fig. 2.17). The density maps clearly show that the NP grafts extend outwards with the shortening and subsequent removal of matrix chains. This observation is consistent with the fact that the shorter the matrix chains, the weaker the depletion force (osmotic pressure) they exert (Sup. Fig. 2.17) and thereby the farther the grafts extend into the matrix, which explains the observed increase in the range of repulsion with decreasing length and removal of matrix chains. Such extension of grafts also leads to a sparser layer of grafted polymer segments around the dimer NPs (Fig. 2.10 insets), allowing easier interpenetration between the grafts of the test and dimer NPs. Thus, the diminishing depletion attraction with shortening and removal of matrix chains also results in smaller steric repulsion between grafts. However, this decrease in steric repulsion is smaller in magnitude than the corresponding decrease in depletion forces (Sup. Fig. 2.17), which causes increase in the overall polymer-mediated repulsion with reduction in the length of the matrix chains or their removal. Though we did not study systems with matrix chains longer than 40 due to computational reasons, we expect their PMFs to look similar to those of $L_m = 40$ given that $W_p(d)$ and $\rho_g(x, r)$ seem to have converged at this chain length, indicating that the grafted chains are close to their maximum compression. The above results underscore the importance of the surrounding medium when examining interactions between NPs and suggest that the effects of the surrounding matrix cannot be neglected, even when the matrix is neutral to the grafts, as is the case in this study.

2.3.5 Additional Insights into Depletion Interactions

The polymer-grafted NPs examined here exhibit unusually strong depletion attraction, even in a monomeric matrix where the strength of the depletion interactions is $\sim 1300 k_B T$ (Sup. Fig. 2.17). To understand the origin of such strong interactions, we turn to the classical

model of Asakura and Oosawa (AO model) [90, 91] that provides an analytical expression for the strength of depletion interactions between two spherical particles in a solution of macromolecules (depletant). The model treats both components as hard spheres and uses an ideal-gas approximation to estimate the translational entropy that the macromolecules gain from the additional volume that frees up due to the overlap between the macromolecule-excluded volumes of two particles when they come into contact. Specifically, the free energy change ΔG_d resulting from the contact of two particles of diameter D_p in a surrounding solution of volume V containing N macromolecules of diameter D_m is given by [91]

$$\Delta G_d = -\frac{N\pi k_B T D_m^2 \left(3D_p + 2D_m\right)}{12V},\tag{2.7}$$

where it was further assumed that V is much greater than the excluded volume overlap between the particles, applicable to most situations where the particles are present at low volume fraction.

We first investigated if the AO model could explain the large depletion attraction exhibited by our polymer-grafted NPs in a *monomeric* matrix. However, a straightforward application was not possible because Eq. (2.6) was derived for hard particles with an excluded volume defined by a sphere of diameter $(D_p + D_m)$, while our NPs have a soft shell of polymer grafts around a hard core. If one considers the average height of the polymer grafts to be h_g and the diameter of the NP core to be D_c, the true excluded volume of the NP can be approximated as a sphere of diameter $(D_c + 2h_g + 1)$, where 1 is the diameter of the depletant (monomeric segments) in reduced units. Thus, the diameter of the depletants D_m in Eq. (2.6) needs to be replaced by an "effective" diameter given by $(2h_g + 1)$. By substituing $h_g \approx 3.0$ computed from simulations, $D_p = D_c = 6$, and $N/V \equiv \rho_p = 0.82$, we obtained $\Delta G_d \approx -340 k_B T$, which is of similar scale as the depletion attraction $W_{m\rightarrow NP}(0)$ computed from simulations. As reference, the AO depletion interactions for bare NPs of the same size in the same medium yielded only $\Delta G_d \approx -4 k_B T$. Thus, the depletion interactions in polymer-grafted NPs can indeed be very large, primarily because they can exhibit an unusually large excluded volume overlap with other NPs due to their soft

polymer grafts.

Next, we applied the model to polymer-grafted NPs in a *polymeric* matrix of length $L_m = 40$, where an entire matrix chain (depletant) was approximated as a hard-sphere of diameter equal to $2R_g$, where R_g is the radius of gyration of the matrix chains; the effective diameter of the depletant now becomes equal to $(2h_g + 2R_g)$ and the depletant density N/V is given by ρ_p/L_m. By computing $R_g \approx 3.0$ from simulations, we obtained a value of $\Delta G \approx -25k_BT$, which is almost two orders of magnitude smaller than the value of $\sim 2500k_BT$ computed from simulations. Thus, the AO model does a poor job of estimating depletion interactions in polymer melts, as it neglects the gain in the internal configurational entropy of the chains, which can be substantial in melts. Nevertheless, to test the reasonableness of this huge depletion attraction observed in our simulations, we simulated the same system *but* containing bare NPs of diameters equal to the effective diameter $(D_c + 2h_g)$ of the polymer-grafted NPs and found that the depletion attraction is indeed comparable to that computed for polymer-grafted NPs (Sup. Fig. 2.18).

It was noted earlier that the strength of the depletion attraction always goes hand-in-hand with that of steric repulsion and that the former is consistently weaker than the latter in all the systems investigated here, including 2-particle configurations (see, for example, Fig. 2.7a). The first observation is easily explained by recognizing that both types of forces increase with the amount of overlap between the grafts, and therefore if the steric repulsion were large due to a large overlap between grafts, the depletion attraction will also be large, and *vice versa*.

To explain the second observation, we consider the simpler case of a 2-particle system comprised of the test and reference NP (Fig. 2.1c). In this system, the depletion force on the test NP arises due to differences in the population of matrix chains interacting with the inside and outside halves of the test NP (facing toward and away from the reference NP); Similarly, most of the steric force ($> 95\%$ in Fig. 2.6) on the test NP arises from its interactions with the grafts of the reference NP, which are clearly more populated on the inside half of the test NP. The observed dominance of steric forces over depletion forces could then be perceived to arise from the mismatch in population of reference NP grafts over the two halves of the test NP being larger

45

than the corresponding mismatch in population of matrix chains [92]. To test this conjecture, we computed the differences $\Delta\rho_g$ and $\Delta\rho_m$ in the average density of polymer segments belonging to reference NP grafts and matrix chains within cylindrical volumes of radius R and thickness d touching the right and left poles of the test NP:

$$\Delta\rho_i = \frac{\int_0^R 2\pi r dr \int_0^d [\rho_i(x,r) - \rho_i(D_c + 2d - x, r)]dx}{\pi R^2 d}, \tag{2.8}$$

where d is the surface-to-surface distance between the reference and test NP whose centers are assumed to be located at positions $x = -D_c/2$ and $x = D_c/2 + d$, and index $i = g, m$ refers to the reference NP grafts or the matrix chains. We obtained $\Delta\rho_g = 0.33$, 0.31, and 0.25 and $\Delta\rho_m = -0.22$, -0.23, and -0.20 for the representative system (system 1, Table 2.1) at increasing separation $d = 2$, 4, and 6; for these calculations we employed $R = 6$, roughly corresponding to the footprint of a polymer-grafted NP (Fig. 2.5). The positive $\Delta\rho_g$ indicates depletion of reference NP grafts on the outside region of the test NP and the negative $\Delta\rho_m$ indicates depletion of matrix chains in the region between the reference and test NP. The decreasing magnitudes of $\Delta\rho_g$ and $\Delta\rho_m$ with increasing d indicates that the matrix and graft segmental densities become more isotropic around the test NP. More importantly, we find that the overall density difference $(\Delta\rho_g + \Delta\rho_m)$ is positive, suggesting a greater imbalance in the segmental density of grafted chains compared to matrix chains, explaining the slightly larger steric forces compared to depletion forces in this system.

2.3.6 Stability of NP Clusters and Phase Diagram

Experiments have shown that polymer-grafted NPs exhibit a rich phase diagram in which they transition from a dispersed morphology at sufficiently high grafting density and graft length to 1D strings to 2D sheets to 3D close-packed structures with decreasing grafting density and graft length. While it is not possible to directly relate the computed 2- and 3-particle PMFs to the stability of several of these higher-order structures due to multi-body effects, such PMFs can

nevertheless provide valuable information on the stabilities of small 2- and 3-particle clusters (dimer and trimer) as a function of parameters like grafting density and graft length; These clusters may be conceived as precursors of the 1D, 2D, and 3D higher-order structures. Note that each of the 3-particle reaction coordinates yields a distinct configuration of the trimer: *linear*, *L-shaped* and *triangular* configuration from $\mathbf{x}_{0°}$, $\mathbf{x}_{90°}$, or $\mathbf{x}'_{90°}$, respectively. The "phase" diagram we seek therefore comprises of five distinct phases: dispersed, dimer, and the three types of trimers.

We constructed such a phase diagram by *first* calculating the free energy change associated with forming a dimer or a trimer from isolated NPs. The free energy $\Delta G_{\text{dim}}(d)$ of forming a dimer with a surface-to-surface separation distance d is simply given by the 2-particle PMF computed earlier that we *now* denote by $W_2(d)$:

$$\Delta G_{\text{dim}}(d) = W_2(d). \tag{2.9}$$

The free energy $\Delta G_{\text{tri}}(d_1, d_2)$ of forming any one of the three trimer configurations can be calculated as the sum of the free energies of first forming a dimer, as a function of distance d_1 between the dimer NPs, and then forming a trimer, as a function of distance d_2 between the third NP attaching onto the dimer:

$$\Delta G_{\text{tri}}(d_1, d_2) = W_2(d_1) + W_3^{2D}(d_2; d_1). \tag{2.10}$$

Here, $W(d_1)$ is the 2-particle PMF computed earlier and $W_3^{2D}(d_2; d_1)$ is a 2D 3-particle PMF that depends on both d_1 and d_2; Note that $W_3^{2D}(d_2; d_1)$ is *different* from the 1D 3-particle PMFs computed thus far, and now denoted by $W_3(d)$, which consider interactions of a third NP with a dimer fixed at the contact distance $d_1 = 0$, that is, $W_3(d) \equiv W_3^{2D}(d; 0)$.

The *next* step involves determining the global minimum in the computed ΔG_{dim} and ΔG_{tri} profiles that provides the relative stability of a structure. If this minimum free energy value is

positive or if the entire profile is always positive, then that structure is deemed unstable. The stability of a dimer can be easily obtained as it involves computation of a 1D free energy profile, but determining the stability of the trimer phase is extremely computationally demanding, as it involves computation of a 2D 3-particle PMF. To this end, we made the following reasonable approximation:

$$\min\{\Delta G_{\text{tri}}(d_1, d_2)\} \approx \min\{W_2(d_1)\} + \min\{W_3^{2D}(d_2; 0)\} \equiv \min\{W_2(d)\} + \min\{W_3(d)\}, \quad (2.11)$$

which allowed us to estimate the stability of the trimer clusters using only the already-computed PMFs. Note that we have assumed here that the minimum free energy of attaching the third NP is minimally affected by the precise configuration of the dimer as long as the dimer NPs are almost at touching distance in their most favorable configuration. This assumption is reasonable considering that (1) the most stable configuration of dimers are indeed ones in which the NPs are separated by small distances ($d_1 \approx 0.024\sigma$; see Fig. 2.3a and earlier discussion), and (2) the PMF computed for system in which the dimer exhibits its most stable configuration ($d_1 \approx 0.024\sigma$) was found to be very similar to the 3-particle PMF computed here with contacting dimer NPs ($d_1 = 0$) (see Sup. Fig. 2.13 and earlier discussion). As explained earlier, the reason that our grafted NPs assemble at such close distances has to do with the short-ranged nature of vdW attraction between NPs as compared to polymer-mediated repulsion (Fig. 2.3a and 2.3b). Therefore, we envision that for systems in which the vdW attraction is longer ranged, for instance when the size of the NPs is much larger and the attraction scales as $\sim 1/d$ or if the systems were so densely grafted that the NPs are unable to displace the grafts to access the strong vdW attraction.

Figure 2.11 compares the formation free energy profiles of the dimer and trimer phases for nine different combinations of graft lengths and grafting densities with the core-core attraction strength fixed at a value of $\varepsilon_c = 1$ roughly corresponding to that of solid silicon. In particular, we compare $\Delta G_{\text{dim}}(d)$ and $\Delta G_{\text{tri}}(d)$, where the latter corresponds to the variation in the free energy of an NP trimer as a function of the distance between a NP and a NP dimer already

assembled and fixed in its most favorable configuration. We observe that the free energy profiles of the dimer and all three trimers are positive at $(L_g, \Gamma_g) = (20, 0.4)$, $(20, 0.2)$, $(10, 0.4)$, and $(5, 0.4)$. This implies that the NPs prefer to remain dispersed for such strongly grafted NPs, where the vdW attraction between the NP cores is too weak to overcome the polymer-mediated repulsion between the NPs. However, as the grafting density and graft length is reduced, the polymer-mediated repulsion becomes weaker, and the dimer and trimer phases begin to exhibit negative free energies of formation. In particular, we find that the linear trimer phase is the most stable phase at $(L_g, \Gamma_g) = (10, 0.2)$ while the triangular trimer phase becomes most stable at $(L_g, \Gamma_g) = (20, 0.1)$, $(10, 0.1)$, $(5, 0.2)$, and $(5, 0.1)$. In general, we find that the stability of the L-shaped trimer is always intermediate to that of the linear and triangular trimers, and hence does not appear as the most stable phase under any grafting condition. We also note the presence of large energy barriers separating the associated and dispersed states. In cases where the bound state is globally stable, the presence of such energy barriers could cause the NPs to get kinetically trapped in the dispersed state, and thermal annealing of the polymer-NP system might be required to help NPs to cross over the barrier and bind to each other.

The above results on cluster stabilities along with those obtained for weaker ($\varepsilon_c = 0.5$) and stronger core/core attraction ($\varepsilon_c = 3$) are summarized in terms of phase diagrams in Fig. 2.12. The general features of these phase diagrams resemble those observed experimentally [72], that is the NPs transition from isotropic structures of high dimensionality (3D aggregates in experiments, triangular trimers here) to anisotropic structures of decreasing dimensionality (2D sheets to 1D strings in experiments, linear trimers to dimers here) with increasing grafting density and graft length, eventually yielding dispersed NPs (both here and in experiments) at sufficiently strong grafting conditions. As expected, a weak core-core attraction strength shifts the boundaries of the phases inwards to small grafting densities and graft lengths, and *vice versa* for strong attraction.

Our phase diagrams also reveal a unique feature that is missing in the experimental phase diagram—the presence of a *globally* stable dimer phase (see Fig. 2.12c). This phase appears within a small window of parameter space—arguably at high grafting densities, long grafts,
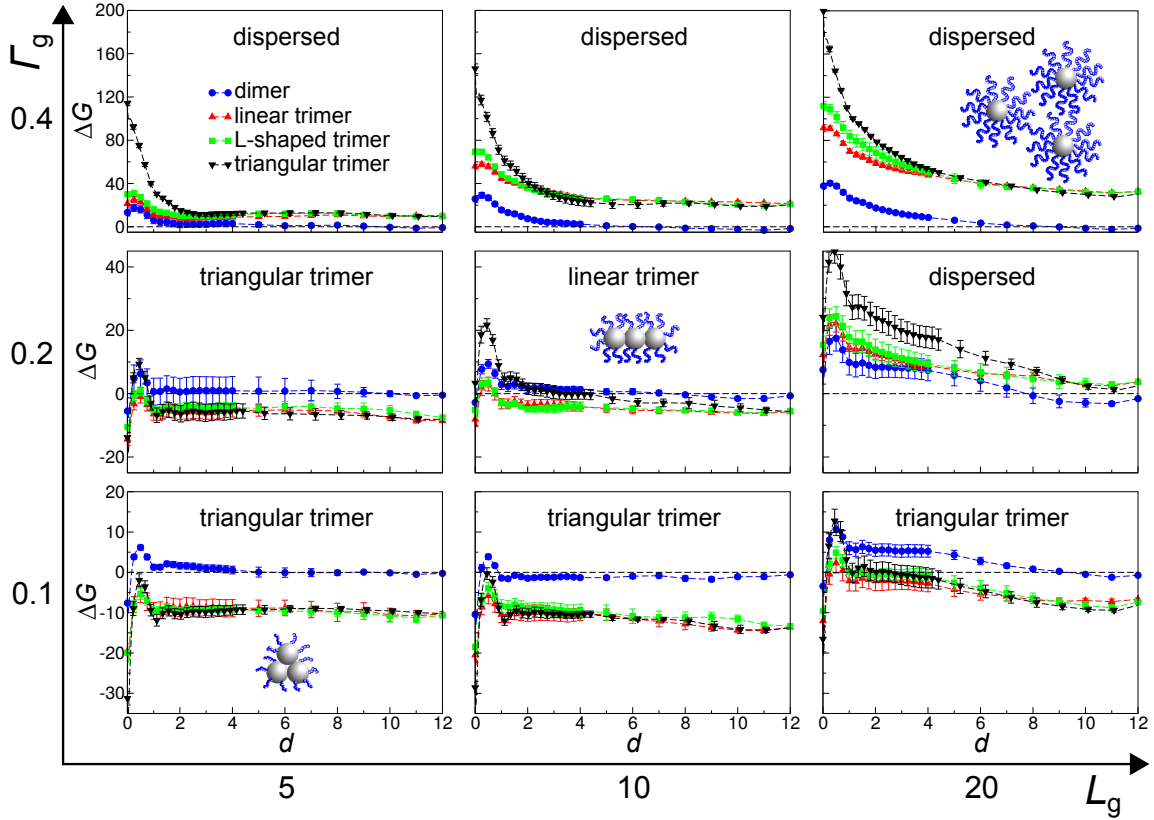
Figure 2.11: Free energies of formation of the NP dimer $[\Delta G_{\text{dim}}(d)]$ and of the three different configurations of NP trimers $[\Delta G_{\text{tri}}(d)]$ for nine different kinds of polymer-grafted NPs in a polymer matrix of chain length $L_m = 40$. The NPs in all systems exhibit the same core-core attraction ($\varepsilon_c = 1$), but differ in terms of their graft length ($L_g = 5, 10, 20$) or grafting density ($\Gamma_g = 0.1, 0.2, 0.4$).

and strong core/core attraction according to our results—where the 2-particle PMF W_2 exhibits an attractive minimum while the 3-particle PMF W_3 is purely repulsive due to the polymer redistribution effect discussed earlier. Within this region of the parameter space, the dimers are stable against dissociation into individual NPs and also stable against growing into trimers.

Since a linear trimer is less stable than the dimer in this region of the phase diagram, then we expect all *n*-particle *linear* structures (1D strings) to be less stable than the dimer, as each *j*-particle PMF W_j ($j > 3$) is at least as repulsive as W_3. Now, it may be argued that the free energies of formation of other more compact higher-dimensional structures (such as tetragonally arranged tetramers, octahedrally-arranged hexamers, etc.) may become lower than the formation
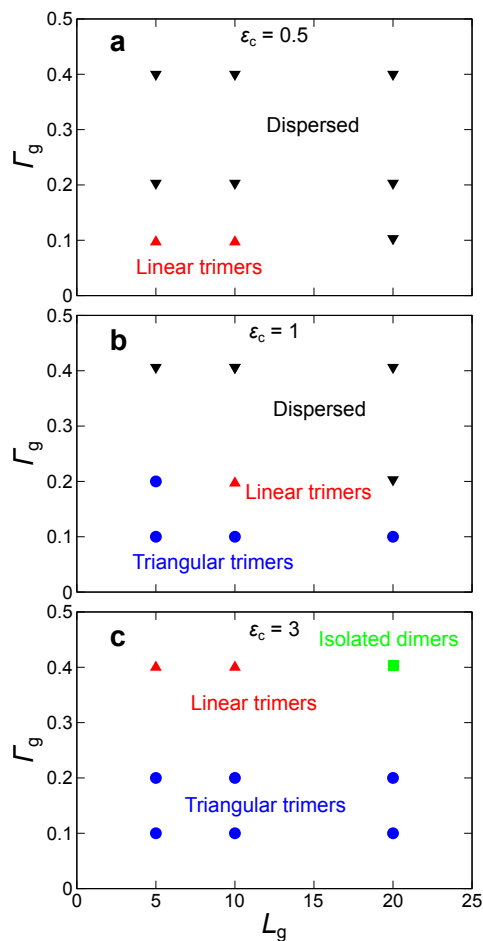
Figure 2.12: Phase diagrams along the graft length–grafting density parameter space depicting the most favorable configuration adopted by three NPs at different fixed values of the core-core attraction strength: (a) $\varepsilon_c = 0.5$, (b) $\varepsilon_c = 1$, and (c) $\varepsilon_c = 3$. The dashed-lines depict qualitatively the boundaries between the different phases.

free energy of the dimer. However, for that to occur, the j-particle PMF associated with the addition of an NP to a $(j-1)$-particle cluster would have to become strongly attractive, e.g., due to sudden jump in the vdW attraction W_c due to increase in the number of NP contacts, and more than counterbalance the strong polymer-mediated repulsion W_p arising from each of these contacting NPs, which is highly unlikely given that W_p increases stronger than linearly with the number of contacts (due to positive many-body contributions). Understandably, such compact higher-order structures appear only under weak grafting conditions (when the graft density/graft length are sufficiently small) in the experimental phase diagram, which is clearly incompatible

with the strong grafting conditions under which the dimer phase is stabilized. Thus, we believe that the dimer phase identified here is also stable against forming higher-order structures. It would be interesting to experimentally test the existence of such a phase and to further investigate and map out its precise location within the grafting parameter space. Such stable NP dimers, as well as other small clusters, could find applications in plasmonics [46, 93].

Note that one cannot make a similar claim about the global stability of any of the trimer configurations observed to be the most stable phase in our phase diagram. The reason is that though this phase has been determined to be averse to dissociating into lower-order structures (individual NPs, or dimer + isolated NP), it remains undetermined whether the phase is also averse to growing into larger structures (e.g., tetramers). In fact, when the trimer phase is determined to be stable, the 3-particle PMF W_3 must be favorable (possess a minimum with negative free energy) according to Eq. (2.11). This would then imply that the 4-particle PMF W_4 associated with attaching a fourth NP to the trimer, would also likely be favorable, especially when the location of attachment is sufficiently far from other non-contacting NPs of the trimer in which case W_4 would be almost as favorable as W_3. The trimer would thus merely represent an intermediate to a more stable tetramer structure, and so forth. Applying such an argument to a linear trimer would suggest that the trimer will continue to grow into a longer linear NP string as each NP addition to the ends of the string serves to further stabilize it. Similarly, the L-shaped and triangular trimer phases may be precursors of the square and hexagonal sheets, though we do not expect each subsequent addition of NP to yield the same free energy change as the 3-particle PMF.

Lastly, we comment that the free energies of formation of clusters calculated from the PMFs ignore the loss in translational entropy and the gain in rotational entropy that NPs undergo upon assembly. The change in entropy associated with the dimerization of two NPs may be

roughly estimated via [94]

$$\Delta S \approx k_\mathrm{B} \left[\ln \left(\rho_N \left(\frac{h^2}{\pi m k_\mathrm{B} T} \right)^{3/2} \right) + \ln \left(\frac{8\pi^2 I k_\mathrm{B} T}{h^2} \right) - \frac{1}{2} \right] \tag{2.12}$$

where ρ_N is the number density of NPs, h is the Planck's constant, m is the mass of each NP, and $I = m D_\mathrm{c}^2/2$ is the moment of inertia of the NP dimer. Using typical sizes (5–100 nm), densities (2–5 g/cm^3), and loadings (2–5 vol%) of NPs, we obtain ΔS in the range -9 to -18 k_B. Thus, the entropy change is small compared to the losses and gains in configurational entropy of the grafts and matrix chains (1000s of k_B according to Figs. 6 and Sup. Fig. 2.14). Hence, we expect the qualitative features of the phase diagram to be largely preserved even in the absence of this free energy component. Moreover, the translational entropy loss is expected to depend on the concentration of NPs. Therefore, the "standard" free energies of formation computed here do not depend on NP concentration, which facilitates easier comparison of the relative free energies of the structures as it does not require any specification of NP concentration.

2.4 Conclusion

We have investigated the role of polymer-mediated interactions between NPs in the formation of anisotropic structures from spherically-symmetric polymer-grafted NPs by computing the overall PMF between a NP-dimer and a test NP along with its 3-body contribution as a function of its orientation relative to the dimer. The rationale is that stable anisotropic phases like 1D strings and 2D sheets must emerge from an anisotropy in the 3-body polymer-mediated component of the PMF because if that is not the case, the NPs would simply assemble into hexagonal close-packed aggregates to maximize the number of attractive contacts between the NPs, or else remain dispersed if the attraction is weak. Our calculations show that the 3-body, polymer-mediated component of the PMF is indeed highly anisotropic, exhibiting the strongest repulsion along the perpendicular axis passing through the center of the dimer and the least

repulsion along its longitudinal axis. Further analysis reveals that this anisotropy, and the even stronger anisotropy observed in the overall PMFs, is directly related to the anisotropic distribution of graft segments near the surface of the dimer. In particular, the polymer grafts in between the dimer NPs get pushed outwards from their contact point causing strong enhancement in the graft segmental density in the contact region in between the two NPs. The enhancement is highest within this region and gradually decreases away from it, reaching its lowest value at the dimer poles, similar to the observed variation in polymer-mediated repulsion. By decomposing the polymer-mediated PMF into steric repulsion arising from the grafted chains and depletion interactions arising from the surrounding matrix, we find that the reduction in the grafted polymer density from dimer contact region to its poles leads to concomitant reduction in steric and depletion interactions along the same direction. However, with the steric repulsion consistently dominating depletion attraction, the net effect is a reduction in polymer-mediated repulsion from the contact region to the poles. This consistent dominance of steric over depletion forces seems to arise from a greater mismatch in the segmental density of grafted chains, as opposed to that of matrix chains, across the inner and outer halves of the interacting NPs. Interestingly, despite the strong variation in the graft segmental density, the overall segmental density remains independent of location around the dimer surface.

Probing further the role of the NP grafts and the surrounding matrix, the anisotropy in both the overall and 3-body contribution of polymer-mediated interactions is found to intensify with increasing graft length and grafting density. This trend arises again due to the simultaneous rise in the steric repulsion and depletion attraction, and the increasing dominance of the former over the latter, with increasing graft length and grafting density. The surrounding matrix has a very different effect, where the anisotropy in the overall PMF is found to diminish with increasing length of matrix chains. In fact, NPs interacting in a monomeric matrix at the same density as the polymer matrix exhibit much higher anisotropy, and those interacting in vacuum exhibit even higher anisotropy. The strength of and anisotropy in the 3-body component, in contrast, are found to increase with increasing matrix chain length. Our analysis shows that

even though both depletion and steric forces decrease rapidly with the monomerization and subsequent removal of matrix chains, the steric forces decrease less rapidly than the depletion forces, leading to increasing anisotropy in polymer-mediated repulsion. Additional analysis reveals that the unusually large depletion forces observed in polymer-grafted NPs arises from the ability of their grafts to overlap when they come into close contact, leading to unusually large changes in the matrix-excluded volume.

Representative overall PMFs, obtained by adding an attractive vdW core/core potential to the polymer-mediated PMF, exhibit more complex behavior. While vdW attraction favors the formation of triangular 3-particle clusters and polymer-mediated repulsion favors (least disfavors) linear clusters, the overall PMF stipulates that all three cluster configurations (triangular, L-shaped, or linear) may be stable depending on the relative strengths of the two PMF components. The overall PMFs also provide some basis for the experimentally observed anisotropic phases given that the triangular, L-shaped, and linear 3-particle clusters may be conceived as precursors of the 2D hexagonal, 2D square, and 1D string phases, and that the three cluster configurations were found to occupy *qualitatively* similar regions of the parameter space as the three higher-order anisotropic phases. Lastly, our cluster phase diagram predicts the possibility of observing a stable NP dimer phase within a narrow window of parameter space where the 2-particle PMF is attractive and all 3-particle PMFs are repulsive. The existence of this novel phase with potential applications in plasmonics remains to be tested.

2.5   Acknowledgments

2.6 Supporting Figures
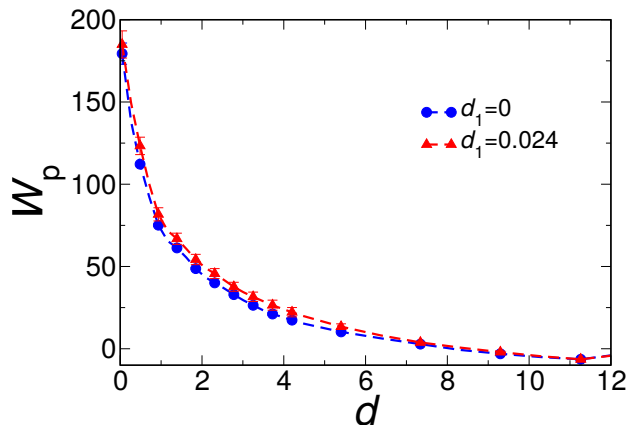
Figure 2.13: Comparison of the polymer-mediated PMF $W_p(d)$ computed with dimer NPs fixed at a separation distance of $d_1 = 0$ apart (as done in all simulations) versus dimers fixed at their most favorable separation distance of $d_1 = 0.024$. The comparison is plotted for the representative NP-polymer system with $L_g = 20$, $\Gamma_g = 0.4$, and $L_m = 40$ along the $\mathbf{x}'_{90°}$.
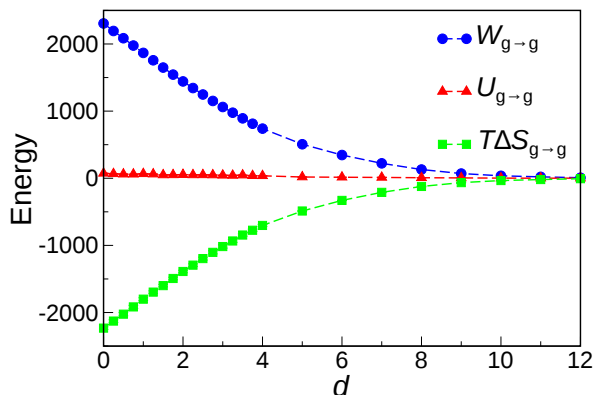
Figure 2.14: Decomposition of graft-graft repulsion $W_{g \to g}$ into its energetic $U_{g \to g}$ and entropic contributions $T\Delta S_{g \to g}$ as a function of separation distance d. The error bars are not shown as they are all smaller than the size of the symbols. $U_{g \to g}$ was calculated as the ensemble average of the potential energy arising graft-graft interactions computed from MD simulations at various fixed distances d while $T\Delta S(d)$ was calculated from the first law of thermodynamics: $T\Delta S(d) = U(d) - W(d)$

.
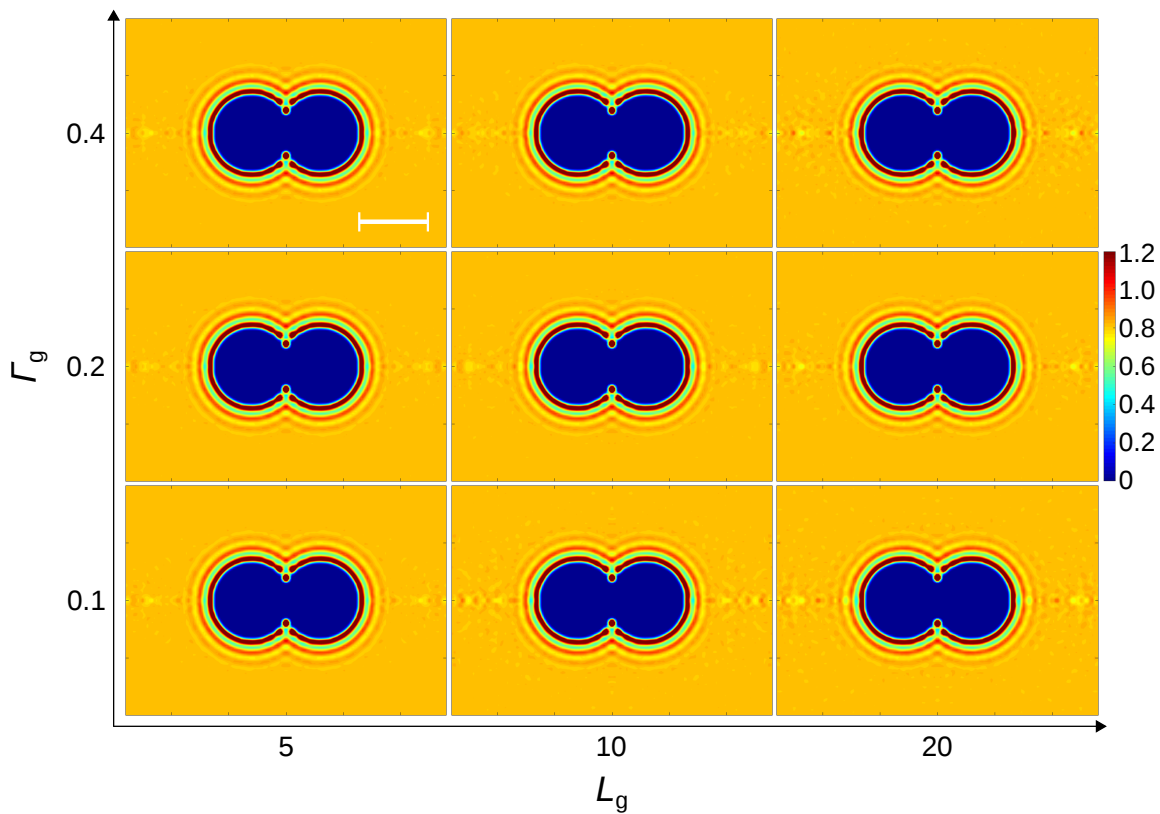
Figure 2.15: 2D contour maps of the overall monomer density $\rho_{g+m}(x, r)$ corresponding to nine distinct NP-polymer systems differing in graft length ($L_g = 5, 10, 20$) or grafting density ($\Gamma_g = 0.1, 0.2, 0.4$). Color bar denotes the magnitude of this density in units of $beads/\sigma^3$. Scale bar denotes the size of the NP core, $D_c = 6$.
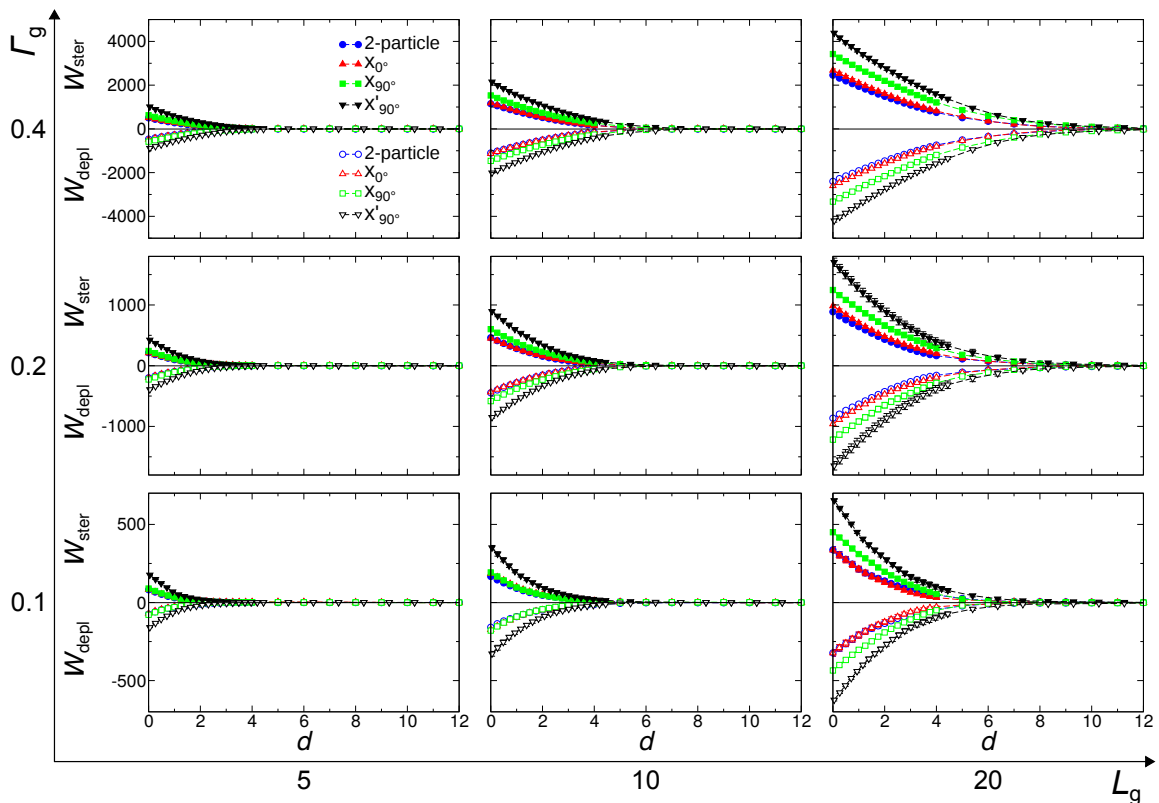
Figure 2.16: Comparison of the steric repulsion and depletion attraction profiles along 2- and 3-particle reaction coordinates for polymer-grafted NPs of size $D_c = 6$ grafted with polymer chains of different lengths ($L_g = 5$, 10, and 20) and at different grafting densities ($\Gamma_g = 0.1$, 0.2, and 0.4) in a polymer matrix of chain length $L_m = 40$.
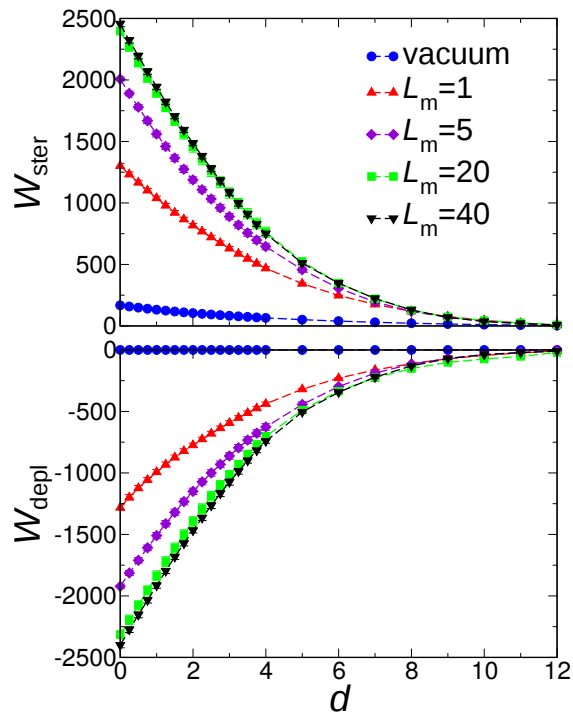
Figure 2.17: Comparison of 2-particle steric repulsion and depletion attraction profiles for NP cores of size $D_c = 6$ grafted with polymer chains of length $L_g = 20$ interacting across vacuum and across polymer matrices of lengths $L_m = 1, 5, 20,$ and 40.
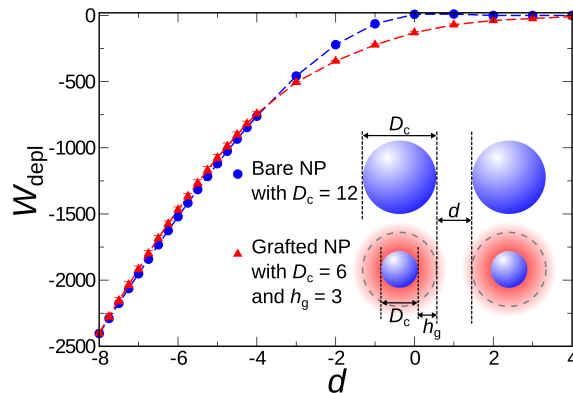
Figure 2.18: Comparison of depletion attraction computed from simulations of grafted NPs in a polymer matrix (system 1 with NP cores of size $D_c = 6$ but effective span of $D_c + 2h_g = 12$, where h_g is the average height of the polymer brush) against that computed from simulations of bare NPs of size $D_c = 12$ in the same polymer matrix.

Chapter 3

Interfacial Assembly of Tunable Anisotropic Nanoparticle Architectures

3.1 Introduction

Polymer-nanoparticle composites have attracted considerable scientific and technological interest in the past few decades. While many traditional applications of such composites require the nanoparticles (NPs) to remain well dispersed within the polymer matrix, some of the newer proposed applications rely on higher-order organization of NPs [59]. For instance, by arranging plasmonic NPs into non-close-packed clusters and periodic arrays, one could take advantage of the unique plasmonic couplings between particles to create optically-active composites [93, 95–98]. In the same vein, the organization of magnetic, semiconducting, or mixtures of semiconducting and plasmonic NPs into specific arrangements results in unique magnetic, exciton, or plasmon-exciton couplings that may be harnessed for novel applications [59, 99–103]. Self-assembly provides a powerful bottom-up approach for organizing NPs in a highly parallelized fashion. However, achieving precise, unique, and complex assemblies of NPs in polymers is challenging. Inorganic NPs are usually polydisperse in size and immiscible in polymers (due to strong interparticle van der Waals interactions, solvophobic surfaces, and

polymer-mediated depletion forces), which cause the particles to kinetically agglomerate into random fractal structures [104–106]. Even if the NPs were homogeneous and their interactions were weakened to access thermodynamically-favored structures, the spherical NPs typically used for assembly would result in close-packed "isotropic" structures that maximize the total number of favorable contacts between the particles.

Several strategies have been proposed to promote NP assembly into "anisotropic" structures that go beyond the isotropic morphologies obtained with spherical NPs. An obvious strategy is to use shaped particles,[46, 60, 107, 108] which can now be routinely synthesized due to advances in inorganic synthesis methods. A related approach is to adsorb or graft functional groups nonuniformly across the surface of the NPs, resulting in "patchy" particles that interact asymmetrically with each other [34, 68, 109]. Though these approaches have yielded encouraging assembly outcomes in aqueous media, achieving similar levels of success in polymeric media has been challenging. A third approach involves grafting polymer chains onto the surface of the NPs [110]. In addition to improving the polymer-miscibility of the NPs, this strategy also introduces anisotropic interactions between NPs due to "polarization" of the distribution of grafted chain segments around NPs when they get close to each other [72, 111]. In this manner, spherical NPs have been assembled into anisotropic structures like sheets and strings by simply varying the grafting density or the length of the grafted chains [72]. Researchers have also used microphase separation of block copolymers to trap small NPs within or at the interface of the formed domains, [31, 112–115] providing an avenue for spatially organizing the NPs. Other approaches involving the use of magnetic and electric fields to align particles also hold promise for directing NP assembly towards anisotropic structures but have so far been applied mostly to micron-sized particles in aqueous systems [39, 40, 116].

Here we propose a new strategy for assembling NPs into unique, anisotropic structures within a polymer matrix, as depicted schematically in Fig. 3.1A. Our approach is motivated by the well-known phenomenon of colloids migrating to gas-liquid or liquid-liquid interfaces to reduce their surface energy [117–120]. We take advantage of this effect to trap NPs at the interface
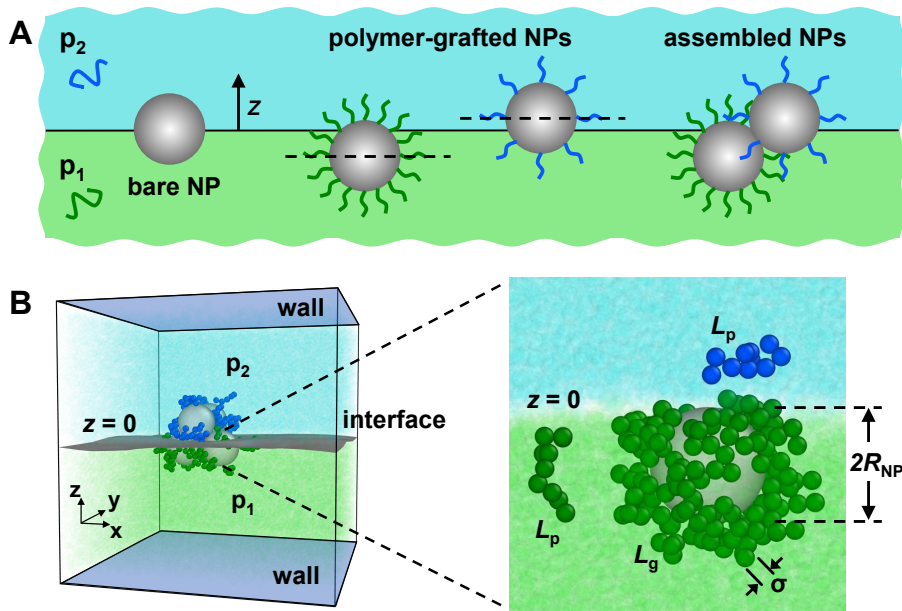
Figure 3.1: Interfacial assembly of NPs into unique clusters and phases. (A) Schematic of the proposed strategy: Bare NPs neutral to both polymer layers p_1 and p_2 of a bilayer get trapped symmetrically at the interfacial plane. Grafting NPs with chains selective to p_1 displaces the NP downwards to a new equilibrium position. Grafts selective to p_2 displace the NPs upwards, but by a smaller distance if the chains are grafted at lower density. Mixtures of such NP species assemble into unique configurations that minimize the overall free energy of the system. A tilted NP dimer assembled in this manner is shown for illustration. (B) Simulation setup and coarse-grained model of the polymer bilayer and polymer-grafted NPs used for demonstrating interface-mediated assembly of NPs. Throughout this study, the top and bottom polymer layers are shown in cyan and fluorescent green, the NP cores are colored grey, and the grafts selective to the two layers are shown in blue and green.

between two mutually immiscible polymers forming a stable bilayer. Thus, NPs that interact similarly with both polymer layers would be expected to localize at the interfacial plane, where they can occlude the largest possible area of the interface and thereby provide the largest free energy benefit. Consider now multiple such NPs that also exhibit strong attractive interactions amongst themselves. While this scenario may facilitate the formation of free-floating planar sheets of NPs, it is not particularly useful for assembling unique structures. To address this shortcoming, we suggest trapping of NPs at *multiple, distinct* planes parallel to the interfacial plane, where the spacing between adjacent planes is small enough to allow the NPs to interact, and potentially assemble, across the planes. For instance, two NPs on opposite sides of the

interfacial plane at normal displacements smaller than the particle radii should still be able to interact with each other to potentially form a tilted NP dimer. To achieve control over the normal positioning of NPs relative to the interfacial plane, we propose grafting the NPs with polymer chains that are preferentially miscible (or immiscible) with one of the two polymer layers. Selective interactions of the grafts should then provide the necessary thermodynamic driving force to displace NPs away from the interfacial plane, and the extent of grafting, a controllable experimental parameter, should be able to provide precise control over the extent of this normal displacement of particles. In the following sections, we demonstrate using computer simulations the ability of the proposed assembly strategy to obtain NP architectures currently not achievable by conventional approaches.

3.2   Results and Discussion

To demonstrate and further investigate the proposed assembly approach, we carried out molecular dynamics (MD) simulations of polymer-grafted NPs in a polymer bilayer formed by two mutually immiscible polymers. Since our primary aim is to elucidate general features of the assembly mechanism and *not* to model any specific system, we used a coarse-grained (CG) model to represent the polymer chains and NPs, which also kept computational costs reasonable (Fig. 3.1B, left). Briefly, the NP grafts and the matrix chains of the bilayer (denoted by "g", and "p_1" and "p_2") were treated as bead-chains [79] in which polymer segments are represented by beads, and the NP cores (denoted by "NP") were treated as rigid spheres. Chains of the same polymer type were considered to be miscible, and hence their segments interacted with each other via a potential that accounts for attractive and excluded-volume interactions. In contrast, the two polymer layers were considered immiscible, and hence their intersegmental interactions were treated using a potential that accounts only for excluded-volume interactions. The grafts were considered to be either partly or fully miscible with one layer and immiscible with the other, and their interactions were again treated using the two kinds of potentials. Attractive and

excluded-volume potentials were also used for modeling interactions between NP cores, and between NP cores and polymer segments. The size σ of polymer beads and the strength ε of attraction between like segments set the length and energy scale of the system. This simple model captures the essential physics of the NP-bilayer system, including the conformational dynamics of the polymer chains, interactions between tethered and free chains, depletion forces exerted by the matrix, and diffusion of grafted particles in polymers [78, 111]. Furthermore, the potentials used for treating miscible and immiscible interactions have been shown to yield stable bilayers that reproduce the density profiles, surface tension, and capillary fluctuations of fluid interfaces [121–123].

The MD simulations were performed in the canonical ensemble at a fixed temperature of $T = \varepsilon/k_B$ and a fixed density of 0.85 beads/σ^3, wherein the system is present in a melt-like state. Periodic boundary conditions were implemented in the x and y directions parallel to the interface and rigid walls were used in the normal direction z (Fig. 3.1B, right). A sufficiently large simulation box was chosen in the normal and lateral directions to prevent artifacts from the confining wall and periodic boundaries, respectively. The chain lengths of both matrix polymers were fixed at $L_p = 10$ beads. The radii of the NP cores were set to $R_{NP} = 3\sigma$, unless otherwise stated, and their surfaces were isotropically grafted with chains; Graft lengths of $L_g = 5$–20 beads and grafting densities of $\Gamma_g = 0$–0.4 chains/σ^2 spanning the mushroom to weak-brush grafting regimes were explored. The strength of attraction ε_g between graft segments and those of the layer miscible to them were varied in the range 0.5–2ε, and an attraction of $\varepsilon_{NP} = 50\varepsilon$ was used for modeling inter-NP interactions. The CG model, choice of parameters, and simulation methods are described in more detail in the **Supporting Information**.

3.2.1 Particle Trapping at Interface

We first examined the behavior of *individual* NPs in polymer bilayers to determine how NP grafting with chains selective to one of the polymer layers affects the interfacial location of the particles. While MD simulations can directly provide the 3D trajectory of a NP as a function of time t from which one could obtain its ensemble-averaged *normal* position $\langle z(t) \rangle$ relative to the interfacial plane (represented by $z = 0$), we used an alternative, more informative route to determining the preferred positions of the NPs. Specifically, we used simulations to compute the free energy (potential of mean force) $\Delta F(z)$ of the NP-polymer system as a function of particle displacement z from the interfacial plane; See **Supporting Information** for specifics on these free-energy calculations. The delta symbol is meant to emphasize that this free energy is obtained *relative* to the free energy of the reference system in which the NP is located far from the interface, in the bulk of the polymer layer miscible with the NP grafts. The location of the global minimum in $\Delta F(z)$, denoted by z_m, should then provide us the most energetically favorable (equilibrium) position of the NP. In addition to equilibrium positions, this free-energy-computation route reveals the energetic basis of particle trapping not possible to obtain from NP trajectories alone and also enables quantitative comparison with the theoretical model of NP trapping developed further below.

To study the effect of grafting, we computed $\Delta F(z)$ for NPs of radii $R_{NP} = 3\sigma$ grafted with chains of length $L_g = 5$ beads that are miscible with one polymer layer (p_1) and immiscible with the other (p_2). For convenience, we chose the grafts to be chemically identical to p_1 chains (i.e., $\varepsilon_g = \varepsilon$). We examined NPs with four different grafting densities Γ_g in the range 0.1 to 0.4 chains/σ^2. For comparison, we also computed $\Delta F(z)$ for a bare NP. **Figure 2A** presents these computed free energy profiles, all of which exhibit a parabolic dependence on z and contain a single minimum. These minima, representing equilibrium positions z_m of particles, shift away from the interfacial plane, and toward the layer compatible with the grafts, with increasing grafting density. Compared to the bare NP that prefers to reside at the interfacial plane
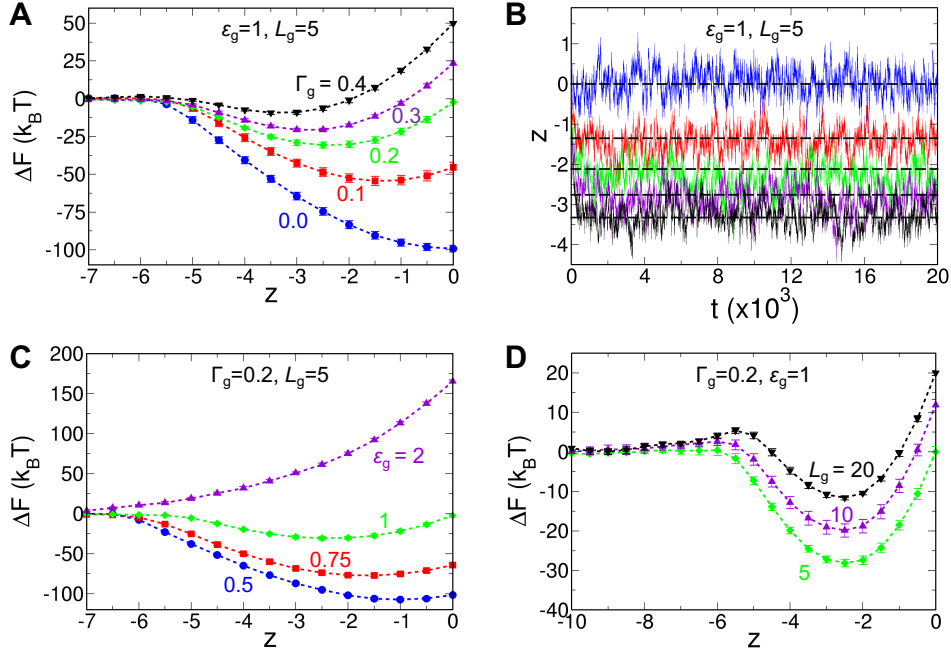
Figure 3.2: Free energy profiles of polymer-grafted NPs as a function of their position from the interfacial plane. (A) $\Delta F(z)$ for NPs with grafting densities $\Gamma_g = 0.1$, 0.2, 0.3, and 0.4 chains/σ^2 compared against that of a bare NP ($\Gamma_g = 0$). (B) Fluctuations in position $z(t)$ of NPs as a function of time t captured from MD simulations of free particles in the bilayer. The five trajectories correspond to the five different NPs examined in (A). Dashed lines correspond to the equilibrium positions z_m obtained from the $\Delta F(z)$ profiles. (C) $\Delta F(z)$ for NPs grafted with chains that are equally incompatible to polymer p_2, but exhibit different compatibility with polymer p_1 ($\varepsilon_g = 0.5$, 0.75, 1, and 2ε). (D) $\Delta F(z)$ for NPs grafted with chains of different lengths $L_g = 5$, 10, and 20 beads.

($z_m = 0$), the NP with the largest grafting density Γ_g considered here gets displaced by a distance ($z_m \approx -3.25\sigma$) almost as large as the NP radius. The equilibrium positions z_m obtained from the free energy profiles agree well with the average positions $\langle z(t) \rangle$ obtained from simulations of freely-mobile NPs (Fig. 3.2B). Note that even though z_m reports the most favorable position while $\langle z(t) \rangle$ reports the ensemble-averaged position, the two quantities are expected to be similar for systems exhibiting a deep and symmetric energy well at the minimum, as observed for our NPs.

The bare NP's preference for the interfacial plane is obviously due to the particle occluding the largest possible area of the interface at this position, which leads to the largest reduction in the interfacial free energy. The free energy gain of $\Delta F(z_m) \sim -100\,k_BT$ indicates very strong

trapping of the NPs; larger particles, in the colloidal range, have been reported to exhibit even stronger trapping [117, 124, 125]. For the grafted NPs, even though their displacement away from the interface reduces the interfacial area occluded by the particle, the resulting increase in the interfacial free energy is more than compensated by favorable interactions between NP grafts and surrounding matrix that are gained as a result of the displacement. This gain arises from both the increase in favorable interactions of the grafts with the polymer layer compatible with them, and the decrease in unfavorable interactions of the grafts with the incompatible layer. The higher the grafting density, the higher the gain in favorable graft-matrix interactions, and the more the particle displaces from the interfacial plane. At sufficiently high grafting density ($\Gamma_g \gtrsim 0.4$), the free energy gain arising from these favorable graft-matrix interactions overwhelms the gain in free energy arising from interface occlusion, causing the NPs to completely detach from the interface and move into the bulk of the polymer layer compatible with the grafts.

We also studied the effects of two additional parameters related to the grafts: the extent of their miscibility with the compatible polymer layer as quantified by the interaction strength ε_g, and their length L_g. Figure 3.2C shows the $\Delta F(z)$ profiles computed for grafted NPs with ε_g in the range 0.5 to 2ε, keeping other grafting parameters fixed ($L_g = 5$ beads and $\Gamma_g = 0.2$ chains/σ^2). The free energy profiles retain the characteristic parabolic shape obtained earlier, and the equilibrium position shifts away from the interface with increasing magnitude of ε_g until the NPs completely detach from the interface and go into the bulk phase at $\varepsilon_g \gtrsim 1.5$. Figure 3.2D shows the free energy profiles obtained for varying graft lengths between $L_g = 5$ and 20 beads with fixed $\Gamma_g = 0.2$ chains/σ^2 and $\varepsilon_g = \varepsilon$. In contrast to the trends obtained with varying Γ_g or ε_g, the equilibrium positions surprisingly show little to no change with increasing magnitude of L_g. A likely source for this insensitivity is the flexibility of the grafts that allows the longer grafts facing the incompatible polymer layer to bend "backwards" to avoid unfavorable interactions with this layer and maximize favorable interactions with the compatible layer (Sup. Fig. 3.8). This effect apparently allows the NPs to maintain the same amount of favorable graft-matrix interactions (interactions with miscible layer minus those with immiscible layer) regardless of

the graft length. Interestingly, NPs with long grafts (especially those with $L_g = 20$ beads) lead to a shallow energy barrier as the particle approaches the interface from the side of the compatible polymer layer ($-6.5\sigma < z < -4.5\sigma$) that also likely arises from this backward bending of grafts, which leads to some loss of their conformational entropy.

The above results demonstrate that NPs grafted with chains selective to one of the layers of a polymer bilayer provides a viable approach for trapping NPs at normal positions located roughly within a radius of the particle on either side of the interface ($|z_m| \lesssim R_{NP}$). We also illustrated that the equilibrium displacement z_m of the NPs from the interface can be effectively tuned by modulating the surface density of the grafts or the difference in their compatibility with the two polymer layers, though the former perhaps offers the best control and range from an experimental standpoint. Hence, in the remainder of this work, we use the grafting density as our "knob" (keeping the length and misciblity of the grafts fixed at $L_g = 5$ and $\varepsilon_g = \varepsilon$) to tune the positions, and thereby the interactions between polymer-grafted NPs at polymer/polymer interfaces.

3.2.2   Theoretical Model of Trapping

The free energy profiles and equilibrium positions computed from simulations can be described by a simple model, enabling quantitative prediction and explanation of the observed effects of NP grafting. To obtain this model, we considered the migration of a NP from the bulk region of the polymer layer compatible with its grafts (say p_1) to a distance z from the interfacial plane where the NP intersects it (Fig. 3.1A). The free energy change associated with this migration is made up of two contributions: $\Delta F(z) = \Delta F_{int}(z) + \Delta F_{graft}(z)$. The first term $\Delta F_{int} \equiv -\gamma_{p_1-p_2} A_{p_1-p_2}(z) < 0$ represents the gain in free energy due to the NP occluding part of the interface, where $\gamma_{p_1-p_2}$ is its surface tension and $A_{p_1-p_2}$ is its circular area occluded by the NP. The second term $\Delta F_{graft} \equiv \Delta\gamma'_{g-p} A_{g-p_2}(z) > 0$ represents the loss in free energy caused by the replacement of part of the favorable interactions of the grafts with the compatible chains of

layer p_1 for unfavorable interactions with incompatible chains of layer p_2 across the interface, where $\Delta\gamma'_{\text{g-p}}$ is the difference in the surface energies of the grafts interacting with the two layers and $A_{\text{g-p}_2}$ is the area of the spherical cap of grafts in contact with layer p_2; The prime symbol is used for differentiating such energies from the surface tension traditionally applied to interfaces formed between free polymer chains. By writing down the two area terms in terms of effective radii $R' > R_{\text{NP}}$ of NPs that includes the graft contribution, we arrive at the following expression for the free energy change we seek (see Supporting Information and the associated Sup. Figs. 3.9 and 3.10 for complete derivation):

$$\Delta F(z) = \begin{cases} 0 & z \leqslant -R' \\ -\pi\left(R'^2 - z^2\right)\gamma_{\text{p}_1\text{-p}_2} + 2\pi R'(R' + z)\Delta\gamma'_{\text{g-p}} & |z| < R' \\ 4\pi R'^2 \Delta\gamma'_{\text{g-p}} & z \geqslant R' \end{cases}, \qquad (3.1)$$

The above expression yields a quadratic dependence of ΔF in position z, explaining the parabolic shapes of the computed free energy profiles in Fig. 3.2A. The equilibrium position of the NPs may be obtained via $\partial\Delta F/\partial z|_{z_{\text{m}}} = 0$, yielding $z_{\text{m}} = -(\Delta\gamma'_{\text{g-p}}/\gamma_{\text{p}_1\text{-p}_2})R'$. This result suggests that the NPs prefer to stay at the interfacial plane when they are equally selective to both polymer layers ($\Delta\gamma'_{\text{g-p}} = 0$), and get increasingly displaced from this position with increasing difference in the compatibility of the NP with the two layers (increasing $\Delta\gamma'_{\text{g-p}}$), predictions consistent with our simulations. The model also predicts that no minimum exists for $\Delta\gamma'_{\text{g-p}} > \gamma_{\text{p}_1\text{-p}_2}$ when the NPs become too selective for one of the layers and prefer to remain fully immersed in it. The relative stability of the NP to reside at locations intersecting the interfacial plane, as compared to the bulk within their favored layer, is given by $\Delta F(z_{\text{m}}) = -\pi R'^2(\gamma_{\text{p}_1\text{-p}_2} - \Delta\gamma'_{\text{g-p}})^2/\gamma_{\text{p}_1\text{-p}_2}$. Thus, the NPs that exhibit the highest interfacial stability are those that are neutral to both polymer layers $\Delta\gamma'_{\text{g-p}} = 0$, and thereby position themselves at the interfacial plane to occlude the largest possible area of the interface without sacrificing any favorable graft-matrix interactions. The stability decreases as the NP-matrix interactions become more asymmetric ($\Delta\gamma'_{\text{g-p}} \neq 0$), and
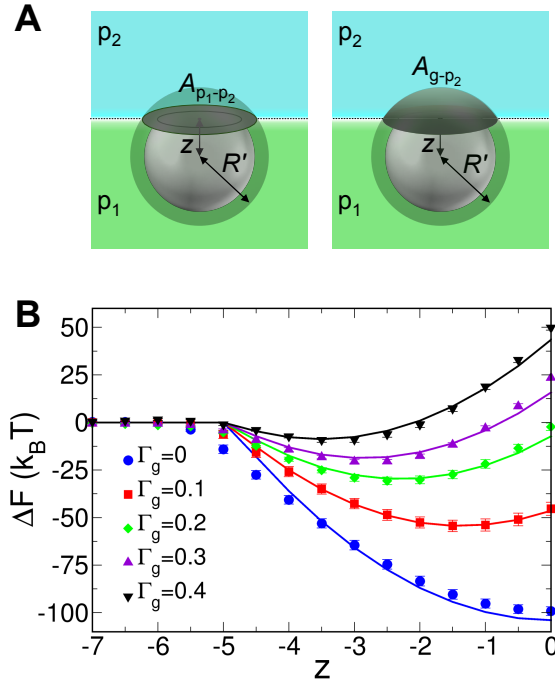
Figure 3.3: Free energy model for NP trapping at interfaces. (A) Schematic showing the two main contributions to the free energy in this model: loss in interfacial surface energy proportional to the circular cross-sectional area $A_{p_1-p_2}$ occluded by the polymer-grafted NP, and gain in the surface energy of the grafts with the surrounding polymer matrix proportional to the area A_{g-p_2} of the spherical cap contacting the incompatible polymer p_2. (B) Model fits (solid lines) to the free energy profiles computed from simulations (symbols) for bare NPs and NPs grafted with chains at the four grafting densities shown in Fig. 3.2A.

the NPs get increasingly displaced away from the interfacial plane. Another consequence of the quadratic nature of this model is its curvature $\kappa \equiv \partial^2 \Delta F / \partial z^2 = 2\pi\gamma_{p_1-p_2}$ that, interestingly, depends *only* on properties of the bilayer (its interfacial tension) and *not* of the grafted NPs (e.g., their size or interactions). This result also implies that the NPs trapped at the interface should exhibit similar fluctuations δz in their normal position irrespective of NP size or interactions, given that $\delta z \sim \sqrt{k_B T / \kappa}$. Indeed, the computed free-energy profiles for the various NPs explored here appear to display similar curvatures (Fig. 3.2A,C,D), and the trapped NPs appear to exhibit similar extents of fluctuations irrespective of their grafting density (Fig. 3.2B). Our model is thus able to *qualitatively* explain all observed trends in the computed free energy profiles.

We also investigated the ability of our model to *quantitatively* fit the free energy profiles

computed from simulations by setting $R' = 4.95\sigma$ and using the unknown $\gamma_{p_1\text{-}p_2}$ and $\Delta\gamma'_{g\text{-}p}$ as adjustable parameters. Since the bilayer was kept the same across all systems, $\gamma_{p_1\text{-}p_2}$ in the model was kept unchanged across all profiles during the fitting procedure. However, $\Delta\gamma'_{g\text{-}p}$, which is expected to vary with the grafting density, was adjusted independently for each profile. Figure 3.2B shows model fits obtained for the bare NP and the grafted NPs at the four grafting densities simulated here. We find that the model does an excellent job in fitting all profiles. There are slight discrepancies at $z < -R'$ where our model enforces ΔF to instantly flatten out as the NPs no longer contact the interface, whereas the computed profiles indicate a more longer-ranged effect of the interface, albeit weak, that extends to distances as large as ~6σ. This effect could arise from multiple factors not accounted in this model, including capillary fluctuations of the interface and stretching of NP grafts or the deformation of the interface to remain in mutual contact, as depicted in Sup. Fig. 3.11. The model does an excellent job in predicting the equilibrium positions of the NPs for both the bare and grafted NPs (Sup. Fig. 3.8a). In addition, the fitted value of $\gamma_{p_1\text{-}p_2}$ compares favorably to surface tensions estimated from theory and those measured experimentally, and the fitted values of $\Delta\gamma'_{g\text{-}p}$ also seem physically reasonable (see Supporting Information and Sup. Fig. 3.12b).

3.2.3   Assembly of Interfacial Clusters

Having demonstrated how a polymer bilayer could be used to trap polymer-grafted NPs in 2D planes parallel to the interface and how the NP grafting density could be used to control the position of these NP traps, we next investigated how the interactions between *multiple* such NPs trapped within different planes could be harnessed to assemble NPs into unique configurations. We began by probing the assembly of *two* "anti-symmetric" polymer-grafted NPs identical in all aspects *except* that they are grafted with chains compatible with opposite layers of the bilayer. Based on our earlier results, we anticipated that the two NPs would partition into opposite sides of the interfacial plane while still intersecting partly with it, thereby allowing for interactions
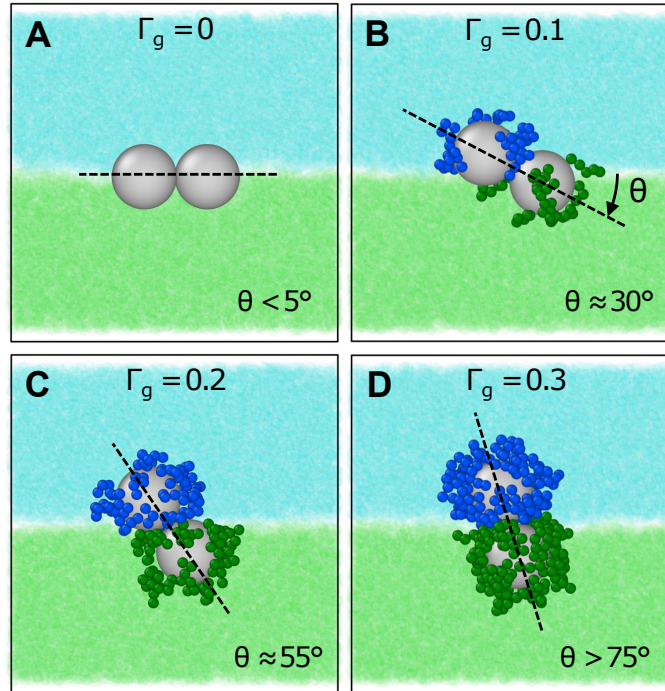
Figure 3.4: NP dimers with a tunable tilt relative to the interface assembled from anti-symmetric polymer-grafted NPs. Representative configurations taken from simulations illustrate how dimers become increasingly tilted with increasing grafting density, exhibiting average tilt angles of (A) $\theta \approx 0°$ for bare NPs, (B) $\theta \approx 30°$ for $\Gamma_g = 0.1$ chains/σ^2, (C) $\theta \approx 55°$ for $\Gamma_g = 0.2$ chains/σ^2, and (D) $\theta > 75°$ for $\Gamma_g = 0.3$ chains/σ^2. Dimer axes are shown as dashed lines.

between the NPs across the interface. To examine how these interactions manifest into assembly, we simulated the dynamics of two such NPs within a bilayer, starting from a well separated configuration of NPs, where they were present in their respective layers at distances $z = \pm R_{NP}$ sufficiently far from the interface but well within the influence of the interfacial trap. As earlier, we studied NPs of size $R_{NP} = 3\sigma$ grafted with chains of length $L_g = 5$ beads at four different grafting densities in the range $\Gamma_g = 0.1$ to 0.4 chains/σ^2 with bare NPs as control. In each simulation, one NP had grafts chemically identical to the chains of layer p_1 with attraction strength $\varepsilon_g = \varepsilon$, and the other to p_2, also with $\varepsilon_g = \varepsilon$.

Our simulations show that the *bare* NPs assembled into a stable dimer whose axis is oriented horizontally, parallel to the interface (3.4A). The assembly was found to occur via

two pathways: the two NPs diffused and migrated to their preferred location, the interfacial plane, before colliding with each other to form a horizonally-aligned dimer; or the NPs collided and stuck to each other before reaching the interface to yield a tilted dimer, which eventually rotated into the preferred horizontal orientation. The *grafted* NPs of low to medium grafting densities ($\Gamma_g = 0.1$–0.3 chains/σ^2) also exhibited similar assembly dynamics, *except* that they partitioned to their off-centered locations above and below the interface, and yielded stable NP dimers whose center of masses remain at interfacial plane ($z_{com} \approx 0$) but whose axes display a visible tilt relative to the interface (Fig. 3.4B–D). Interestingly, the tilt angle increases with increasing grafting density. This effect results from the NP cores attempting to maintain contact with each other (as a result of strong but short-range attraction between them) without sacrificing the free energy gained from the interface. Due to this geometric constraint, the tilt angle θ can be easily predicted as $\theta = \sin^{-1}(|z_m|/R_{NP})$, where $|z_m|$ is the equilibrium distance of either NP from the interfacial plane in isolation. Comparison of the predicted tilt angles with those measured directly from simulations reveals good agreement between the two sets of angles (Sup. Fig. 3.13), confirming that NPs indeed prefer to stay within their interfacial traps z_m, largely unhindered by the presence of the other particle. At sufficiently high grafting densities ($\Gamma_g = 0.4$ chains/σ^2), the NPs stay relatively far from the interface and even when the two NPs collide with each other, they are unable to form a stable dimer, arguably due to strong steric repulsion between their grafts. Thus, interfacial trapping of NPs could indeed be used to assemble *anti-symmetric* dimers of NPs, and moreover tune their orientation with respect to the interface. It should be straightforward to extend these results to *asymmetric* dimers, where the two NPs have different sizes or grafting densities. In both cases, the particles will prefer to reside at different absolute distances $|z_{m,1}| \neq |z_{m,2}|$ from the interface, resulting in dimers that are overall shifted from the interfacial plane ($z_{com} \neq 0$), and exhibit a tilt angle $\theta = \sin^{-1}[(|z_{m,1}| + |z_{m,2}|)/(R_{NP,1} + R_{NP,2})]$, where $R_{NP,1}$ and $R_{NP,2}$ are the core radii of the two NPs.

The NP-trapping approach could also be used to assemble *larger* anisotropic clusters encompassing more than two species of NPs. As demonstration, we attempted to assemble *open*
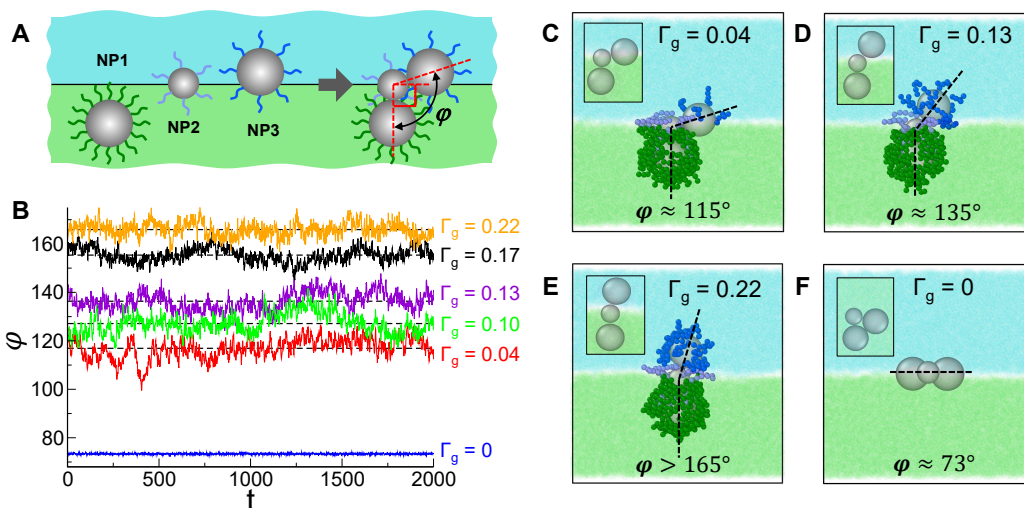
Figure 3.5: NP trimers with open and tunable bending angle assembled at the polymer interface. (A) Schematic of the strategy for assembling such trimers involving three NPs (NP1, NP2, and NP3) grafted with different kinds of chain (see text for more details). (B) Bending angles $\varphi(t)$ obtained as a function of time t from simulations of trimer systems differing in the grafting density on NP3 (as specified), but fixed grafting densities on NP1 and NP2, respectively. (C-E) Representative configurations of these trimers captured from simulations with $\varphi \approx 115°$ (C), $\varphi \approx 135°$ (D), and $\varphi > 165°$ (E) obtained using grafting densities of 0.04, 0.13, and 0.22 chains/σ^2 on NP3 (insets show NP configurations more clearly without their grafts). (F) Representative configuration of a closed trimer with $\varphi \approx 73°$ obtained from bare NPs (inset shows top view for better visualization).

NP trimers with a tunable "bending" angle, defined as the angle φ subtended by the two terminal NPs about the middle NP. Clearly, such configurations cannot be achieved using bare NPs, which would simply assemble into *closed* triangles, both in the bulk phase and at an interface. To this end, we proposed grafting the three NPs with distinct types and/or numbers of chains to trap them at different distances from the interfacial plane in such a way that the two terminal NPs cannot contact and stick to each other (Fig. 3.5A). Specifically, we proposed trapping the middle NP (labeled "NP2" in the figure) at the interface by leaving the particle bare or grafting it with chains neutral to both polymer layers. The other two NPs (labeled "NP1" and "NP3") could be trapped on either sides of the interface by grafting them with chains selective to opposite polymer layers. To achieve the widest possible range of φ, one of these terminal NPs (NP1, say) was densely grafted to push it as far as possible into the bulk polymer phase without completely

detaching from the interface, and the middle NP was kept sufficiently small so that it contacted NP1 in a perpendicular orientation. The other terminal NP (NP3) whose relative orientation with respect to NP2 could be modulated via its grafting density should then provide us a "knob" for tuning φ.

To test this strategy, we performed simulations of appropriately chosen polymer-grafted NPs in the bilayer. We used $R_{NP} = 3\sigma$ particles for the terminal NPs and graft lengths of $L_g = 5$ beads on all three NPs, as in the dimer simulations. As proposed, NP1 was densely grafted with chains miscible to p_1; We found that $\Gamma_g = 0.52$ chains$/\sigma^2$ pushed NP1 to $z \simeq 5\sigma$, a position where its grafts barely touch the interface. NP2 was chosen to have a smaller size of $R_{NP} = 2$ so that it could bind to NP1 in a vertical orientation without sacrificing its equilibrium position ($z_m \approx 0$). While a bare particle could also yield this desired position and contact orientation, we chose to graft NP2 with neutral chains at a moderate grafting density of 0.32 chains$/\sigma^2$ given that grafting offers the additional benefit of stability against potential aggregation of NPs. While this is not an issue when studying isolated clusters, nonspecific aggregation of NPs could become problematic when examining the assembly of larger numbers of clusters at high concentrations. Lastly, NP3 was grafted with chains miscible to p_2, and its grafting density was varied between 0.04 and 0.3 chains$/\sigma^2$ to modulate the trapped position of NP3, and thereby modulate φ. As before, we used $\varepsilon_g = \varepsilon$ to treat all miscible interactions of NP1 grafts with p_1, NP2 grafts with p_1 and p_2, and NP3 grafts with p_2. All simulations were initiated from a dispersed configuration of NPs.

Figure 3.5B shows the results of these simulations in terms of the bending angle $\varphi(t)$ measured as a function of simulation time t for each successfully-formed trimer *post* assembly. Representative snapshots of several of these trimer configurations as captured from the simulations are provided in Fig. 3.5C-E. Our results confirm the assembly of open trimers with the "bond" between NP1 and NP2 oriented vertically with respect to the interface, consistent with our design strategy. Equally importantly, the results confirm that the grafting density on NP3 could indeed be used to modulate the bending angle of the trimers. In particular, the lowest

grafting density examined here yielded bending angles close to $115°$, and increasing the grafting density gradually pushed NP3 away from the interface, yielding larger trimer angles. In this manner, we were able to achieve trimer bending angles between $115°$ to $180°$. Also evident from Fig. 3.5B is the absence of bending angle data for systems in which NP3 was grafted with $\Gamma_g > 0.22$ chains/σ^2. Though these systems were able to yield stable dimers of NP1 and NP2, the densely-grafted NP3 was unable to bind sufficiently strongly to NP2 due to the combined effect of NP3 residing too far from the interface as a result of the strong grafting and NP2 being pulled away from the interface due to NP1. Finally, to confirm that bare NPs, even at interfaces, are unable to yield such open trimer configurations, we simulated the above NPs without any grafts. As anticipated, the three bare NPs migrated to the interface and assembled into a horizontally-aligned trimer with a closed angle of approximately $73°$ (Fig. 3.5F); Note that the smaller size of the middle NP compared to the end NPs makes $\varphi > 60°$.

3.2.4   Assembly of Interfacial Phases

Consider the small clusters of interfacial NPs assembled above. While clusters of densely-grafted NPs are likely stable against further association with other NPs and clusters due to steric repulsion from their grafts, clusters of weakly-grafted or bare NPs might continue to assemble if additional NPs were available. We sought to investigate the kind of macroscopic structures (phases) such NPs formed. A *single* species of NPs would be expected to assemble into a hexagonally-packed monolayer (assuming sufficiently high surface tension, and negligible or weak multibody interactions between bare or weakly-grafted NPs [72, 111]), and depending on the preferred positions z_m of its NPs, the monolayer will form at the interface plane or offset from it. However, the assembly outcome is less straightforward for *multiple* NP species, where the different NP species prefer to reside in distinct planes parallel to the interfacial plane. Here, the NPs would be expected to compete for their favorite locations at or displaced from the interfacial

plane while the system as a whole attempts to also maximize the net number of favorable contacts between the NPs.

To illustrate how this interplay between interfacial and interparticle forces leads to novel assembly structures, we considered a binary system composed of equal numbers of the two anti-symmetric NP species studied earlier in the context of tilted dimers. The two NP types prefer to occupy positions within 2D planes on opposites sides of the interface with an interplanar distance $\Delta d = 2|z_\mathrm{m}|$ that can be tuned via the grafting density from a value of 0 to a value as large as $2R'$, the effective diameter of the NPs. The two layers of NPs are therefore expected to interact with each other, especially for weakly-grafted NPs where Δd is small, raising the possibility of forming interdigitated bi-layered structures. In this work, we simulated the assembly behavior of $N = 12$ such NPs (6 particles of each species) with Γ_g in the range 0.05 to 0.3 chains/σ^2. The grafting densities were kept small enough to promote interactions between NPs across the interface and to also allow NPs to stick to each other, and the particle numbers were kept large enough to enable extrapolation of the resulting finite-sized structures to macroscopic phases. For comparison, we also simulated the assembly of 12 bare NPs in a bulk polymer and in a polymer bilayer.

Simulations of bare NPs showed that in the bulk they assembled into the expected close-packed structure resembling a truncated triangular dipyramid [126, 127] (Fig. 3.6A), while in the bilayer the NPs formed the expected interface-trapped hexagonally-arranged monolayer [128] (Fig. 3.6B). In the $N \to \infty$ limit, the bulk structure should morph into a hexagonal- or cubic-close-packed lattice, and the interfacial structure should continue growing into an infinite planar sheet with hexagonally-arranged particles. In both these structures, as well as all ensuing structures, the interparticle spacings are consistent with the minimum of the NP-NP interaction potential given by $2R_\mathrm{NP} + (2^{1/6} - 1)\sigma \approx 6.12\sigma$, which we denote by R^*.

Compared to these known structures, the symmetric grafted NPs assembled into unconventional structures in the bilayer. The NPs with the smallest grafting density of 0.05 chains/σ^2 assembled into a hexagonally-arranged ridged monolayer comprised of alternating lines of NPs
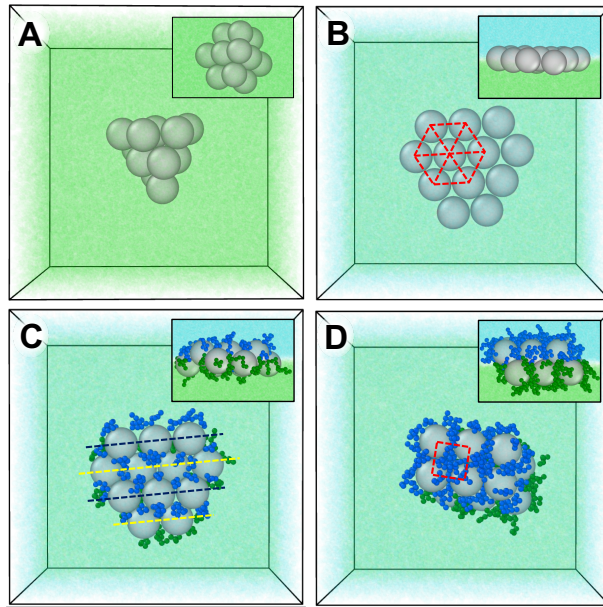
Figure 3.6: Higher-order structures of polymer-grafted NPs assembled at the interface of a polymer bilayer compared against those assembled using bare NPs. (A) Truncated triangular dipyramid obtained from bare NPs in a bulk polymer. (B) Hexagonal monolayer obtained from bare NPs in a bilayer interface. Red dashed lines show the underlying hexagonal packing. (C) Hexagonally-ordered ridged monolayer obtained from grafted NPs ($\Gamma_g = 0.05$ chains/σ^2) in a bilayer. Black and yellow dashed lines indicate NPs located above and below the interface. (D) Cubic-ordered bilayer obtained with grafted NPs ($\Gamma_g = 0.1$ chains/σ^2) in a bilayer. Red dashed lines emphasize square packing. Insets show structures from a view parallel to the interface.

positioned $\approx 1.2\sigma$ above and below the interface (Fig. 3.6C). These undulations obviously arise from the two species of NPs attempting to retain their preferred positions of $z_m \approx \pm 0.9\sigma$ on either side of the interfacial plane, as predicted for isolated NPs from Eqs. 2 and 6. As these NPs prefer to remain close to the interface, the NPs would have to sacrifice a larger amount of interfacial free energy to stretch apart to form a bilayer than the energy they would gain from the additional NP contacts provided by such a bilayer. Consequently, the NPs prefer to form a monolayer, albeit an undulating one, that exhibits a smaller number of favorable contacts, but occludes a large area of the unfavorable interface.

The NPs with slightly denser grafts ($\Gamma_g = 0.1$ chains/σ^2) form an interdigitated bilayer displaying an unusual square arrangement of NPs in each layer (Fig. 3.6D). Due to their stronger grafting, these NPs would individually prefer to reside farther from the interfacial plane ($z_m \approx$

$\pm 1.4\sigma$ from Eqs. 2 and 6). In the bilayer, these NPs are located roughly $\pm 2.16\sigma$ from the interfacial plane, indicating that the NPs get displaced by a small distance ($2.16\sigma - 1.4\sigma = 0.76\sigma$) from their preferred positions. Hence, the formation of a bilayer from such NPs leads to only a small sacrifice in the interfacial free energy, which is easily compensated by the interparticle interaction energy gained by the formation of the bilayer (8 contacts per NP in the bilayer *versus* 6 in the monolayer). A similar reasoning can be used to explain why the NPs prefer to form a square bilayer as opposed to a hexagonal bilayer that one might naively expect. Based on geometrical arguments (see Sup. Fig. 3.14), the two NP layers of a close-packed hexagonal bilayer would be located at a distance $\pm R^*/\sqrt{6} \approx \pm 2.5\sigma$ from the interface and each NP would exhibit 9 contacts (6 within the layer and 3 in the other layer). Thus, the formation of a hexagonal bilayer as opposed to a square one, would require larger displacements ($2.5\sigma - 1.4\sigma = 1.1\sigma$ *vs.* 0.76σ) of the NPs from their preferred positions, while gaining only a single additional contact (9 *vs.* 8 contacts). To rule out the distinct possibility that the square arrangement arose from any intrinsic tendency of NPs in each layer to form a square pattern (e.g., due to multibody effects arising from the grafts), we performed simulations of the same system, but containing only one of the NP species. Our results show that each NP species, *on its own*, prefers to form a hexagonal monolayer (Sup. Fig. 3.15), confirming that it is indeed interlayer interactions that are responsible for the formation of the square bilayer, which sacrifices much less interfacial free energy than a bilayer that had retained the hexagonal arrangement of the monolayers. Interestingly, simulations of systems with fewer NPs of one of the two species also reveal partial to perfect square arrangement of the NPs of the other species (Sup. Fig. 3.16).

Higher grafting densities of 0.15 and 0.2 chains/σ^2 allowed the top and bottom layers of NPs to retain hexagonal order, but interestingly did *not* lead to the close-packed, hexagonal bilayer configuration depicted in Sup. Fig. 3.14 that maximizes the number of NP-NP contacts across the interface. Instead, the two NP layers stretched apart, shifted, and rotated relative to each other (Sup. Fig. 3.17a,b), while remaining stably bound to one another. These deviations, which increase in going from $\Gamma_g = 0.15$ to 0.2 chains/σ^2, obviously arise from the stronger

steric repulsion that the two NP layers experience due to the NP grafts, which are now present at a higher density. The separation, shift, and rotation of the NP layers helps alleviate some of this repulsion by creating larger voids for the grafts in between the two layers, and also freeing up grafts on some of the exposed NPs at the monolayer corners. Whether the two layers remain bound for $N \rightarrow \infty$ and retain the same orientation obtained here, and whether fine tuning of the grafting density within the 0.1 to 0.15 chains/σ^2 range not considered here yields the ideal close-packed hexagonal bilayer remain open questions. Lastly, at even higher grafting densities of 0.3 chains/σ^2, the steric repulsion between the NPs becomes so large that they are unable to even form ordered monolayers, resulting in significantly open and irregular structures (Sup. Fig. 3.17c).

Lastly, we explored the potential of our approach to also assemble quasi-1D structures, in addition to the small clusters and quasi-2D phases demonstrated above. One strategy for promoting the formation of linear structures is through the use of NPs grafted with chains at intermediate densities, where the steric repulsion between the grafts is small enough to allow assembly along one lateral direction, but large enough to prevent assembly along both lateral directions. Specifically, the expulsion of grafts from in between two bound NPs leads to an anisotropic distribution of graft segments around the dimer, causing a third approaching NP to feel stronger steric repulsion at the contact region of the dimer as opposed to its poles. Thus, the dimer becomes more susceptible to further assembly through its poles (longitudinal axis) rather than near the contact region (perpendicular directions) [72, 111]. Such "multibody interactions" have indeed been proposed to lead to string-like NP aggregates in bulk polymers, and has the potential to lead to interesting structures at interfaces.

Figure 3.7 provides two examples of such NP structures created via this strategy. The first structure, exhibiting a "serpentine" morphology (Fig. 3.7A), was obtained from further assembly of the four tilted NP dimers with $\Gamma_g = 0.3$ chains/σ^2 reported in Fig. 3.4D, but in a bilayer of shorter matrix chains ($L_m = 5$ beads) to promote stronger multibody effects [111]. While the mechanism for the formation of the serpentine morphology is not fully known, it likely arises
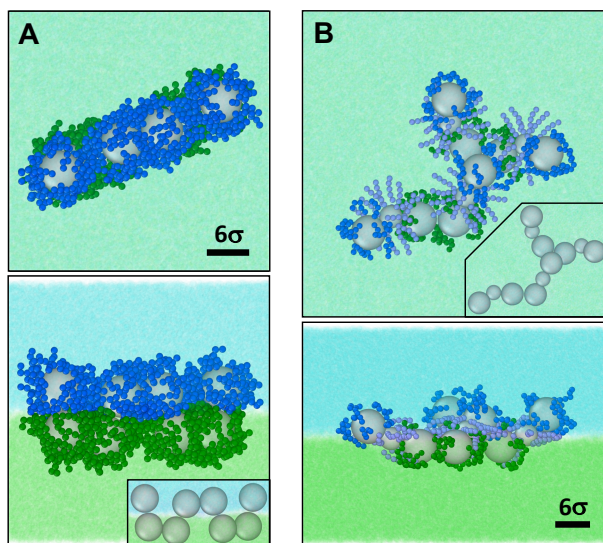
Figure 3.7: Quasi-linear structures of polymer-grafted NPs assembled at the interface of a bilayer: (A) Serpentine structure obtained from two anti-symmetric species of NPs grafted at $\Gamma_g = 0.3$ chains/σ^2 in a bilayer of short matrix chains. (B) Branched structure obtained from the assembly of three species of NPs where the two end NPs are anti-symmetric and grafted at $\Gamma_g = 0.1$ chains/σ^2. Top and bottom panels show the top and side view, and insets show structures without grafts for better visualization of NP arrangement.

from the strong steric repulsion between grafts that prevents two dimers from simultaneously forming two contacts with each other, and assembling into a 2D bilayer. However, the repulsion is apparently weak enough to allow the dimers to form a single contact (though one of their NPs) resulting in a "chain" of tilted dimers connected by single bonds. The linear morphology of this chain as well as the alternating nature of these bonds going back and forth between the two layers also likely arise from steric repulsion that pushes neighboring dimers into orientations that maximize the separation distance between the two non-contacting NPs. The second structure, exhibiting a "branched" morphology (Fig. 3.7B), was achieved by the assembly of four open trimers composed of same three species of NPs used for assembling the trimers in Fig. 3.5C-E, *except* that the two end NPs had much smaller grafting densities ($\Gamma_g = 0.1$ chains/σ^2), causing them to adopt positions slightly above and below the interfacial plane; This effect together with strong steric repulsion between end NPs that pushes them apart likely led the trimers to adopt the highly obtuse configuration observed in the figure. Interestingly, because the two end NPs

of the trimer remain close to the interface, neighboring trimers could bind to each other in two ways: via end NPs in the same layer or via those on opposite layers. The former type of contact seems to permit interactions between two trimers, leading to the linear branches in the structure, while the latter apparently permits interactions between more than two trimers, leading to the branched node in the structure.

3.3 Conclusions

This study proposes and demonstrates through coarse-grained MD simulations a novel approach for assembling spherical NPs into anisotropic structures within a polymer matrix. The approach relies on two key ingredients—a polymer/polymer interface and polymer grafting of NPs—to break the underlying symmetry of an otherwise isotropic system of interacting particles. The polymer interface serves to introduce a finite-range, 1D harmonic field into the polymer matrix (first term in Eq. (3.1)) that, *independently*, would trap NPs at the interfacial plane. The grafts, when selective to one of the polymer layers, serve to introduce a linear field (second term in Eq. (3.1)), also of finite range, that displaces the harmonic trap away from the interface, the extent of which can be precisely controlled by the NP grafting density. The ability to trap multiple species of NPs differing in graft selectivity and/or graft density at distinct planes from the interface can then be used to assemble NPs into unique and tunable structures that go beyond the isotropic, maximally close-packed assemblies nominally obtained in the bulk or at interfaces. To illustrate the potential of this approach, we demonstrated the assembly of unique clusters, such as tilted dimers and open trimers with tunable orientations and bending angles, as well as unique quasi-1D and 2D phases, including serpentine and branched structures, hexagonally-arranged ridged monolayers, and square-packed interdigitated bilayers. We introduced a simple model to provide rapid predictions of the free energies and equilibrium positions of NPs based on experimentally accessible parameters. Such a model should provide useful guidance on trapping individual NPs at desired distances from the interface. Furthermore, this model, along with one

for NP-NP interaction energies, could be input into an energy-minimization algorithm to provide useful structure predictions on NP clusters and extended phases.

The ability of this approach to yield NP clusters with specific orientations or open configurations would be especially attractive for plasmonics. In this case, the NP cores could be made of a plasmonically-active metal like Ag or Au, and the NP clusters could be engineered via polymer grafting to be stable against further assembly and exhibit nanoscopic gaps between neighboring NPs. The most obvious benefit would be the unique plasmonic resonances that might emerge from such atypical non-contacting particle arrangements, with the additional possibility of unusual effects arising from clusters residing at the interface of two polymeric media with potentially different dielectric properties [95, 129]. Furthermore, the ability of the proposed approach to tune NP configuration could enable systematic studies of structure-property relationships. Similarly assembled unique clusters and phases of magnetic and semiconducting NPs would enable researchers to take advantage of unique magnetic and exciton couplings that emerge from such particle arrangements [59]. Other potential applications exist in the fields of solid-state catalysis, where catalytic NPs facilitating distinct reactions may be spatially organized into clusters to drive multi-stage reactions [130].

The proposed approach and results presented here open up new avenues for future studies. First of all, the higher-order structures demonstrated here likely constitute only a small subset of architectures conceivable by this approach. For instance, we examined only the simplest possible scenario of two anti-symmetric species of NPs to assemble quasi-2D structures, and again two or three closely-related NP species to assemble quasi-1D structures. We envision that using differently sized or grafted NPs and additional species of NPs has the potential to create a vast array of unique and interesting macroscopic phases. Similarly, it may be possible to assemble larger and more complex NP clusters (than the dimers and trimers demonstrated here) using a wider choice of polymer-grafted NP species. Second, the approach has so far been applied to spherical NPs in polymeric interfaces, but could be easily extended to other kinds of interfaces, such as those formed between oil and water, and to aspherical NPs. In the latter

scenario, we envision the interfacial forces to modulate not only the position of the NPs but also their orientation. Third, the quantitative model developed here for predicting equilibrium position of NPs could be further improved by accounting for the deformation of polymer grafts and the interface, which become severe when the NPs are located near the interface in the polymer layer incompatible with the grafts. Fourth, it would be instructive to study the translational and rotational dynamics of NPs and their clusters trapped at or near interfaces, which are expected to differ substationally from their dynamics in the bulk. Another topic that demands further examination is the role of multibody effects in the interfacial assembly of higher-order structures. These effects were cursorily used in this study to demonstrate assembly of quasi-linear structures, but its full potential in particle assembly at interfaces remains to be explored. Finally, the proposed assembly approach would need to be experimentally validated. Indeed, experiments have already successfully demonstrated the ability to prepare stable polymer bilayers from mutually immiscible polymers and to preferentially capture NPs within one of the layers [131]. Future experiments on the entrapment and asssembly of multiple species of NPs in such bilayers should reveal the possibilities and caveats of this interface-mediated NP assembly approach.

3.4 Supporting Information

3.4.1 Coarse-Grained Model

We used a coarse-grained (CG) representation to model both the polymer-grafted nanoparticles (NPs) and the polymer bilayer formed from the two mutually immiscible polymers. The grafted and matrix polymer chains, denoted by "g" and "p_1" and "p_2", were treated as Kremer-Grest bead-chains [79], in which polymer segments, typically a few monomers long, are represented by beads of size σ and mass m. The chain lengths of both matrix polymers were fixed at $L_p = 10$ segments (beads). The length of the grafts were varied in the range $L_g = 5\text{–}20$ segments, i.e., from half to twice as long as the matrix chains. The NP cores were treated as rigid spheres of radius $R_{NP} = 3\sigma$ and mass $m_{NP} = 216m$ (unless otherwise stated) with uniformly distributed grafting points across their surface. We explored grafting densities in the range $\Gamma_g = 0$ (bare NPs) to 0.4 chains/σ^2 (unless otherwise stated). Simple calculations based on *unperturbed* radii of gyration R_g^* of grafts (i.e. in the free state *not* attached to the NPs) yields fractional surface coverages $\Gamma_g R_g^{*2}$ of 0.1 to 1.85, indicating that we explored a range of grafting regimes, from mushroom to weak-brush regimes.

Adjacent beads along the chain representing bonded segments were connected to each other using a combination of a finitely extensible nonlinear elastic (FENE) spring and a Weeks-Chandler-Anderson (WCA) potential [80] :

$$U_b = U_{FENE} + U_{WCA}, \tag{3.2}$$

where the FENE potential ensures that the bonds between segments do not stretch beyond a given separation distance of $R_0 = 1.5\sigma$, and is given by

$$U_{FENE}(r; k, R_0) = -\frac{k}{2} R_0^2 \ln\left[1 - \left(\frac{r}{R_0}\right)^2\right], \tag{3.3}$$

where r is the distance between the bonded segments, $k = 30\varepsilon/\sigma^2$ is the spring constant, and ε is an energy parameter. The WCA potential is a short-range purely repulsive potential given by

$$U_{\text{WCA}}(r;\sigma,\varepsilon) \;=\; \begin{cases} 4\varepsilon\left[\left(\frac{\sigma}{r}\right)^{12} - \left(\frac{\sigma}{r}\right)^{6} + \frac{1}{4}\right] & r < 2^{1/6}\sigma \\ 0 & r \geqslant 2^{1/6}\sigma \end{cases}, \tag{3.4}$$

that accounts for the excluded volume interactions between the bonded segments.

The interactions between non-bonded segments, both intra- and inter-chain, were treated differently based on whether the parent chains were mutually miscible or immiscible, with the former exhibiting attractive interactions on top of excluded volume interactions and the latter exhibiting only excluded volume interactions, similar to approaches adopted in earlier studies [121–123, 132]. Chains of the same polymer type were considered miscible, and their segmental interactions were treated using a cut-and-shifted Lennard-Jones (LJ) potential

$$U_{\text{nb}}^{\alpha\text{-}\alpha} = U_{\text{LJ}}(r;\sigma,\varepsilon,r_{\text{c}}) \;=\; \begin{cases} 4\varepsilon\left[\left(\frac{\sigma}{r}\right)^{12} - \left(\frac{\sigma}{r}\right)^{6} - \left(\frac{\sigma}{r_{\text{c}}}\right)^{12} + \left(\frac{\sigma}{r_{\text{c}}}\right)^{6}\right] & r < r_{\text{c}} \\ 0 & r \geqslant r_{\text{c}} \end{cases}, \tag{3.5}$$

where $\alpha = $ g, p_1, and p_2, $r_{\text{c}} = 2.5\sigma$ is the cutoff distance of the potential, and ε represents the common strength of all such nonbonded interactions irrespective of chain type. Segments of the two polymer layers considered immiscible interacted with each other via the same WCA potential as that used for describing excluded volume interactions between bonded segments:

$$U_{\text{nb}}^{p_1\text{-}p_2} = U_{\text{WCA}}(r;\sigma,\varepsilon). \tag{3.6}$$

The grafts were generally considered to be compatible with one polymer layer and incompatible with the other. The former interactions were again treated using the LJ potential with an

intersegmental attraction strength of ε_g, and the latter using the WCA potential

$$U_{\text{nb}}^{\text{g-}\alpha} = \begin{cases} U_{\text{LJ}}(r;\sigma,\varepsilon_g,r_c) & \alpha \text{ is miscible} \\ U_{\text{WCA}}(r;\sigma,\varepsilon) & \alpha \text{ is immiscible} \end{cases}, \qquad (3.7)$$

where $\alpha = \text{p}_1$ or p_2; We explored values of ε_g between 0.5 and 2ε, i.e., from half to twice as strong as the attractive interactions between polymer segments of the same kind.

The excluded volume interactions between NP cores and the polymer segments were treated using an expanded WCA potential that accounts for the larger excluded volume of the cores (compared to polymer segments):

$$U_{\text{nb}}^{\text{NP-}\alpha} = U_{\text{WCA}}(r - r_{\text{ev}};\sigma,\varepsilon), \qquad (3.8)$$

where $\alpha = \text{g, p}_1$, and p_2, r is the distance between the center of the NP core and the polymer segment, and $r_{\text{ev}} \equiv R_{\text{NP}} - \sigma/2$ is a distance shift implemented to prevent the polymer segments from penetrating the NP core. The NP cores interact with each other via an expanded LJ potential

$$U_{\text{nb}}^{\text{NP-NP}} = U_{\text{LJ}}(r - 2R_{\text{NP}};\sigma,\varepsilon_{\text{NP}},r_c), \qquad (3.9)$$

where r is the distance between the centers of the cores of NP, $2r_{\text{NP}}$ shift prevents the NP cores from penetrating each other, and a strong attraction $\varepsilon_{\text{NP}} = 50\varepsilon$ was implemented to promote NP assembly. This attraction strength is consistent with the typical van der Waals interactions between small NPs

, and importantly, is also sufficiently strong to allow the NPs to overcome the steric repulsion arising from their grafts to assemble and weak enough to favor the formation of interfacial over bulk structures in the presence of an interface.The grafted chains were tethered onto the surface of the NP via FENE springs and with a pseudo-uniform distribution of grafting points at desired grafting density using the "generalized spiral points" algorithm of Rakhmanov

88

et al. [81].

Table 3.1 summarizes values of all the CG model parameters considered in this study. Note that all simulation parameters and quantities are defined in units of σ, m, and ε, which set the respective length, mass, and time scales in this study.

3.4.2 Molecular Dynamics Simulations

All molecular dynamics (MD) simulations of the NP-polymer system were carried out using the LAMMPS package [88] developed by the Sandia National Laboratory. The simulations were carried out in the canonical (NVT) ensemble at a temperature of $T = \varepsilon/k_B$ and a polymer-segment number density of $\rho = 0.85/\sigma^3$ in the polymer bulk. Under these conditions, the chains in each polymer layer are present in a melt-like state. A velocity-Verlet algorithm with a time step of $\Delta t = 0.002 \ (m\sigma^2/\varepsilon)^{1/2}$ was used for integrating the equations of motion, and a Nosé-Hoover thermostat with a time constant of $\tau = 1.0(m\sigma^2/\varepsilon)^{1/2}$ was used for regulating the system temperature. The polymer bilayer was confined in the z direction normal to the interface by two impermeable LJ walls, while periodic boundary conditions (PBCs) were implemented in the x and y directions parallel to the interface. The polymer layers were *each* chosen to have a thickness of $\Delta h = 15\sigma$ (or $\Delta h = 20\sigma$ for NPs with long grafts); Considering that the effective diameters of the NPs are roughly 6 to 12σ (depending on the length and extent of grafting), the polymer layers are sufficiently thick to capture the entire range of influence of the interface without distortion by the enclosing walls. Similarly, the simulation box was kept sufficiently large in the two lateral directions to ensure that a NP or its aggregate does not indirectly interact with itself via hydrodynamic flows (generated by NP mobility) propagated and reinforced through PBCs. Table 3.1 provides the size of simulation boxes considered in this study.

To carry out productive MD simulations for yielding meaningful data on NP dynamics, entrapment, self-assembly and free energies, we first generated well-equilibrated system of polymer-grafted NPs located at desired initial positions within a phase-separated polymer bilayer.

This was achieved by first placing the required number of NPs and matrix chains in a non-overlapping configuration in a simulation box 30 to 50 times larger than the required dimensions. To avoid overlaps, the grafts were arranged in straight, ground-state configurations perpendicular to the NP surface, the NPs were placed sufficiently far from each other, and the two types of matrix chains were organized into loose bundles of straight chains that were respectively placed above and below the NPs. Next, we assigned Maxwell-Boltzmann-distributed velocities to all segments and performed MD simulations for 0.1–0.4 million time steps, keeping the NP locations fixed at their initial positions. This allowed the grafted and matrix chains to randomize their configurations and also spread across the simulation box to form a uniform low-density matrix. Following this, we slowly compressed the simulation box over 1 million time steps until the required dimensions consistent with the target density ρ were achieved and the two matrix polymers phase-separated into a stable bilayer; Simultaneously, the NPs were gradually moved to their desired positions within the box. Finally, the system was simulated for an additional 1 million MD time steps, holding the particles fixed at their desired locations, to further equilibrate the system.

We carried out *two* different types of simulations following equilibration. First, we carried out equilibrium simulations of *freely-mobile* NPs within the bilayer for exploring the dynamics of individual NPs, especially their equilibrium positioning at or close to the interface, and for exploring the self-assembly of multiple such trapped NPs into higher-order structures. These simulations were generally started with NPs in the polymer layer most compatible with the NP grafts, specifically in the bulk region where the NPs "feel" neither the interface nor the wall, e.g., $z \sim \pm 5$–7σ. These simulations were typically performed for 12 million time steps and the trajectories of the NPs were recorded every 100 time steps.

Second, we carried out simulations of a single *constrained* NP at different fixed distances from the interface, which were used for computing the system free energy—the potential of mean force (PMF)—as a function of the normal coordinate z of the NP. In these simulations, the NP center was held fixed at equidistant points (spaced $\Delta z = 0.5$ apart) along a normal path

starting in the bulk region of one polymer layer at $z = -9\sigma$, crossing the interfacial plane at $z = 0$, and ending in the bulk of the second layer at $z = 9\sigma$ (or $z = -12\sigma$ to 12σ for NPs with longer grafts). The NP center was held fixed for 0.6 million time steps at each z location, and the ensemble-averaged normal force $\langle f_z(t) \rangle$ experienced by the NP was measured from the last 0.5 million time steps. All simulations was repeated four times to improve accuracy, yielding a total of $\sim$100 million time steps for the entire procedure. The PMF was then computed by integrating the force component over position as

$$\Delta F(z) \equiv F(z) - F(z_0) = -\int_{z_0}^{z} f_z(z) dz \qquad (3.10)$$

where z_0 represents a position in the bulk of the polymer layer most compatible with the NP grafts where the net force experienced by the particle is expected to be zero, i.e., $f_z(z_0) \sim 0$; In the case of bare NPs, the "reference" position z_0 can be present in either layers (which are both neutral to NP core). More details of this approach for computing PMFs are provided in our earlier publication [111].

3.4.3 Theoretical Model of NP Trapping

We seek a simple theoretical model to describe the observed (simulated) variation in the free energy (potential of mean force) of the NP-polymer system as a function of NP position z relative to the interface. To derive such a model, we consider a polymer-grafted NP residing in the bulk region of the polymer layer (say p_1) compatible with the NP grafts (Fig. 3.9a). The *interfacial* free energy F_0 of this system is given by the sum of the free energy of the unperturbed interface between the two polymer layers and the free energy of the interface present between the NP grafts and the surrounding matrix polymer:

$$F_0 = A_{\text{int}}\gamma_{p_1\text{-}p_2} + A_{\text{sph}}\gamma'_{g\text{-}p_1}, \qquad (3.11)$$

where A_{int} is the area of the planar interface between the two matrix polymers p_1 and p_2, A_{sph} is the area of the spherical interface between the NP grafts and the matrix polymer p_1, $\gamma_{p_1\text{-}p_2}$ is the interfacial tension between the two matrix polymers, and $\gamma'_{g\text{-}p_1}$ is the surface energy per unit area between the grafts and matrix p_1. Note that we used the prime symbol here to differentiate it from the traditional interfacial tension that is applied to interfaces formed between free polymer chains.

We next consider moving the NP center to a distance z from the interfacial plane, a position sufficiently close for the NP to intersect it (Fig. 3.9b). This movement leads to a reduction in the interfacial area between p_1 and p_2 by an amount equal to the circular crosssectional area of the grafted NP at $z = 0$; we denote this area by A_{circ}. The NP movement also leads to the introduction of a new interface between NP grafts and the incompatible matrix p_2 resembling a spherical cap with an area we denote by A_{cap}. Note that this area also represents the amount of interface lost between the grafts and the compatible matrix p_1. The total interfacial free energy of this new configuration is then given by

$$F(z) = (A_{\text{int}} - A_{\text{circ}}(z))\gamma_{p_1\text{-}p_2} + (A_{\text{sph}} - A_{\text{cap}}(z))\gamma'_{g\text{-}p_1} + A_{\text{cap}}(z)\gamma'_{g\text{-}p_2} \qquad (3.12)$$

where $\gamma'_{g\text{-}p_2}$ represents the surface energy of the newly introduced graft-p_2 interface.

The free energy change associated with moving the NP from the bulk of the compatible polymer layer p_1 to a position at or close to the polymer/polymer interface is then simply given by

$$\Delta F(z) \equiv F(z) - F_0 = -A_{\text{circ}}(z)\gamma_{p_1\text{-}p_2} + A_{\text{cap}}(z)(\gamma'_{g\text{-}p_2} - \gamma'_{g\text{-}p_1}), \qquad (3.13)$$

where the first term represents a favorable contribution from the NP occluding part of the unfavorable polymer/polymer interface, and the second term represents an unfavorable contribution caused by the replacement of part of the favorable graft-mediated interactions with the compatible chains of p_1 for unfavorable interactions with the incompatible chains of p_2 across the interface.

To obtain the two area terms in Eq. (3.12), we consider the grafted NPs to have "effective" radii R' larger than the core radius R_{NP} based on two observations from our simulations. First, analysis of polymer density around the NPs reveals strong layering (adsorption) of polymer segments around the NP cores, irrespective of whether the NPs are bare or grafted (Fig. 3.10). Second, the computed free energy profiles in Fig. 3.2 indicate that NPs begin to "feel" the interface over normal distances considerably farther than the 3σ distance predicted from the NP core radius. We found that $R' = 4.95\sigma$ provides a better representation of the effective size of these NPs. The circular area A_{circ} occluded by the NP can then be obtained as

$$A_{circ}(z) = \pi r^2 = \pi(R'^2 - z^2),\tag{3.14}$$

and the curved surface area of the spherical cap A_{cap} is given by

$$A_{cap}(z) = \pi(r^2 + h^2) = \pi((R'^2 - z^2) + (R' + z)^2) = 2\pi R'(R' + z),\tag{3.15}$$

where r is the radius of the circular crosssection and h is the height of the spherical cap (Fig. 3.9c). Substituting these two area contributions into Eq. (3.13) yields our final model:

$$\Delta F(z) = -\pi(R'^2 - z^2)\gamma_{p_1-p_2} + 2\pi R'(R' + z)\Delta\gamma'_{g-p},\tag{3.16}$$

where we have used the short notation $\Delta\gamma'_{g-p}$ to denote $\gamma'_{g-p_2} - \gamma'_{g-p_1}$, the difference in the surface energy of the grafts interacting with the two polymers layers. Note that the above free energy expression is only valid when the NP intersects the interfacial plane, i.e., $-R' < z < R$. For $z \leqslant -R'$, the interfacial free energy is equal to F_0, and therefore $\Delta F(z) = 0$. For $z \geqslant R'$, the free energy difference is entirely contributed by the grafts, and given by the difference in the surface energy of the grafts in the two polymer layers, or in other words, $\Delta F(z) = 4\pi R'^2 \Delta\gamma'_{g-p}$.

3.4.4 Surface-Tension Calculations

The model fits of the free energy profiles in Fig. 3.3 yielded best-fit values of the surface energies $\gamma_{p_1\text{-}p_2}$ and $\Delta\gamma'_{g\text{-}p}$. We take a closer look at the magnitudes of the two fitted quantities. The obtained value of $\gamma_{p_1\text{-}p_2} = 1.35\ k_B T/\sigma^2$ is reasonable when compared to the surface tensions of 1–10 mN/m measured between weakly and strongly immiscible polymers [133]; For instance, assuming room temperature and segment sizes on the order of a nanometer, one obtains $\gamma_{p_1\text{-}p_2} \approx 5.6$ mN/m for our CG system. We also tested how well the fitted value of $\gamma_{p_1\text{-}p_2}$ matched against that estimated from the Helfand-Tagami theory [134], according to which

$$\gamma_{p_1\text{-}p_2} = (\chi_{p_1\text{-}p_2}/6)^{1/2}\sigma\rho_0 k_B T, \tag{3.17}$$

where $\chi_{p_1\text{-}p_2}$ is the Flory-Huggins parameter that quantifies the incompatibility of the two polymers, σ is the effective size of a polymer segment, and ρ_0 is the number density of these segments in the bulk polymer. The Flory-Huggins parameter can be calculated using the standard relationship

$$\chi_{p_1\text{-}p_2} = z\Delta w/k_B T, \tag{3.18}$$

where z is the average coordination number of the polymer segments (beads) in the two layers, and $\Delta w \equiv \varepsilon_{p_1\text{-}p_2} - \frac{1}{2}(\varepsilon_{p_1\text{-}p_1} + \varepsilon_{p_2\text{-}p_2})$ is an energy parameter describing the *net* interaction energy associated with forming a contact between unlike polymer segments, i.e., p_1 and p_2. Using the value of $z \approx 12.5$ obtained from simulations of the polymer bilayer at $T = \varepsilon/k_B$, and the values of $\varepsilon_{p_1\text{-}p_2} = 0$, $\varepsilon_{p_1\text{-}p_1} = \varepsilon_{p_2\text{-}p_2} = -\varepsilon$ prescribed by our CG model, we obtained $\gamma_{p_1\text{-}p_2} = 1.23 k_B T$ via Eqs. 16 and 17. The model-fitted value of $\gamma_{p_1\text{-}p_2} = 1.35 k_B T$ obtained from our simulations thus agrees quite well with both experiments and with estimates from theory.

The obtained $\Delta\gamma'_{g\text{-}p}$ values are all smaller than $\gamma_{p_1\text{-}p_2}$ and increase with grafting density. Since the chains of the compatible matrix are chemically identical to the grafts (so $\gamma'_{g\text{-}p_1} \sim 0$), the magnitude of $\Delta\gamma'_{g\text{-}p}$ arises primarily from $\gamma'_{g\text{-}p_2}$ associated with the interactions between the grafts

and the incompatible matrix. Hence, the small value of $\Delta\gamma'_{g-p}$, and of γ'_{g-p_2}, seems reasonable given that graft-matrix interface has a lower density of graft segments than matrix chain segments at the polymer/polymer interface. The increase in $\Delta\gamma'_{g-p}$, and in γ'_{g-p_2}, with grafting density Γ_g also makes sense with denser grafting leading to larger number of unfavorable contacts with the matrix and hence larger surface energy γ'_{g-p_2}. Ideally, a proportional increase in $\Delta\gamma'_{g-p}$ with Γ_g might be expected. Instead, we find that the increase exhibits a weaker dependence (Fig. 3.3D) that is better described by a powerlaw

$$\Delta\gamma'_{g-p} \approx 1.29\gamma_{p_1-p_2}\Gamma_g^{0.66}, \tag{3.19}$$

suggesting an increased tendency of the grafted chains to extend themselves towards the compatible polymer layer and avoid the incompatible layer with increasing grafting density.

Table 3.1: Details of simulation systems examined in this study.

$L_g{}^a$	$L_m{}^b$	$\Gamma_g{}^c$	$n_g{}^d$	$n_m{}^e$	V^f
Isolated NPs					
5–20	10	0.1–0.4	11–45	2206–6496	27000–80319
NP dimers					
5	10	0.1–0.4	11–45	2196-2150	27000
NP trimers					
5	10	0.04–0.3^g	5–34	4245-4232	53905
Higher-order structures					
5	10	0.1–0.3	11–34	4368–6552	54010–81031

^{a}Length of grafted chains. ^{b}Length of matrix chains. ^{c}Grafting density. ^{d}Number of grafted chains per NP. ^{e}Number of matrix chains in simulation box. ^{f}Volume of simulation box. ^{g}Values pertain to NP3 only. For NP1 and NP2, we used $\Gamma_g = 0.52$ and 0.32, and $n_g = 59$ and 16, respectively.
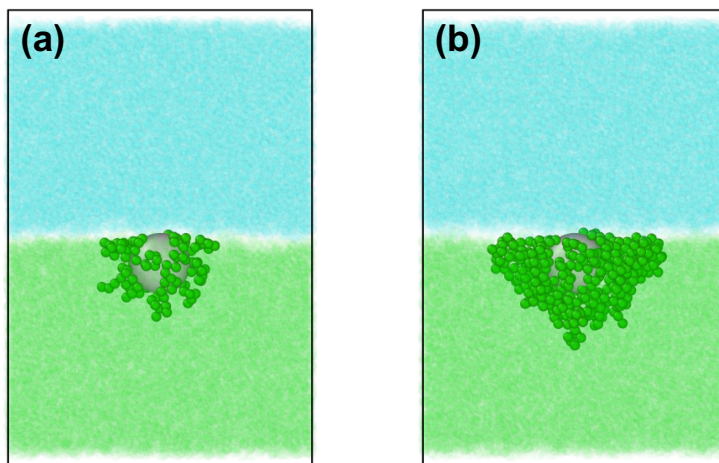
Figure 3.8: Representative configurations of grafted NPs, with two different graft lengths of (a) $L_g = 5$ and (b) $L_g = 10$ beads, located at their respective equilibrium positions in the bilayer (at $z \approx -2.5\sigma$ from the interfacial plane). The flexible polymer grafts contort themselves to maximize (minimize) contact with the compatible (incompatible) layer.
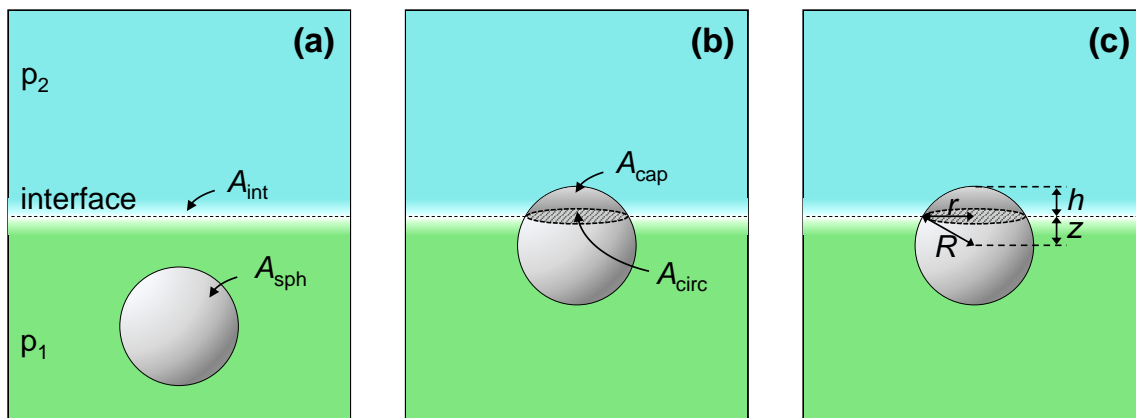
Figure 3.9: Cartoons showing key aspects of our theoretical model for predicting NP positions and free energies. (a) polymer-grafted NP completely immersed in the bulk of polymer layer p_1 showing the two relevant polymer interfaces and their associated areas A_{int} and A_{sph}. (b) NP intersecting the interfacial plane highlighting its area A_{circ} occluded by the NP and the area A_{cap} of the new interface formed between the grafts and p_2. (c) Radius of the circular crosssection r and height h of the spherical cap formed by the intersection of the NP with the interface.
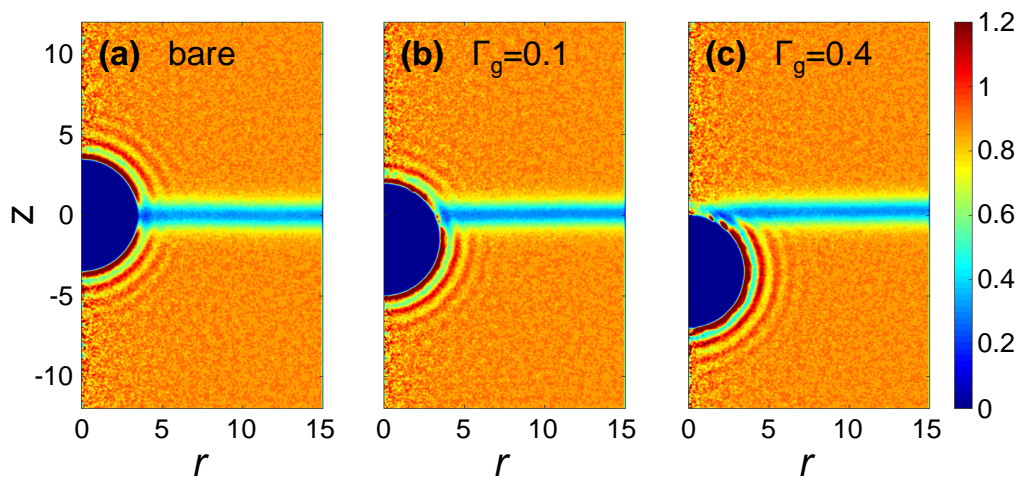
Figure 3.10: Contour maps of the *overall* polymer segment density $\rho_{\mathrm{g+m}}(r,z)$ around bare and grafted NPs located at their minimum-free-energy position z_{m}. The density maps are shown for NPs at three different grafting densities: (a) $\Gamma_{\mathrm{g}} = 0.0$ (bare), (b) $\Gamma_{\mathrm{g}} = 0.1$, and (c) $\Gamma_{\mathrm{g}} = 0.4$ beads/σ^2. The ring-shaped density peaks around the NP cores suggest strong layering of polymer segments. Color bar denotes the density in units of segments/σ^3. Positions r and z are defined as described in Fig. 3.8 caption.
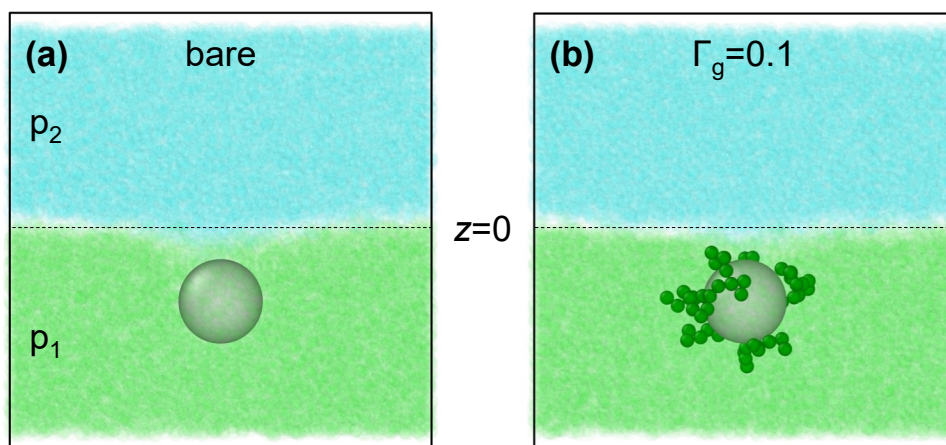
Figure 3.11: Representative simulated configurations of (a) bare NP, and (b) NP grafted with chains at density 0.1 beads/σ^2 placed at $z = -5\sigma$ showing some deformation of the interface even when the particles are "far" from the interface ($|z| > R_{\mathrm{NP}} = 3\sigma$).
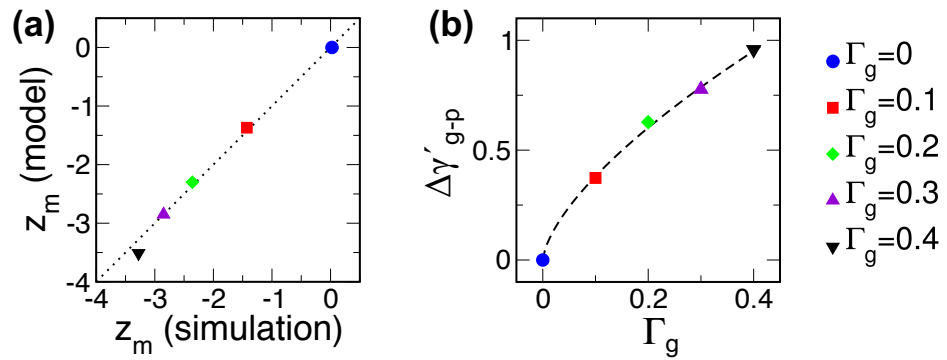
Figure 3.12: (a) Equilibrium positions z_m of NPs predicted by the theoretical model compared against those obtained from simulations. Black dotted line denotes perfect-agreement line. (b) Surface energy $\Delta\gamma'_{g\text{-}p}$ values obtained from model plotted as a function of grafting density. Black dashed line denotes a power-law fit to the data.

Figure 3.13: Equilibrium tilt-angles θ predicted by the model for NPs at different grafting densities (as specified in plot) compared against angles measured from simulations. Black dotted line denotes perfect-agreement line.

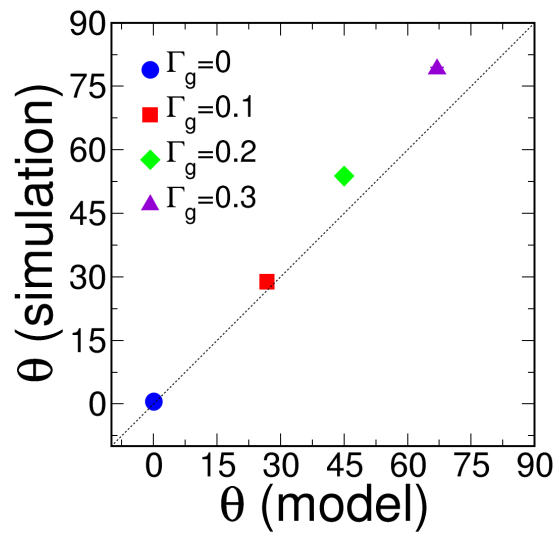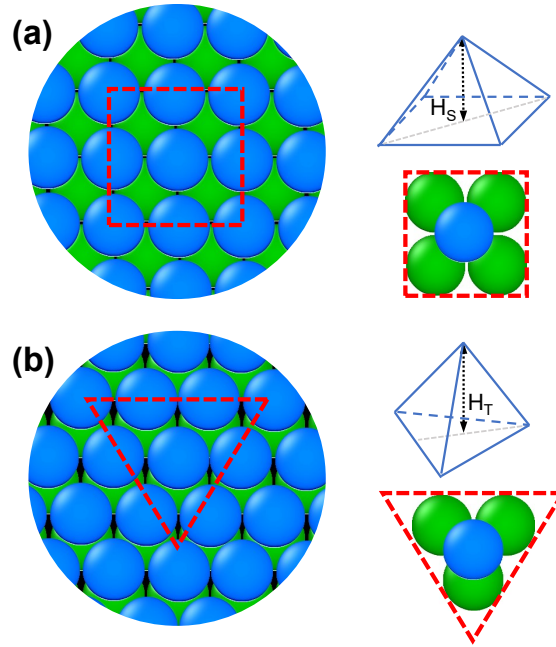**Figure 3.14**: Schematics showing particle arrangements in (a) square-ordered bilayer and (b) hexagonal-ordered bilayer. Red dashed lines enclose the underlying square-pyramidal and tetrahedral arrangement of NPs in the square and hexagonal bilayers. The vertical heights of the square pyramid and tetrahedron, as denoted by H_S and H_T, provide the separation distance between the two layers of NPs. The distances between the centers of the NPs forming each side of the square base in the square pyramid and the triangular base in the tetrahedron are both equal to $R^* \approx 6.12\sigma$. From geometry, the heights of the square pyramid and the tatrahedron are then given by $H_S = R^*/\sqrt{2} \approx 4.33\sigma$ and $H_T = \sqrt{2/3}R^* \approx 5.0\sigma$. The NP layers in the square and hexagonal bilayers are therefore located roughly $\pm 4.33\sigma/2 = \pm 2.16\sigma$ and $\pm 5.0\sigma/2 = \pm 2.5\sigma$ from the interfacial plane, respectively.
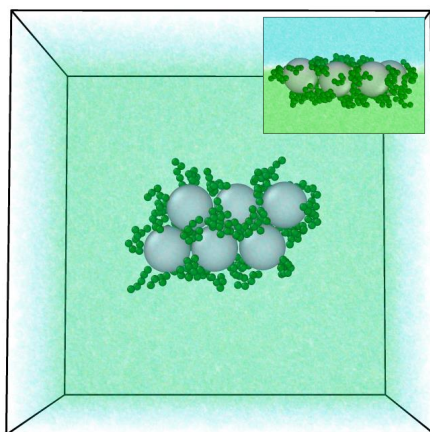
Figure 3.15: Representative configuration of a hexagonal-ordered monolayer obtained from simulations of 6 polymer-grafted NPs at a polymer interface. All NPs were grafted with chains miscible and immiscible with the bottom and top polymer layers, respectively. Inset shows the structure from a view parallel to the interface.
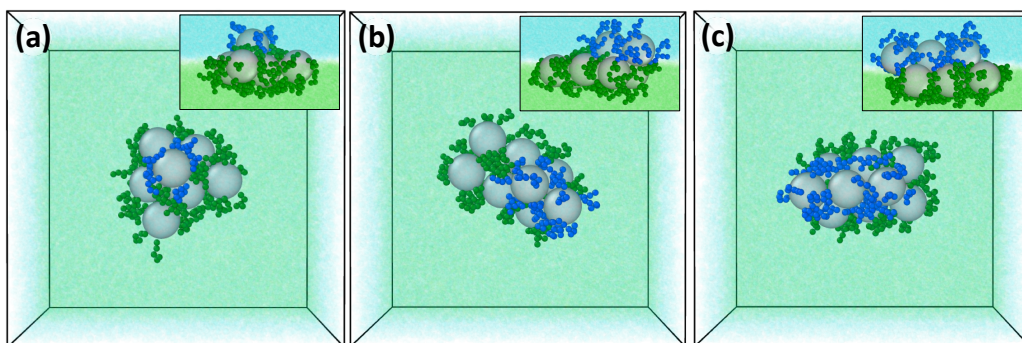
Figure 3.16: Representative configuration of structures obtained from the assembly of unequal numbers of the two anti-symmetric NP species grafted at $\Gamma_g = 0.1$ chains/σ^2. Structures obtained from particle number ratios of (A) 1:6, (B) 2:6, and (C) 3:6 are shown. Inset shows the structure from a view parallel to the interface.
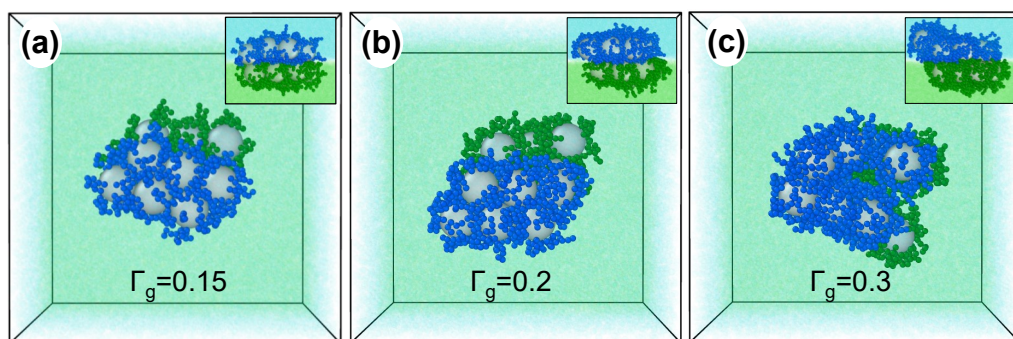
Figure 3.17: Representative configurations of higher-order structures obtained from simulations of 12 NPs with grafting densities of (a) 0.15, (b) 0.2, and (c) 0.3 beads/σ^2 in a polymer bilayer. Half of the NPs are grafted with chains miscible to polymer layer p_1, and the other half are grafted with chains miscible to p_2. Insets show the structures from a view parallel to the interface.

3.5   Acknowledgments

Chapter 4

# One-Dimensional Anomalous Diffusion of Gold Nanoparticles in a Polymer Melt

4.1 Introduction

Functionalized metal nanoparticles (NPs) dispersed in a polymer matrix are of considerable interest scientific and technological. Dilute dispersions of NPs in polymers can serve as a unique microrheological probe of the dynamics of the host polymer matrix, while at higher concentrations polymer nanocomposites (PNCs) are formed, which can exhibit a variety of complex thermal, mechanical, rheological, plasmonic, optical and electrical properties [95, 104, 135–141]. Ensuring effective dispersion of the NPs is one of the key issues in synthesizing PNCs [142]. Consequently, the motion of the functionalized NPs in the embedding matrix is also of intrinsic interest because it reveals how the NPs disperse at a microscopic level inside the polymer when it is in the melt state.

It is known that functionalized nanoparticles introduced into a polymer matrix show several different regimes of diffusion, ranging from classic Brownian motion to highly anomalous diffusion depending on the degree of entanglement of the chains anchored to the NP's with the host polymer chain [143–158]. Of particular interest is the regime where the nanoparticle

size is comparable to the mesh size, which is the case explored here. Dynamical measurements may be made using multi-speckle dynamic light scattering (DLS) [143], photoluminescence or fluorescence correlation spectroscopy [144, 145] or its X-ray analog, known as X-ray photon correlation spectroscopy (XPCS) [146–156]. For NPs in polymer solutions, subdiffusive behavior has been observed [144, 149]. For polystyrene (PS) melts, Guo et al. [152] found normal hydrodynamic diffusion of Au NPs at high temperatures for host matrices of low to intermediate MW, while a crossover to hyperdiffusion with ballistic-like motion occurred as the temperature was lowered to below $\sim$1.1 T_g. Similar behavior was seen for alumina NPs in Polymethyl-methacrylate (PMMA) host matrices [151]. This behavior may be attributed to the onset of glassy behavior in the host matrix. Narayanan et al. studied the dynamics of Au NPs at the surface of thin films of PS at temperatures well above T_g and observed almost normal diffusion when the host matrix had a MW of 30 Kg/mole but ballistic-like motion for higher MW host PS chains [154].

In DLS or XPCS experiments, one measures the normalized scattered intensity autocorrelation function

$$g_2(\mathbf{q},t) = \frac{\langle I(\mathbf{q},t')I(\mathbf{q},t'+t)\rangle}{\langle I(\mathbf{q},t')\rangle^2} = 1 + A|f(\mathbf{q},t)|^2 \tag{4.1}$$

where $I(q,t)$ is the scattered intensity at time t, q is the wave vector transfer, the averages are over time t', and A ($0 < A < 1$) is the instrumental coherence factor (with $A = 1$ for complete coherence of the beam). $f(q,t)$ is the normalized intermediate scattering function (ISF) related to the Fourier transform of the scattering function $S(q, \omega)$ and for uncorrelated particles is given by

$$f(\mathbf{q},t) = \frac{1}{N}\sum_i \left\langle e^{-i\mathbf{q}\cdot\mathbf{r}_i(0)} e^{i\mathbf{q}\cdot\mathbf{r}_i(t)} \right\rangle \tag{4.2}$$

where $r_i(t)$ is the position of particle i at time t and the bracket denotes an ensemble average. For studies of the motion of NPs in polymers, the ISF generally has been fit with the form (isotropic in q)

$$f(\mathbf{q},t) = Ce^{-(t/\tau(q))^\beta} \qquad (4.3)$$

where for normal diffusion, the exponent $\beta = 1$ where D is the diffusion constant and $\tau(q)$ $=[Dq^2]^{-1}$. The hyperdiffusive behavior observed previously for Au NPs in PS melts in certain regimes is usually associated with $\beta > 1$ and $\tau(q) = [Vq]^{-1}$, where V has the dimensions of a velocity related to a "drift velocity" of the NP, acquired due to the release of stresses at random locations in the host matrix, as is believed to occur in jammed systems. An oscillatory g_2 function can arise from uniform convective motion of the nanoparticles, if the scattered beam were heterodyning with some static reference beam [159–161], or in homodyning from shear flow [162], or a symmetric particle velocity distribution with a predominant magnitude of drift velocity. From Eq. (4.2),

$$\begin{aligned}
f(\mathbf{q},t) &= \frac{1}{N}\sum_i \left\langle e^{i\mathbf{q}\cdot[\mathbf{r}_i(t)-\mathbf{r}_i(0)]} \right\rangle = \frac{1}{N}\sum_i \left\langle e^{i\mathbf{q}\cdot\mathbf{v}_i t} \right\rangle \\
&= \frac{1}{N}\sum_i \left\langle e^{i\mathbf{s}\cdot\mathbf{v}_i} \right\rangle = \int d\mathbf{v} P(\mathbf{v}) e^{i\mathbf{v}\cdot\mathbf{s}}
\end{aligned} \qquad (4.4)$$

where the vector variable qt has been defined by s and $P(v)$ is the velocity distribution for the particles. If $P(v)$ is peaked around one particular magnitude of the velocity v, this will give rise to an oscillatory $f(q,t)$[1]. From Eq. (4.4), $P(v)$ can be obtained from the Fourier transform of $f(q,t)$ with respect to s. In this case, Fourier transforming $f(q,t)$ can yield the distribution of particle drift velocities [159, 163], as illustrated below. In several previous studies, β was found to be dependent on both q and temperature, and in some cases $\tau(q)$ was found to crossover between the forms given above at some values of q [146, 154]. Possible anisotropies in the particle motion or oscillatory g_2 functions have never been explored previously in the case of NPs in polymers.

In the present work, our collaborators, Sinha et al., report the results of XPCS studies

---

[1] Since $g_2(q, t)$ is $|f(\mathbf{q},t)|^2$, a complex oscillatory $f(q,t)$ will yield a constant. However, a symmetrical velocity distribution will yield a real $f(q,t)$, and thus an oscillatory g_2 function.

of functionalized Au NPs dispersed in molten PS that illustrates several such novel features, including anisotropy effects, drift velocities, and the effect of stress in the host polymer network. To validate the experimental observations, we present the results of molecular dynamics simulations, which agree well with these experimental results and demonstrate the intermittent random ballistic-like motion seen here.

4.2   Experimental Approach

The volume fraction of the NPs was very small, so as to minimally perturb the host polymer. Two different sizes of Au NPs (13 nm and 18 nm diameter), were densely grafted with ligands of linear PS of MW 38 Kg/mole to prevent aggregation, and dispersed at a volume concentration of 0.5% in host matrices of linear PS of MWs of 13 Kg/mole ($T_g \sim$ 90C), 30 Kg/mole and 97 Kg/mole ($T_g \sim$ 100C) respectively, were studied as a function of temperature. The high grafting density of the ligand chains (see Supporting Information) implies that they form a brush and thus only the 13 Kg/mole host matrix chains can penetrate and wet the NPs [164, 165].

The ligand-grafted NPs were mixed in solution and films were cast, embedding the NPs in the polystyrene matrix. The mixture was then loaded into a flat stainless-steel sample container (shown schematically in Supporting Information) with a circular opening. After the sample was loaded into the cavity, Kapton windows were attached, using Momentive RTV106 high temperature adhesive, to seal the sample. The samples were annealed at 180C in vacuum in 2 different orientations (illustrated in Sup. Fig. 4.5) for more than one day (24 hours) before performing the XPCS measurements. In orientation A, the thermal gradient is along the plate-like sample parallel to the long edge of the sample container (henceforth referred to as the z-axis). For the other orientation the thermal gradient was along the x-axis, i.e. normal to the flat face of the sample (orientation B in Sup. Fig. 4.5). XPCS experiments were performed at beamline 8-ID-I of the Advanced Photon Source at Argonne National Laboratory using 7.35 keV X-rays.

Measurements were made for sample temperatures between 120C and 170C, where thermal degradation is not expected to be significant. Some preliminary XPCS experiments carried out on this system of NPs at the LCLS XFEL have been published previously [166].

For most XPCS measurements, the intensity auto-correlation function $g_2(q,t)$ is averaged over all directions of q in the y-z plane (see Sup. Fig. 4.5) with the same magnitude q, on the assumption of dynamical isotropy, to improve statistical accuracy of counting. In the present experiment however, the pixels in the 2D detector were grouped into 36 pie-shaped sectors, each subtending an angle of $10°$ at the center, and whose mean direction to the vertical is given by the angle ϕ. $\phi = 0$ corresponded to the direction parallel to the z-axis, i.e. long edge of the sample container. The g_2 functions were averaged in each sector over pixels corresponding to a magnitude of q within ranges $\pm\Delta q$, where $\Delta q = 9.6\times10^{-4}$ Å^{-1}. Thus, we measured the functions $g_2(q, \phi, t)$.

The XPCS studies begin by discussing measurements made on samples annealed in orientation A (see section 4.6.1). These samples show a progression from normal to anomalous diffusion as the chain length of the PS in the host matrix is increased. For the 18nm Au NPs in the host matrix of MW 13 Kg/mole at 160C the (g_2-1) functions showed no dependence on sector angle at any temperature, i.e. were isotropic, and could be described by a single exponential for $f(q, t)$, with relaxation times $\tau \sim q^{-2}$ as expected for normal Brownian motion, yielding a value of $D = 4450$ Å^2/sec for the diffusion constant at 160C (see Sup. Fig. 4.6 in Supporting Information). Then the Einstein-Stokes relation yields for a particle with hydrodynamic radius 9 nm a viscosity of $\sim 8\times10^3$ Poise which is close to the measured viscosity for PS with MW 13 Kg/mole at 160C [167]. This implies normal diffusion in an isotropic viscous fluid, as the host polymer chains can penetrate the ligand brush.

Figure 4.1(a) shows the functions $(g_2 - 1)$ measured for the 18 nm Au NPs in the host matrix of MW 30 Kg/mole (close to the entanglement MW) at 160C for $q = 9\times 10^{-3}$Å^{-1} for several different angular sectors. One can see that these functions are oscillatory, but that the period of the oscillation is independent of sector angle ϕ so that they are functions only of the
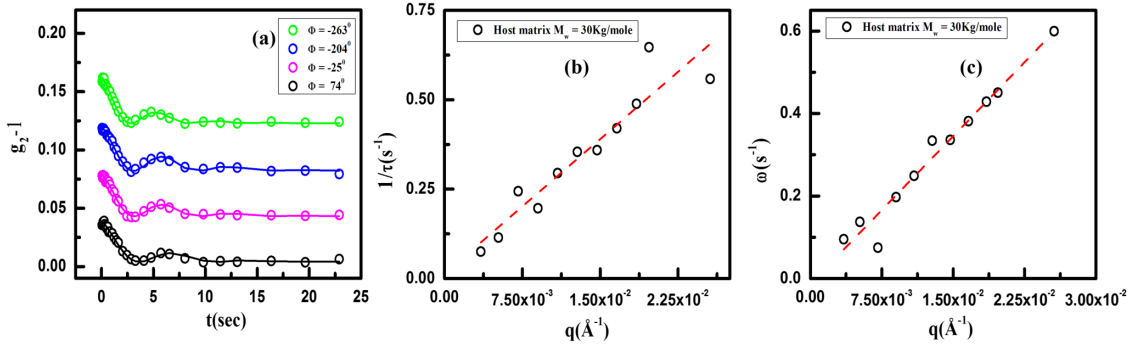
Figure 4.1: (a) Isotropic (g_2 - 1) functions for 18 nm gold particle in host Matrix MW=30 Kg/mole for $T = 160C$ and $q = 9 \times 10^{-3} \text{Å}^{-1}$. The curves have been vertically displaced for clarity. (b) $1/\tau$ vs q and (c) ω vs q for the above mentioned system.

magnitude of q.

For the data shown in Fig.4.1(a), $f(q,t)$ can be well described, for all q values, sectors and temperatures in terms of a form for $f(q,t)$ given by:

$$f(q,t) = Ae^{-(t/\tau)^\beta}\cos(\omega t) \tag{4.5}$$

where β turns out to have a value of ~ 1.8, independent of q and almost temperature independent (see Table 4.1 in Supporting Information). Thus the NP motion is isotropic and $\beta > 1$ indicates that it is hyperdiffusive. The prefactor A also turned out to be essentially independent of q, temperature and sample and has a value consistent with the instrumental coherence factor, implying that there is no "escape from a cage" at very short timescales [155, 158]. For the above system they find that $\tau = (1/v_1)q^{-1}$ and $\omega = v_2q$, where v_1 and v_2 are constants (see Figs. 4.1(b) and 4.1(c)). This corresponds to a ballistic motion of the NPs, with v_2 representing the peak velocity and v_1 the width of the distribution.These turn out to be dependent on temperature and the size of the NP. Similar results were found for the 13 nm diameter NPs.

Next they present results for the host matrix consisting of chains of MW 97 Kg/mole. The dynamics they observed for this case were strikingly different for samples annealed in the horizontal (B) and in the vertical (A) orientations. For the samples containing 18 nm Au NPs annealed in orientation B, the results are very similar to those reported above for the 30 Kg/mole
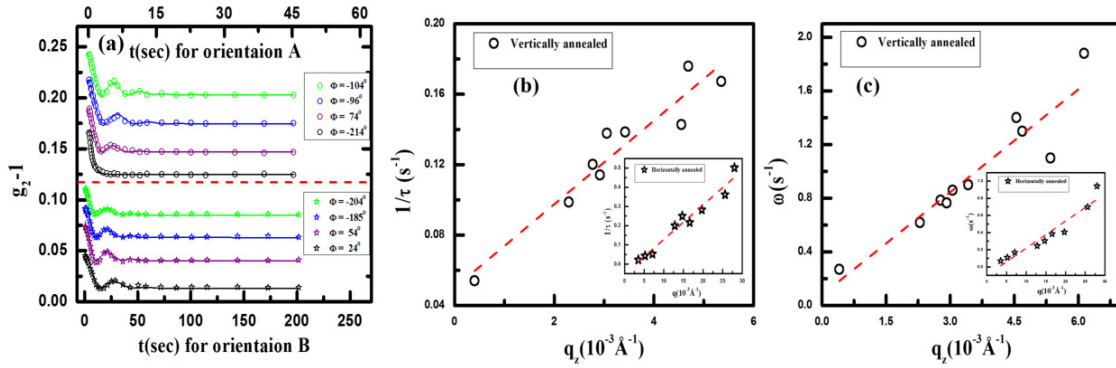
Figure 4.2: (a) Relaxation dynamics in terms of g_2 - 1 as a function of τ at different angles ϕ at T=160 C and q=9$\times$ 10^{-3} Å^{-1} for sample of 97 Kg/mole host matrix with nanoparticle diameter 18 nm annealed in orientation A ($\circ$) and orientation B ($\star$), plotted with 2 different time scales as shown. The curves have been vertically displaced for clarity. Dependence of (b) $1/\tau$ and (c) ω as a function of q_z (= $q\cos\phi$) at T=160 C for 18 nm Au NPs annealed in orientation A. Inset panels in fig (b) and (c) represent the cases of samples at orientation B as a function of q.

MW host matrix, with isotropic, oscillatory (g_2-1) functions which can be fit with Eq. (4.5). For these samples $\beta \approx$2, implying a Gaussian spatial self-correlation function for the diffusing particle with a width that increases linearly with time, as expected for ballistic motion.

However, the results for samples annealed in orientation A for the same host matrix of MW 97 Kg/mole are very different. Figure 4.2(a) shows the functions (g_2-1) for the 18 nm Au NPs for both annealing orientations for $q = 9\times10^{-3}$ Å^{-1} for several different sector angles ϕ. It can be seen that for this orientation these functions are also oscillatory, but in this case the period of the oscillation varies with ϕ. They can be well fitted for all q values, sector angles ϕ and temperatures, with the form for $f(\boldsymbol{q}, t)$ given by Eq. (4.5), where τ=$(1/v_1)$ $(q \cos\phi)^{-1}$ and ω = $v_2 q \cos\phi$. Note that $(q \cos\phi)$ is simply q_z the component of $\boldsymbol{q}$ along the z-axis. Thus in this case $f(\boldsymbol{q},t)$ may be rewritten as

$$f(q,t) = Ae^{-(v_1 q_z t)^{\beta}} \cos(v_2 q_z t) \tag{4.6}$$

This corresponds to one-dimensional ballistic motion along the z-axis, with v_1 and v_2 representing 2 characteristic velocities, which are temperature dependent. By Eq. (4.4), the velocity distributions can be obtained from the Fourier transform of $f(\boldsymbol{q},t)$. Figure 4.3 show
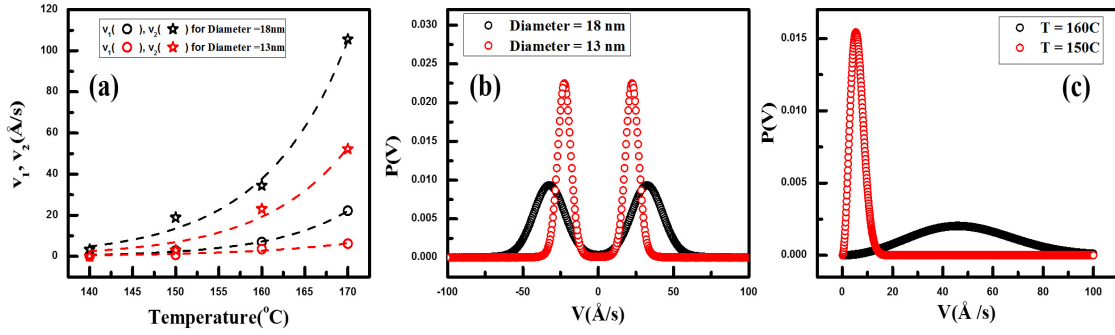
Figure 4.3: The variations of (a) v_1 and v_2 for the 13nm and 18nm Au NPs samples with 97 Kg/mole host matrix annealed in orientation A, as a function of temperature. Velocity distributions at T=160 C for NPs in (b) 97Kg/mole and (c) 18nm Au NPs in the 30Kg/mole host matrices annealed in orientation A.

the isotropic velocity distribution of the 18 nm NPs between v and $(v+dv)$ in the 30 Kg/mole MW host matrix, the velocities v_1 and v_2 for the 13 nm and 18 nm Au NPs as a function of temperature, and the corresponding one-dimensional distributions of particle velocities along the z-axis obtained by Fourier transforming $f(q_z,t)$ in the 97 Kg/mole MW host matrix, for samples annealed in orientation A. Paradoxically, the larger NPs have higher drift velocities. They argue that this may be due to the fact that the host matrix chains penetrate even less into the larger NPs which have a higher density of grafted ligand chains, thus providing less resistance to drift motion. In order to confirm this very unusual anisotropic motion of NPs, they repeated these experiments on new but similar samples after a reasonable interval of time, with identical results.

These distributions peak at $v = \pm v_2$. The present results show that the particle motion can be described statistically in terms of a one-dimensional Levy flight [168], with a random distribution of jump lengths, and a drift velocity along the z-axis between jumps, i.e. a Levy walk [169], on a time-scale typically longer than the range of time scales measured for $g_2(\boldsymbol{q},t)$, with a distribution of velocities around $\pm v_2$. This distribution can be described statistically by a Levy stable distribution [163, 168, 169]. As shown in the Supporting Information, $P(v\text{-}v_2)$ behaves asymptotically as $(v\text{-}v_2)^{-(1+\beta)}$ as expected for Levy stable distributions. They hypothesize that the one-dimensional motion of the NPs arises from the dynamic alignment of the polymer chains of the host matrix along the z-axis due to the NP motion along the direction of heat flow, during

115

the thermal annealing process in orientation A, as discussed below.

4.3   Modeling and Simulations of Nanoparticle Diffusion

To test the above hypothesis, we conducted molecular dynamics simulations of a gold NP diffusing in a polymer melt that is relaxing from a state with pre-aligned polymer chains in the z-direction (see Supporting Information for details of calculations) [79–82]. In particular, we examined 2 systems: a single PS-grafted (MW $\sim$ 38 Kg/mol) NP diffusing within an unentangled PS matrix (with short chains of MW $\sim$ 13 Kg/mol) and in an entangled PS matrix (with long chains of MW $\sim$ 143 Kg/mol). During the simulations, the mean squared displacement (MSD) of the NP and its components along the *x*, *y*, and *z* directions were calculated. We also calculated the ISF *f(q, t)* defined in Eq. (4.2) for values of $q = (2\pi/L)(n_x, n_y, n_z)$; n_x, n_y, n_z are integers, and *L* is the size of the simulation box (which was taken to be as large as possible, i.e. 55σ, where σ is the bead size. See Supporting Information). This is at least 5 times larger than the hydrodynamic size of the polymer-grafted NP.

We performed calculations of *f(q,t)* with *q* along the *x*, *y*, *z* directions (which we label $f_{1,x}, f_{1,y}$, and $f_{1,z}$ respectively) with n_x, n_y, n_z ranging from 1 to 6. (Values < 1 correspond to wavelengths incompatible with the periodic boundary conditions). In the short-chain PS system, simulations demonstrate a linear trend of the overall MSD with t and almost equivalent values of the MSD in the *x*, *y* and *z* directions (Fig. 4.4(a)) suggesting normal isotropic diffusive behavior of the NP, as observed experimentally. However, in the higher MW system, the MSD curves are proportional to t^2 over most of the time scale investigated, which corresponds to ballistic motion (Fig. 4.4(b)), though they eventually become linear at much longer times. The *x*, *y* components of the MSD are very small, while the *z* component is almost identical to the total MSD, implying highly anisotropic motion of the NP along the z-direction. (In the Supporting Information section, we discuss how the length- and time-scales of the simulations can be mapped onto the length- and time-scales of the experimental measurements).
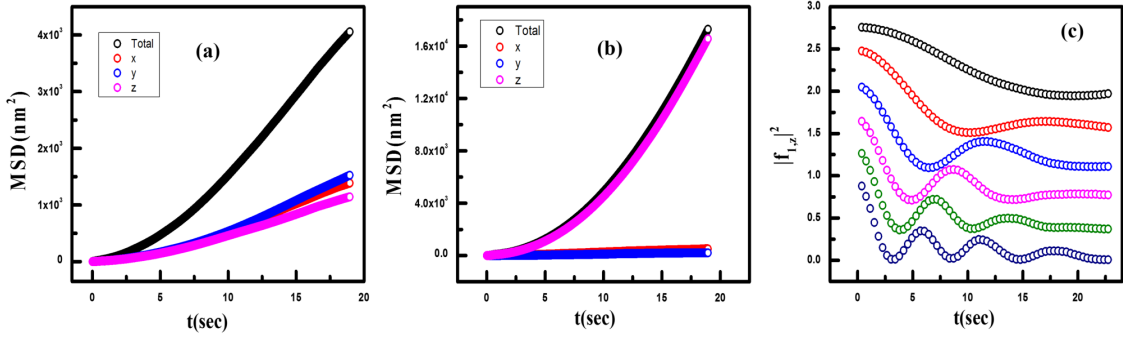
Figure 4.4: Mean square displacement (MSD) and ISF computed from simulations. (a) Overall MSD as a function of time and its x, y, z components of gold NP in MW = 13 Kg/mol polymer host matrix. (b) Overall MSD and its x, y, z components and (c) ISF modulus square $|f_{1,z}|^2$ as a function of t(sec) of gold NP in MW = 143 Kg/mol polymer host matrix. All f_1 curves are normalized and shifted vertically. Here, $q\,(n) = 2\pi n/(55\times45)$ Å^{-1}.

Interestingly, the simulations also show damped oscillatory behavior of the $f_{1,z}$ curves with time, for different values of q_z (Fig. 4.4(c)), which agree with what is observed experimentally in terms of the number of oscillations observed, the positions and amplitudes of the oscillations, and the overall range of time scales. Our simulation reveals ballistic motion with velocities v_{sim} $\approx$ 71 Å/s in the same range as the experiments $v_{exp} \approx$ 38 Å/s. The reason that v_{sim} is higher than v_{exp} is likely because the system temperature in the simulations was held fixed at $T \approx$ 485 K while it was $T \approx$ 434 K in the experiments.

Note that an oscillatory f_1 does not imply oscillatory motion of these particles, but rather confirms the drift like motion. However, following the motion of the particle in the simulations did indicate frequent reversals of the direction of motion of the particle. The corresponding $f_{1,xy}$ curves decay without significant oscillation, indicating that the ballistic motion of the NP is confined to the z direction only. It confirms that this anisotropic motion of the NP can be replicated only in the high molecular weight PS host matrix. Although a rigorous theory is lacking, it is likely that the ballistic motion of the NPs through the higher MW chains of the host matrix (which cannot penetrate the ligand chain brushes on the NPs) is due to thermal gradients and/or release of stresses caused by local distortions in the network. In the case of the 97 Kg/mole host matrix, and samples annealed in orientation A, where the thermal gradient is

along the z-axis, this motion can cause dynamical alignment of the host matrix chains. This can be seen by considering the Weissenberg number [170] for this situation given by $Wi = (v_2/D)\tau_m$ where the first factor is the shear rate (v_2 being the NP velocity, D its diameter) and τ_m is the terminal chain relaxation time. Inserting appropriate values for the latter for the 97 Kg/mole PS chain [171], we find $Wi \geqslant 1$, which can result in chain alignment, as observed, with the particles drifting in both directions along the aligned chains. For the 30 Kg/mole PS chains with faster relaxation times or samples annealed in position B (with no strong thermal gradient), such alignment does not occur, and the resulting motion is isotropic. Movies of the simulation of the motion of the NP within the host polymer matrices may be accessed online (see Supporting Information).

4.4   Conclusions

In summary, our collaborators and us have discovered cases of novel highly anisotropic ballistic motion with characteristic drift velocities for densely grafted functionalized Au NPs moving in high molecular weight polymer melts. We believe that the cause is dynamical alignment of the chains by the NPs as they move driven by thermal gradients and release of stresses in the network, but to our knowledge, there has been no theory to account for ballistic motion of NPs in polymer networks. The theoretical treatment of Bouchaud and Pitard of jammed colloidal particles moving due to the release of elastic stresses in the medium, characterized by $\beta > 1$ and $\tau \approx q^{-1}$ [172] may be more appropriate to the present case. However, it is remarkable that all these phenomena, are semi-quantitatively reproduced by the molecular dynamics simulations reported here. Together, the experimental measurements and simulations provide a detailed description of anomalous NP motion in an entangled polymer network.

4.5   Supporting Information

4.5.1   XPCS details

Sup. Fig. 4.5 shows schematically how the samples were loaded into the container and annealed prior to the XPCS measurements. Initial annealing of the samples was carried out prior to the scattering measurements in a vacuum oven at a temperature of 180C in two orientations A and B shown (see Sup. Fig. 4.5) where the heat flow was respectively along and normal to the face of the thin sample holder as shown. Before the XPCS measurements, small angle X-ray scattering (SAXS) patterns were measured for each sample. The scattering could be described with the squared form factor of the gold nanoparticles, as expected for well-separated gold particles, together with increased scattering at smaller q values. To ensure that the latter was not due to aggregated clusters of the nanoparticles, we verified that the same scattering occurred in a polymer melt without Au NPs, indicating that this was due to large length scale heterogeneities in the polymer itself.

Sup. Fig. 4.6 shows the results for the 18 nm PS-grafted Au NPs in the lowest MW host matrix of 13 Kg/mole PS, showing normal isotropic diffusion.
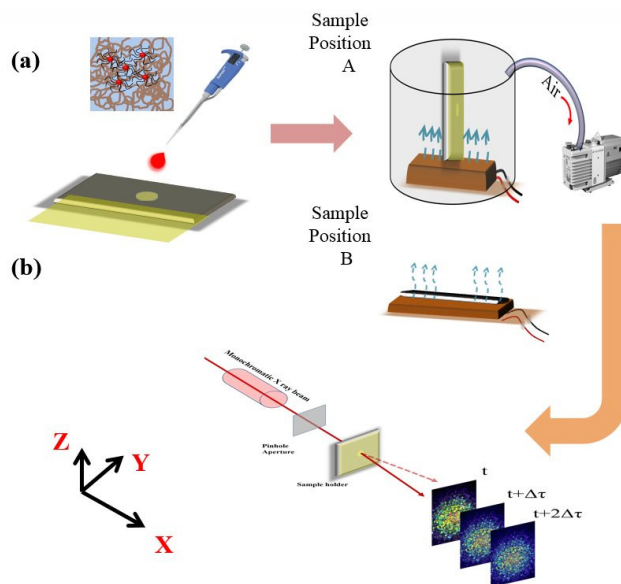
Figure 4.5: (a) Illustration describes the detailed procedure of experiments including loading polymer nanocomposite(PNC) melt into the kapton window sealed sample holder and annealing vertically (Orientation A) and horizontally (Orientation B) under high vacuum at temperature higher than the T_g of the sample. (b) Schematic elucidates the X-ray Photon Correlation Spectroscopy (XPCS) beamline setup used for this measurement.
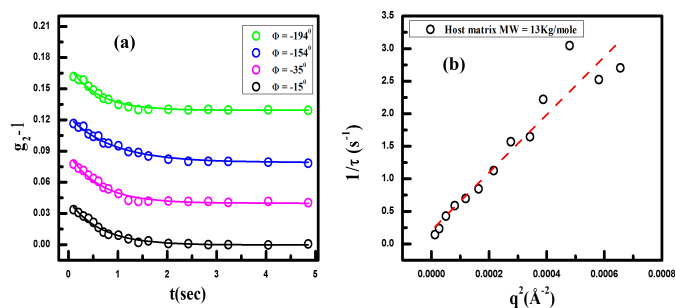
Figure 4.6: (a) (g_2-1) as a function of delay time (t) with different φ's at temperature T = 160C & q = 9×10^{-3} Å^{-1} for vertically annealed samples of 18 nm nanoparticles grafted with 38 Kg/mole PS ligands in polymer matrix of MW 13 Kg/mole showing relaxation in terms of (b) Variation of (1/τ) vs q^2 shows pure diffusional motion for the same system.

4.5.2 Derivation of Particle Velocity Distributions.

(a) Ballistic motion; Isotropic case:-

Since τ and ω are $\sim q^{-1}$, The function f($\mathbf{q}$,t) given in Eq. (4.7) of the paper is a function only of the single variable qt, which is denoted by s, and can be related to the particle velocity distribution P(v) by Eq. (4.8) of main text so the reverse Fourier transformation yields, for the function W(v), the probability of the velocity being between v and (v+dv),

$$W(v) = 4\pi v^2 P(v) = \frac{2Av}{\pi} \int_0^\infty dss e^{-(v_1 s)^\beta} \cos(v_2 s) \sin(vs) \tag{4.7}$$

(b) Ballistic motion; Anisotropic case:-

The function f($\mathbf{q}$,t) in this case is a function of the single variable q_zt which is denoted by s, and may be Fourier inverted to yield a one-dimensional distribution of particle velocities along the z-axis between v and (v+dv)

$$\begin{aligned} W(v) &= \frac{1}{\sqrt{2\pi}} \int_{-\infty}^\infty ds e^{-ivs} e^{(-v_1 s)^\beta} \cos(v_2 s) \\ &= \frac{2}{\sqrt{2\pi}} \int_0^\infty ds \cos(vs) e^{(-v_1 s)^\beta} \cos(v_2 s) \end{aligned} \tag{4.8}$$

This corresponds to the characteristic function of the Levy stable distribution $L_{\mu,o}$[169] shifted around th evelocity v_2, where $\mu=\beta$. Sup. Fig. 4.7 shows a double logarithmic plot of this velocity distribution showing that its asymptotic form is $(v-v_2)^{-(1+\beta)}$ as expected from the theory of Levy stable distributions [169].

4.5.3 Molecular Dynamics Simulations

To investigate the anisotropic diffusion of gold NP, we performed molecular dynamics simulations of a polymer-grafted NP diffusing in both nonentangled and entangled PS polymer
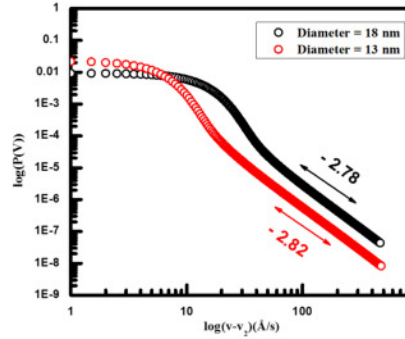
Figure 4.7: $(v\text{-}v_2)^{-(\mu+1)}$ asymptotic behavior of velocity distribution at 160C for two different gold nanoparticle sizes. The numbers on the plot indicate the power laws of the two curves.

Table 4.1: The parameters obtained from fitting of XPCS data for samples at T=160C with different nanoparticle size, host matrix and annealing conditions.

Annealing condition	Nanoparticle diameter (nm)	Host matrix molecular weight(Kg/mole)	β	A	v_1 (Å/s)	v_2 (Å/s)
Orientation A (Vertical)	18	13	1.0	0.037 ±0.003	$D \sim 4450$ Å^2/s	
Orientation A	18	30	1.73 ± 0.07	0.038 ±0.001	11.95	27.6
Orientation A	13	97	1.80 ± 0.05	0.053 ±0.004	3.56	23.1
Orientation A	18	97	1.88 ± 0.05	0.037 ±0.003	6.96	34.4
Orientation B(Horizontal)	18	97	1.98 ± 0.06	0.044±0.003	1.85	20.1

melts. A coarse-grained (CG) model was adopted for improving computational efficiency [79], where PS segments are treated as beads of size σ and mass *m*. Due to computational limitations, we used a large size mapping factor by setting 1σ=4.5nm. The excluded volume interaction between each pair of polymer segment was treated using a short-range, purely repulsive (WCA) potential [80]:

$$U_{\text{ev}} = \begin{cases} 4\varepsilon \left[\left(\frac{\sigma}{r}\right)^{12} - \left(\frac{\sigma}{r}\right)^{6} + \frac{1}{4} \right] & r \leqslant 2^{1/6}\sigma \\ 0 & r > 2^{1/6}\sigma \end{cases}, \qquad (4.9)$$

where *r* is the distance between the segments. For those adjacent polymer segments in the same chain, a finitely extensible nonlinear elastic (FENE) spring was applied to connect them with potential energy given by

$$U_{\text{FENE}} = -\frac{k}{2}R_0^2 \ln \left[1 - \left(\frac{r}{R_0}\right)^2 \right], \qquad (4.10)$$
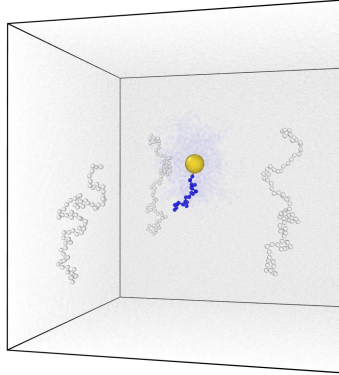
Figure 4.8: Snapshot of Molecular Dynamics Simulation with a PGNP and its trajectories inside a periodic box.

where r is the distance between the bonded segments, R_0 is the maximum possible length of the spring, $k=30\varepsilon/\sigma^2$ is the spring constant, and ε sets the energy scale of the system. The NPs were also treated using CG model as spheres of diameter $D_{NP}=4\sigma$, consistent with the 18nm NPs used experimentally. The excluded volume interactions between NPs and polymer segments were treated using an WCA expanded potential:

$$
U_{\text{WCA-expand}} \quad = \quad
\begin{cases}
= 4\varepsilon \left[\left(\dfrac{\sigma}{r - r_{\text{ev}}} \right)^{12} - \left(\dfrac{\sigma}{r - r_{\text{ev}}} \right)^{6} + \dfrac{1}{4} \right] & r - r_{\text{ev}} \leqslant 2^{1/6}\sigma \\
= 0 & r - r_{\text{ev}} > 2^{1/6}\sigma
\end{cases}
\qquad (4.11)
$$

where r is the distance between the centers of NP and polymer segments. $r_{ev} = (D_{NP} - \sigma)/2$ is a distance shift that prevents the polymer segments and the NP from penetrating each other. The grafted chains were tethered onto the surface of NPs also by using FENE springs, and with pseudouniform distribution of grafting points at desired grafting density using the "generalized spiral points" algorithm of Rakhmanov et al. [81, 82].

A rough mapping scheme provided by Kremer and Grest for PS melts suggests that each

polymer bead corresponds to a PS segment of MW $\sim$ 515 g/mole and length $\sim$ 1.26 nm, while a reduced temperature of T = 1 corresponds to $\sim$ 485 K [79]. Accordingly to this mapping scheme, our experimental system should yield very long bead-chains and large NPs, whose simulations are beyond our computational capability, in spite of the CG representation. To this end, we chose to simulate systems 3.6 times smaller or shorter than the experimental system, and then used a scaling approach to extrapolate our results to the larger experimental system. Subsequently, the 18-nm NPs were represented by spheres of $D_{NP} = 4\sigma$ and the 38 Kg/mole PS grafts were represented by CG bead-chains containing 20 beads. Similarly, the 13 Kg/mole, 30 Kg/mole, and 97 Kg/mole chains studied experimentally should be represented by 7-, 16-, and 52-beads long CG chains. However, because the onset of chain entanglement in the Kremer-Grest model occurs at N $\sim$ 50 beads, we chose to use slightly longer chains containing 78 beads corresponding to 143 Kg/mole PS matrix to ensure that our CG polymer melt fell in the entanglement regime. For the representative short-chain host matrix, we chose to use the 13 Kg/mole PS chains that were studied experimentally.

To test the hypothesis that the anomalous diffusion of gold NP arises from the interactions with vertically aligned PS chains due to thermal annealing, each simulation was started from a non-overlapped configuration of a single NP surrounded by vertically aligned PS host matrix chains in a large simulation box employing periodic boundary conditions (PBCs). The initial condition was meant to provide a way to produce slightly more aligned chains compared to completely isotropic system. The box was then quickly compressed to a reasonable polymer melt-like density 0.85 n_{beads}/V_{beads}, where n_{beads} is the total number of the polymer beads in the simulation box, and V_{beads} is the volume occupied by the polymer beads. Each dimension of the simulation box was set to a large size to suppress anomalous propagation of hydrodynamic effects through PBCs and allow exploration of low q-values in g_1 calculations. Once the polymer melt-like density was reached, 1 million time steps would be given to the system for polymer relaxation, and the calculation of g_1 and MSD would be performed afterward, while the polymer host matrix chains remain preferentially vertically aligned. Each simulation was performed for

10 million time steps. To rationally map the simulation time τ to real timescale, we compared the diffusion coefficients of gold NP in the shortest PS host matrix system acquired respectively in simulation (1.69×10^{-1} nm^2/τ) and experiment (44.5 nm^2/s). If the simulation replicates the dynamics of the experiment system well, it should provide a similar value. By comparing the results, we obtained that $1\tau = 3.80 \times 10^{-3}$ s, which effectively scales the time frame of simulation into experimental time frame as observed. The snapshot of particle trajectory is shown in Sup. Fig. 4.8 and complete trajectories of PGNP in both lower and higher molecular host matrix are uploaded as separate supplementary movies.

4.6 Acknowledgments

Chapter 5

Conclusion and Future Work

In this dissertation, we explored the intriguing phenomenon of nanoparticle (NP) self-assembly, particularly in how one could create anisotropic assemblies using NPs that are inherently isotropic. We began by investigating the role of polymer-mediated interactions between NPs in the formation of anisotropic structures comprised of spherically-symmetric polymer-grafted NPs. The polymer-mediated portion of the potential of mean force (PMF) and three-body contribution were both found to be highly anisotropic. This anisotropy was shown to arise from the expulsion of polymer grafts from in between the dimer NPs, which provides direct support for the hypothesis that the anisotropic interactions could arise from the conformational rearrangement of grafted chains at the contact region. The overall PMF also allowed us to compute the free energies of formation of two- and three-particle clusters, yielding a phase diagram analogous to that observed experimentally. Next, we proposed a novel approach for assembling spherical nanoparticles into anisotropic architectures in a polymer matrix. The approach relies on two key ingredients: the interfacial tension between two mutually immiscible polymers forming a bilayer that serves to trap NPs within two-dimensional planes parallel to the interface; and the differences in the compatibility of the two polymer layers with polymer grafts on particles introduce a linear field that displaces the harmonic trap away from the interface. We demonstrated the viability of the proposed approach in both trapping NPs at tunable distances from the interface

and assembling them into a variety of unusual nanostructures, such as dimers with tunable tilt and trimers with tunable bending angle, as well as anisotropic macroscopic phases, including serpentine and branched structures, ridged hexagonal monolayers, and square-ordered bilayers. We also developed a theoretical model to predict the preferred positions and free energies of NPs trapped at or near the interface that could help guide the design of polymer-grafted NPs for achieving target NP architectures. Lastly, we investigated the dynamics of polymer-grafted gold nanoparticles loaded into polymer melts. Our collaborators experimentally discovered cases of novel highly anisotropic ballistic motion with characteristic drift velocities for densely grafted functionalized Au NPs moving in high molecular weight polymer melts, which they hypothesized is caused by the dynamical alignment of the chains by the NPs as they move driven by thermal gradients and release of stresses in the network. We performed molecular dynamics simulations of a single gold nanoparticle diffusing in a partially aligned polymer network to test this hypothesis and reveal very similar anisotropic ballistic motion of NP in the higher molecular weight system. We also performed calculations of normalized intermediate scattering function from the simulations that quantitatively agree with that observed experimentally. Our simulations were able to reproduce the experimental results to a remarkable degree and provide direct support to the above hypothesis.

An interesting result found in our computed phase diagram of isotropic versus anisotropic 3-particle clusters was that it revealed possible existence of a hidden stable dimer phase within a small window of parameter space, where the 2-particle PMF exhibits an attractive minimum while the 3-particle PMF is purely repulsive due to the polymer redistribution effect. It would be interesting to experimentally test the existence of such a phase and to further investigate and map out its precise location within the grafting parameter space. We also envision the proposed approach of trapping NP at the interface has potential to create a vast array of other unique and interesting macroscopic phases. For instance, by including multiple tilted dimers and carefully tailoring their interactions and conformational rearrangement of the graft polymers, one may be able to confine the assembly of dimers in one-dimensional space and achieve quasi

one-dimensional structures such as staggered, zig-zag, crisscross, or even helix NP wires. One could also employ the idea of creating open angle trimer but instead use unequal number of NPs with different sizes on different sides of the interface to create asymmetric clusters, and assemble them into superlattices with different patterns and periodicities on either side of the interface. In addition, this approach can be used to trap not only spherical NPs but also shaped NPs such as cubes, ellipsoids, and rods accompanied by orientation changes. Indeed, we have observed in preliminary work via molecular dynamics simulations that nanocube equilibrium orientation can be tuned to achieve face-up, vertex-up, and edge-up configurations simply by adjusting the properties of the grafted polymers. We have also observed an interesting phenomenon where multiple dispersed nanocubes in one polymer layer can inhibit the aggregation of nanocubes in another layer, resembling observations made experimentally by our collaborators. All these topics will require further investigation both experimentally and through simulations to fully understand the mechanisms. In summary, this dissertation has opened up new avenues to assemble nanoparticles into unconventional anisotropic architectures with potential applications in advanced polymer nanocomposites.

Bibliography

[1] David P Fromm, Arvind Sundaramurthy, P James Schuck, Gordon Kino, and WE Moerner. Gap-dependent optical coupling of single "bowtie" nanoantennas resonant in the visible. *Nano letters*, 4(5):957–961, 2004.

[2] Katrin Kneipp, Yang Wang, Harald Kneipp, Lev T Perelman, Irving Itzkan, Ramachandra R Dasari, and Michael S Feld. Single molecule detection using surface-enhanced raman scattering (sers). *Physical review letters*, 78(9):1667, 1997.

[3] PJ Schuck, DP Fromm, A Sundaramurthy, GS Kino, and WE Moerner. Improving the mismatch between light and nanoscale objects with gold bowtie nanoantennas. *Physical review letters*, 94(1):017402, 2005.

[4] Carsten Sönnichsen, Björn M Reinhard, Jan Liphardt, and A Paul Alivisatos. A molecular ruler based on plasmon coupling of single gold and silver nanoparticles. *Nature biotechnology*, 23(6):741, 2005.

[5] Bunyamin Karagoz, Lars Esser, Hien T Duong, Johan S Basuki, Cyrille Boyer, and Thomas P Davis. Polymerization-induced self-assembly (pisa)–control over the morphology of nanoparticles for drug delivery applications. *Polymer Chemistry*, 5(2):350–355, 2014.

[6] Tito Trindade, Paul O'Brien, and Nigel L Pickett. Nanocrystalline semiconductors: synthesis, properties, and perspectives. *Chemistry of Materials*, 13(11):3843–3858, 2001.

[7] Andrew N Shipway, Eugenii Katz, and Itamar Willner. Nanoparticle arrays on surfaces for electronic, optical, and sensor applications. *ChemPhysChem*, 1(1):18–52, 2000.

[8] Marie-Christine Daniel and Didier Astruc. Gold nanoparticles: assembly, supramolecular chemistry, quantum-size-related properties, and applications toward biology, catalysis, and nanotechnology. *Chemical reviews*, 104(1):293–346, 2004.

[9] Eric A Appel, Mark W Tibbitt, Matthew J Webber, Bradley A Mattix, Omid Veiseh, and Robert Langer. Self-assembled hydrogels utilizing polymer–nanoparticle interactions. *Nature communications*, 6:6295, 2015.

[10] Younjin Min, Mustafa Akbulut, Kai Kristiansen, Yuval Golan, and Jacob Israelachvili. The role of interparticle and external forces in nanoparticle assembly. In *Nanoscience And*

Technology: A Collection of Reviews from Nature Journals, pages 38–49. World Scientific, 2010.

[11] Rui Chen, Noel T Nuhfer, Laura Moussa, Hannah R Morris, and Paul M Whitmore. Silver sulfide nanoparticle assembly obtained by reacting an assembled silver nanoparticle template with hydrogen sulfide gas. *Nanotechnology*, 19(45):455604, 2008.

[12] Faisal A Aldaye and Hanadi F Sleiman. Sequential self-assembly of a dna hexagon as a template for the organization of gold nanoparticles. *Angewandte Chemie International Edition*, 45(14):2204–2209, 2006.

[13] Frank Caruso, Marina Spasova, Veronica Salgueiriño-Maceira, and LM Liz-Marzán. Multilayer assemblies of silica-encapsulated gold nanoparticles on decomposable colloid templates. *Advanced Materials*, 13(14):1090–1094, 2001.

[14] Li-Tang Yan and Xu-Ming Xie. Computational modeling and simulation of nanoparticle self-assembly in polymeric systems: Structures, properties and external field effects. *Progress in Polymer Science*, 38(2):369–405, 2013.

[15] Shu-Chun Yang, Hiromu Kobori, Chieh-Lun He, Meng-Hsien Lin, Hung-Ying Chen, Cuncheng Li, Masayuki Kanehara, Toshiharu Teranishi, and Shangjr Gwo. Plasmon hybridization in individual gold nanocrystal dimers: direct observation of bright and dark modes. *Nano letters*, 10(2):632–637, 2010.

[16] Fumin Huang and Jeremy J Baumberg. Actively tuned plasmons on elastomerically driven au nanoparticle dimers. *Nano letters*, 10(5):1787–1792, 2010.

[17] Tanya Shirman, Talmon Arad, and Milko E Van Der Boom. Halogen bonding: a supramolecular entry for assembling nanoparticles. *Angewandte Chemie*, 122(5):938–941, 2010.

[18] Kensuke Naka, Hideaki Itoh, and Yoshiki Chujo. Temperature-dependent reversible self-assembly of gold nanoparticles into spherical aggregates by molecular recognition between pyrenyl and dinitrophenyl units. *Langmuir*, 19(13):5496–5501, 2003.

[19] Weihai Ni, Ricardo A Mosquera, Jorge Pérez-Juste, and Luis M Liz-Marzán. Evidence for hydrogen-bonding-directed assembly of gold nanorods in aqueous solution. *The Journal of Physical Chemistry Letters*, 1(8):1181–1185, 2010.

[20] Mark A Olson, Ali Coskun, Rafal Klajn, Lei Fang, Sanjeev K Dey, Kevin P Browne, Bartosz A Grzybowski, and J Fraser Stoddart. Assembly of polygonal nanoparticle clusters directed by reversible noncovalent bonding interactions. *Nano letters*, 9(9):3185–3190, 2009.

[21] Rafal Klajn, Mark A Olson, Paul J Wesson, Lei Fang, Ali Coskun, Ali Trabolsi, Siowling Soh, J Fraser Stoddart, and Bartosz A Grzybowski. Dynamic hook-and-eye nanoparticle sponges. *Nature chemistry*, 1(9):733, 2009.

[22] Chad A Mirkin, Robert L Letsinger, Robert C Mucic, and James J Storhoff. A dna-based method for rationally assembling nanoparticles into macroscopic materials. *Nature*, 382(6592):607, 1996.

[23] A Paul Alivisatos, Kai P Johnsson, Xiaogang Peng, Troy E Wilson, Colin J Loweth, Marcel P Bruchez Jr, and Peter G Schultz. Organization of 'nanocrystal molecules' using dna. *Nature*, 382(6592):609, 1996.

[24] Mathew M Maye, Dmytro Nykypanchuk, Marine Cuisinier, Daniel Van Der Lelie, and Oleg Gang. Stepwise surface encoding for high-throughput assembly of nanoclusters. *Nature materials*, 8(5):388, 2009.

[25] Colin J Loweth, W Brett Caldwell, Xiaogang Peng, A Paul Alivisatos, and Peter G Schultz. Dna-based assembly of gold nanocrystals. *Angewandte Chemie International Edition*, 38(12):1808–1812, 1999.

[26] Sung Yong Park, Abigail KR Lytton-Jean, Byeongdu Lee, Steven Weigand, George C Schatz, and Chad A Mirkin. Dna-programmable nanoparticle crystallization. *Nature*, 451(7178):553, 2008.

[27] Yi Chen, Haipeng Liu, Tao Ye, Junghwa Kim, and Chengde Mao. Dna-directed assembly of single-wall carbon nanotubes. *Journal of the American Chemical Society*, 129(28):8696–8697, 2007.

[28] Ji-Young Kim and Jae-Seung Lee. Synthesis and thermally reversible assembly of dna-gold nanoparticle cluster conjugates. *Nano letters*, 9(12):4564–4569, 2009.

[29] Nathaniel L Rosi, C Shad Thaxton, and Chad A Mirkin. Control of nanoparticle assembly by using dna-modified diatom templates. *Angewandte Chemie*, 116(41):5616–5619, 2004.

[30] Dongyuan Zhao, Qisheng Huo, Jianglin Feng, Bradley F Chmelka, and Galen D Stucky. Nonionic triblock and star diblock copolymer and oligomeric surfactant syntheses of highly ordered, hydrothermally stable, mesoporous silica structures. *Journal of the American Chemical Society*, 120(24):6024–6036, 1998.

[31] Ward A Lopes and Heinrich M Jaeger. Hierarchical self-assembly of metal nanostructures on diblock copolymer scaffolds. *Nature*, 414(6865):735, 2001.

[32] Wei Ma, Hua Kuang, Liguang Xu, Li Ding, Chuanlai Xu, Libing Wang, and Nicholas A Kotov. Attomolar dna detection with chiral nanorod assemblies. *Nature communications*, 4:2689, 2013.

[33] Wei Ma, Hua Kuang, Libing Wang, Liguang Xu, Wei-Shun Chang, Huanan Zhang, Maozhong Sun, Yinyue Zhu, Yuan Zhao, Liqiang Liu, et al. Chiral plasmonics of self-assembled nanorod dimers. *Scientific reports*, 3:1934, 2013.

[34] Xiaoyang Xu, Nathaniel L Rosi, Yuhuang Wang, Fengwei Huo, and Chad A Mirkin. Asymmetric functionalization of gold nanoparticles with oligonucleotides. *Journal of the American Chemical Society*, 128(29):9286–9287, 2006.

[35] Marcin Fialkowski, Kyle JM Bishop, Rafal Klajn, Stoyan K Smoukov, Christopher J Campbell, and Bartosz A Grzybowski. Principles and implementations of dissipative (dynamic) self-assembly, 2006.

[36] Jeroen van Herrikhuyzen, René AJ Janssen, EW Meijer, Stefan CJ Meskers, and Albertus PHJ Schenning. Fractal-like self-assembly of oligo (p-phenylene vinylene) capped gold nanoparticles. *Journal of the American Chemical Society*, 128(3):686–687, 2006.

[37] Zhihong Nie, Daniele Fava, Eugenia Kumacheva, Shan Zou, Gilbert C Walker, and Michael Rubinstein. Self-assembly of metal–polymer analogues of amphiphilic triblock copolymers. *Nature materials*, 6(8):609, 2007.

[38] Tieying Gong, David T Wu, and David WM Marr. Electric field-reversible three-dimensional colloidal crystals. *Langmuir*, 19(15):5967–5970, 2003.

[39] Sumit Gangwal, Olivier J Cayre, and Orlin D Velev. Dielectrophoretic assembly of metallodielectric janus particles in ac electric fields. *Langmuir*, 24(23):13312–13320, 2008.

[40] John P Singh, Pushkar P Lele, Florian Nettesheim, Norman J Wagner, and Eric M Furst. One-and two-dimensional assembly of colloidal ellipsoids in ac electric fields. *Physical Review E*, 79(5):050401, 2009.

[41] ABD Brown, CG Smith, and AR Rennie. Fabricating colloidal particles with photolithography and their interactions at an air-water interface. *Physical Review E*, 62(1):951, 2000.

[42] MG Basavaraj, GG Fuller, Jan Fransaer, and Jan Vermant. Packing, flipping, and buckling transitions in compressed monolayers of ellipsoidal latex particles. *Langmuir*, 22(15):6605–6612, 2006.

[43] Richard P Sear, Sung-Wook Chung, Gil Markovich, William M Gelbart, and James R Heath. Spontaneous patterning of quantum dots at the air-water interface. *Physical Review E*, 59(6):R6255, 1999.

[44] Kohji Ohno, Kyoung-moo Koh, Yoshinobu Tsujii, and Takeshi Fukuda. Synthesis of gold nanoparticles coated with well-defined, high-density polymer brushes by surface-initiated living radical polymerization. *Macromolecules*, 35(24):8989–8993, 2002.

[45] Tyler B Norsten, Benjamin L Frankamp, and Vincent M Rotello. Metal directed assembly of terpyridine-functionalized gold nanoparticles. *Nano Letters*, 2(12):1345–1348, 2002.

[46] Bo Gao, Gaurav Arya, and Andrea R Tao. Self-orienting nanocubes for the assembly of plasmonic nanojunctions. *Nature nanotechnology*, 7(7):433, 2012.

[47] Bo Gao, Yahya Alvi, David Rosen, Marvin Lav, and Andrea R Tao. Designer nanojunctions: orienting shaped nanoparticles within polymer thin-film nanocomposites. *Chemical Communications*, 49(39):4382–4384, 2013.

[48] Benjamin L Frankamp, Andrew K Boal, and Vincent M Rotello. Controlled interparticle spacing through self-assembly of au nanoparticles and poly (amidoamine) dendrimers. *Journal of the American Chemical Society*, 124(51):15146–15147, 2002.

[49] Pasquale F Fulvio, Richard T Mayes, Xiqing Wang, Shannon M Mahurin, John C Bauer, Volker Presser, John McDonough, Yury Gogotsi, and Sheng Dai. "brick-and-mortar" self-assembly approach to graphitic mesoporous carbon nanocomposites. *Advanced Functional Materials*, 21(12):2208–2215, 2011.

[50] Yair Korenblit, Marcus Rose, Emanuel Kockrick, Lars Borchardt, Alexander Kvit, Stefan Kaskel, and Gleb Yushin. High-rate electrochemical capacitors based on ordered mesoporous silicon carbide-derived carbon. *Acs Nano*, 4(3):1337–1344, 2010.

[51] Patrice Simon and Yury Gogotsi. Materials for electrochemical capacitors. In *Nanoscience And Technology: A Collection of Reviews from Nature Journals*, pages 320–329. World Scientific, 2010.

[52] David Pech, Magali Brunet, Hugo Durou, Peihua Huang, Vadym Mochalin, Yury Gogotsi, Pierre-Louis Taberna, and Patrice Simon. Ultrahigh-power micrometre-sized supercapacitors based on onion-like carbon. *Nature nanotechnology*, 5(9):651, 2010.

[53] Pedro MR Paulo, Jose N Canongia Lopes, and Sílvia MB Costa. Molecular dynamics simulations of charged dendrimers: Low-to-intermediate half-generation pamams. *The Journal of Physical Chemistry B*, 111(36):10651–10664, 2007.

[54] Siewert J Marrink, H Jelger Risselada, Serge Yefimov, D Peter Tieleman, and Alex H De Vries. The martini force field: coarse grained model for biomolecular simulations. *The journal of physical chemistry B*, 111(27):7812–7824, 2007.

[55] Hwankyu Lee and Ronald G Larson. Molecular dynamics simulations of pamam dendrimer-induced pore formation in dppc bilayers with a coarse-grained model. *The Journal of Physical Chemistry B*, 110(37):18204–18211, 2006.

[56] Wolfgang H Binder, Christian Kluger, Christoph J Straif, and Gernot Friedbacher. Directed nanoparticle binding onto microphase-separated block copolymer thin films. *Macromolecules*, 38(23):9405–9410, 2005.

[57] Yue Zhao, Kari Thorkelsson, Alexander J Mastroianni, Thomas Schilling, Joseph M Luther, Benjamin J Rancatore, Kazuyuki Matsunaga, Hiroshi Jinnai, Yue Wu, Daniel Poulsen, et al. Small-molecule-directed nanoparticle assembly towards stimuli-responsive nanocomposites. *Nature materials*, 8(12):979, 2009.

[58] Marek Grzelczak, Jan Vermant, Eric M Furst, and Luis M Liz-Marzán. Directed self-assembly of nanoparticles. *ACS Nano*, 4(7):3591–3605, 2010.

[59] Zhihong Nie, Alla Petukhova, and Eugenia Kumacheva. Properties and emerging applications of self-assembled structures made from inorganic nanoparticles. *Nat. Nanotechnol.*, 5(1):15–25, 2010.

[60] Sharon C Glotzer and Michael J Solomon. Anisotropy of building blocks and their assembly into complex structures. *Nat. Mater.*, 6(8):557–562, 2007.

[61] Xiaogang Peng, Liberato Manna, Weidong Yang, Juanita Wickham, Erik Scher, Andreas Kadavanich, and A Paul Alivisatos. Shape control of cdse nanocrystals. *Nature*, 404(6773):59–61, 2000.

[62] Andrea R Tao, Susan Habas, and Peidong Yang. Shape control of colloidal metal nanocrystals. *Small*, 4(3):310–325, 2008.

[63] Karol Miszta, Joost de Graaf, Giovanni Bertoni, Dirk Dorfs, Rosaria Brescia, Sergio Marras, Luca Ceseracciu, Roberto Cingolani, René van Roij, and Marjolein Dijkstra. Hierarchical self-assembly of suspended branched colloidal nanocrystals into superlattice structures. *Nat. Mater.*, 10(11):872–876, 2011.

[64] Liberato Manna, Erik C Scher, and A Paul Alivisatos. Synthesis of soluble and processable rod-, arrow-, teardrop-, and tetrapod-shaped cdse nanocrystals. *J. Am. Chem. Soc.*, 122(51):12700–12706, 2000.

[65] Joel Henzie, Michael Grünwald, Asaph Widmer-Cooper, Phillip L Geissler, and Peidong Yang. Self-assembly of uniform polyhedral silver nanocrystals into densest packings and exotic superlattices. *Nat. Mater.*, 11(2):131–137, 2012.

[66] Marco Zanella, Giovanni Bertoni, Isabella R Franchini, Rosaria Brescia, Dmitry Baranov, and Liberato Manna. Assembly of shape-controlled nanocrystals by depletion attraction. *Chem. Commun.*, 47(1):203–205, 2011.

[67] André H Gröschel, Andreas Walther, Tina I Löbling, Felix H Schacher, Holger Schmalz, and Axel HE Müller. Guided hierarchical co-assembly of soft patchy nanoparticles. *Nature*, 503(7475):247–251, 2013.

[68] Jianzhong Du and Rachel K O'Reilly. Anisotropic particles with patchy, multicompartment and janus architectures: preparation and application. *Chem. Soc. Rev.*, 40(5):2402–2416, 2011.

[69] Matthew N O' Brien, Matthew R Jones, Byeongdu Lee, and Chad A Mirkin. Anisotropic nanoparticle complementarity in dna-mediated co-crystallization. *Nat. Mater.*, 14(8):833–839, 2015.

[70] Marco Lattuada and T Alan Hatton. Preparation and controlled self-assembly of janus magnetic nanoparticles. *J. Amer. Chem. Soc.*, 129(42):12878–12889, 2007.

[71] Gianpetro Malescio and Giuseppe Pellicane. Stripe phases from isotropic repulsive interactions. *Nat. Mater.*, 2:97–100, 2003.

[72] Pinar Akcora, Hongjun Liu, Sanat K Kumar, Joseph Moll, Yu Li, Brian C Benicewicz, Linda S Schadler, Devrim Acehan, Athanassios Z Panagiotopoulos, Victor Pryamitsyn, Venkat Ganesan, Jan Ilavsky, Pappanan Thiyagarajan, Ralph H. Colby, and Jack F. Douglas. Anisotropic self-assembly of spherical polymer-grafted nanoparticles. *Nat. Mater.*, 8(4):354–359, 2009.

[73] Dmitry Bedrov, Grant D. Smith, and Liwei Li. Molecular dynamics simulation study of the role of evenly spaced poly(ethylene oxide) tethers on the aggregation of c60 fullerenes in water. *Langmuir*, 21(12):5251–5255, 2005.

[74] Samanvaya Srivastava, Praveen Agarwal, and Lynden A Archer. Tethered nanoparticle–polymer composites: phase stability and curvature. *Langmuir*, 28(15):6276–6281, 2012.

[75] Yang Jiao and Pinar Akcora. Assembly of polymer-grafted magnetic nanoparticles in polymer melts. *Macromolecules*, 45(8):3463–3470, 2012.

[76] Hilmar Koerner, Lawrence F Drummy, Brian Benicewicz, Yu Li, and Richard A Vaia. Nonisotropic self-organization of single-component hairy nanoparticle assemblies. *ACS Macro Letters*, 2(8):670–676, 2013.

[77] Victor Pryamtisyn, Venkat Ganesan, Athanassios Z. Panagiotopoulos, Hongjun Liu, and Sanat K. Kumar. Modeling the anisotropic self-assembly of spherical polymer-grafted nanoparticles. *J. Chem. Phys.*, 131(22):221102, 2009.

[78] Gregory D Hattemer and Gaurav Arya. Viscoelastic properties of polymer-grafted nanoparticle composites from molecular dynamics simulations. *Macromolecules*, 48(4):1240–1255, 2015.

[79] Kurt Kremer and Gary S Grest. Dynamics of entangled linear polymer melts: A molecular-dynamics simulation. *J. Chem. Phys.*, 92(8):5057–5086, 1990.

[80] John D Weeks, David Chandler, and Hans C Andersen. Role of repulsive forces in determining the equilibrium structure of simple liquids. *J. Chem. Phys.*, 54(12):5237–5247, 1971.

[81] Evguenii A Rakhmanov, EB Saff, and YM Zhou. Minimal discrete energy on the sphere. *Math. Res. Lett*, 1(6):647–662, 1994.

[82] Edward B Saff and A BJ Kuijlaars. Distributing many points on a sphere. *The mathematical intelligencer*, 19(1):5–11, 1997.

[83] EA Carter, Giovanni Ciccotti, James T Hynes, and Raymond Kapral. Constrained reaction coordinate dynamics for the simulation of rare events. *Chem. Phys. Lett.*, 156(5):472–477, 1989.

[84] Michiel Sprik and Giovanni Ciccotti. Free energy from constrained molecular dynamics. *J. Chem. Phys.*, 109(18):7737–7744, 1998.

[85] E Guardia, R Rey, and JA Padró. Potential of mean force by constrained molecular dynamics: a sodium chloride ion-pair in water. *Chem. Phys.*, 155(2):187–195, 1991.

[86] Gaurav Arya. Chain stiffness and attachment-dependent attraction between polyelectrolyte-grafted colloids. *J. Phys. Chem. B*, 114(48):15886–15896, 2010.

[87] Nosé Shuichi. Constant temperature molecular dynamics methods. *Prog. Theoretical Phys. Suppl.*, 103:1–46, 1991.

[88] Steve Plimpton. Fast parallel algorithms for short-range molecular dynamics. *J. Comput. Phys.*, 117(1):1–19, 1995.

[89] Gary S Grest. Communication: Polymer entanglement dynamics: Role of attractive interactions. *J. Chem. Phys.*, 145(14):141101, 2016.

[90] Sho Asakura and Fumio Oosawa. On interaction between two bodies immersed in a solution of macromolecules. *J. Chem. Phys.*, 22(7):1255–1256, 1954.

[91] Sho Asakura and Fumio Oosawa. Interaction between particles suspended in solutions of macromolecules. *J. Polym. Sci.*, 33(126):183–192, 1958.

[92] Dong Meng, Sanat K Kumar, J Matthew D Lane, and Gary S Grest. Effective interactions between grafted nanoparticles in a polymer matrix. *Soft Matter*, 8(18):5002–5010, 2012.

[93] Jonathan A Fan, Chihhui Wu, Kui Bao, Jiming Bao, Rizia Bardhan, Naomi J Halas, Vinothan N Manoharan, Peter Nordlander, Gennady Shvets, and Federico Capasso. Self-assembled plasmonic nanoparticle clusters. *Science*, 328(5982):1135–1138, 2010.

[94] Izchak Z Steinberg and Harold A Scheraga. Entropy changes accompanying association reactions of proteins. *J. Biol. Chem.*, 238(1):172–181, 1963.

[95] Su-Wen Hsu, Andrea L Rodarte, Madhura Som, Gaurav Arya, and Andrea R Tao. Colloidal plasmonic nanocomposites: From fabrication to optical function. *Chem. Rev.*, 118(6):3100–3120, 2018.

[96] Youngjong Kang, Kris J Erickson, and T Andrew Taton. Plasmonic nanoparticle chains via a morphological, sphere-to-string transition. *J. Am. Chem. Soc.*, 127(40):13800–13801, 2005.

[97] P Spinelli, M Hebbink, R De Waele, L Black, F Lenzmann, and A Polman. Optical impedance matching using coupled plasmonic nanoparticle arrays. *Nano Lett.*, 11(4):1760–1765, 2011.

[98] Jesse Theiss, Prathamesh Pavaskar, Pierre M Echternach, Richard E Muller, and Stephen B Cronin. Plasmonic nanoparticle arrays with nanometer separation for high-performance sers substrates. *Nano Lett.*, 10(8):2749–2754, 2010.

[99] Kazuya Nakata, Ying Hu, Oktay Uzun, Osman Bakr, and Francesco Stellacci. Chains of superparamagnetic nanoparticles. *Adv. Mater.*, 20(22):4294–4299, 2008.

[100] Y Lalatonne, L Motte, V Russier, AT Ngo, P Bonville, and MP Pileni. Mesoscopic structures of nanocrystals: collective magnetic properties due to the alignment of nanocrystals. *J. Phys. Chem. B*, 108(6):1848–1854, 2004.

[101] Rolf Koole, Peter Liljeroth, Celso de Mello Donegá, Daniël Vanmaekelbergh, and Andries Meijerink. Electronic coupling and exciton energy transfer in cdte quantum-dot molecules. *J. Am. Chem. Soc.*, 128(32):10436–10441, 2006.

[102] Alexander O Govorov, Garnett W Bryant, Wei Zhang, Timur Skeini, Jaebeom Lee, Nicholas A Kotov, Joseph M Slocik, and Rajesh R Naik. Exciton- plasmon interaction and hybrid excitons in semiconductor- metal nanoparticle assemblies. *Nano Lett.*, 6(5):984–994, 2006.

[103] Olga Kulakovich, Natalya Strekal, Alexandr Yaroshevich, Sergey Maskevich, Sergey Gaponenko, Igor Nabiev, Ulrike Woggon, and Mikhail Artemyev. Enhanced luminescence of cdse quantum dots on gold colloids. *Nano Lett.*, 2(12):1449–1452, 2002.

[104] Anna C Balazs, Todd Emrick, and Thomas P Russell. Nanoparticle polymer composites: where two small worlds meet. *Science*, 314(5802):1107–1110, 2006.

[105] Anne-Caroline Genix and Julian Oberdisse. Nanoparticle self-assembly: from interactions in suspension to polymer nanocomposites. *Soft Matter*, 2018.

[106] Chaitanya R Murthy, Bo Gao, Andrea R Tao, and Gaurav Arya. Automated quantitative image analysis of nanoparticle assembly. *Nanoscale*, 7(21):9793–9805, 2015.

[107] Min Chen, Jaemin Kim, JP Liu, Hongyou Fan, and Shouheng Sun. Synthesis of fept nanocubes and their oriented self-assembly. *J. Am. Chem. Soc.*, 128(22):7132–7133, 2006.

[108] Brendan Pietrobon, Matthew McEachran, and Vladimir Kitaev. Synthesis of size-controlled faceted pentagonal silver nanorods with tunable plasmonic properties and self-assembly of these nanorods. *ACS Nano*, 3(1):21–26, 2008.

[109] Zhenli Zhang and Sharon C Glotzer. Self-assembly of patchy particles. *Nano Lett.*, 4(8):1407–1413, 2004.

[110] Sanat K Kumar, Nicolas Jouault, Brian Benicewicz, and Tony Neely. Nanocomposites with polymer grafted nanoparticles. *Macromolecules*, 46(9):3199–3214, 2013.

[111] Tsung-Yeh Tang and Gaurav Arya. Anisotropic three-particle interactions between spherical polymer-grafted nanoparticles in a polymer matrix. *Macromolecules*, 50(3):1167–1183, 2017.

[112] Bumjoon J Kim, Joona Bang, Craig J Hawker, Julia J Chiu, David J Pine, Se Gyu Jang, Seung-Man Yang, and Edward J Kramer. Creating surfactant nanoparticles for block copolymer composites through surface chemistry. *Langmuir*, 23(25):12693–12703, 2007.

[113] Michael R Bockstaller, Yonit Lapetnikov, Shlomo Margel, and Edwin L Thomas. Size-selective organization of enthalpic compatibilized nanocrystals in ternary block copolymer/particle mixtures. *J. Am. Chem. Soc.*, 125(18):5276–5277, 2003.

[114] Byeong-Hyeok Sohn, Jeong-Min Choi, Seong Il Yoo, Sang-Hyun Yun, Wang-Cheol Zin, Jin Chul Jung, Masayuki Kanehara, Takuji Hirata, and Toshiharu Teranishi. Directed self-assembly of two kinds of nanoparticles utilizing monolayer films of diblock copolymer micelles. *Journal of the American Chemical Society*, 125(21):6368–6369, 2003.

[115] Qingling Zhang, Ting Xu, David Butterfield, Matthew J Misner, Du Yoel Ryu, Todd Emrick, and Thomas P Russell. Controlled placement of cdse nanoparticles in diblock copolymer templates by electrophoretic deposition. *Nano Lett.*, 5(2):357–361, 2005.

[116] Randall M Erb, Hui S Son, Bappaditya Samanta, Vincent M Rotello, and Benjamin B Yellen. Magnetic assembly of colloidal superstructures with multipole symmetry. *Nature*, 457(7232):999, 2009.

[117] Pawel Pieranski. Two-dimensional interfacial colloidal crystals. *Phys. Rev. Lett.*, 45(7):569, 1980.

[118] Bernard P Binks and Tommy S Horozov. *Colloidal particles at liquid interfaces*. Cambridge University Press, 2006.

[119] Alexander Böker, Jinbo He, Todd Emrick, and Thomas P Russell. Self-assembly of nanoparticles at interfaces. *Soft Matter*, 3(10):1231–1248, 2007.

[120] F Bresme and M Oettel. Nanoparticles at fluid interfaces. *J. Phys.: Condens. Mat.*, 19(41):413101, 2007.

[121] David L Cheung. Molecular dynamics study of nanoparticle stability at liquid interfaces: effect of nanoparticle-solvent interaction and capillary waves. *J. Chem. Phys.*, 135(5):054704, 2011.

[122] Guillaume Galliero. Lennard-jones fluid-fluid interfaces under shear. *Physical Review E*, 81(5):056306, 2010.

[123] Hossein Rezvantalab and Shahab Shojaei-Zadeh. Tilting and tumbling of janus nanoparticles at sheared interfaces. *ACS nano*, 10(5):5354–5361, 2016.

[124] Samuel Levine, Bruce D Bowen, and Susan J Partridge. Stabilization of emulsions by fine particles i. partitioning of particles between continuous phase and oil/water interface. *Colloids Surfaces*, 38(2):325–343, 1989.

[125] Y Lin, H Skaff, Todd Emrick, AD Dinsmore, and Thomas P Russell. Nanoparticle assembly and transport at liquid-liquid interfaces. *Science*, 299(5604):226–229, 2003.

[126] Natalie Arkus, Vinothan N Manoharan, and Michael P Brenner. Minimal energy clusters of hard spheres with short range attractions. *Physical review letters*, 103(11):118303, 2009.

[127] Stefano Mossa, Francesco Sciortino, Piero Tartaglia, and Emanuela Zaccarelli. Ground-state clusters for short-range attractive and long-range repulsive potentials. *Langmuir*, 20(24):10756–10763, 2004.

[128] Qingguang Xie, Gary B Davies, and Jens Harting. Direct assembly of magnetic janus particles at a droplet interface. *ACS Nano*, 11(11):11232–11239, 2017.

[129] Leif J Sherry, Shih-Hui Chang, George C Schatz, Richard P Van Duyne, Benjamin J Wiley, and Younan Xia. Localized surface plasmon resonance spectroscopy of single silver nanocubes. *Nano Lett.*, 5(10):2034–2038, 2005.

[130] Riccardo Ferrando, Julius Jellinek, and Roy L Johnston. Nanoalloys: from theory to applications of alloy clusters and nanoparticles. *Chem. Rev.*, 108(3):845–910, 2008.

[131] Su-Wen Hsu, Yuhan Long, Aatheya G Subramanian, and Andrea R Tao. Directed assembly of metal nanoparticles in polymer bilayers. *Mol. Sys. Des. Eng.*, 3(2):390–396, 2018.

[132] Paz Padilla, So/ren Toxvaerd, and J Stecki. Shear flow at liquid–liquid interfaces. *J. Chem. Phys.*, 103(2):716–724, 1995.

[133] Souheng Wu. Calculation of interfacial tension in polymer systems. In *J. Polym. Sci. Part C. Polym. Symp.*, volume 34, pages 19–30. Wiley Online Library, 1971.

[134] Eugene Helfand and Yukiko Tagami. Theory of the interface between immiscible polymers. *J. Polym. Sci. Part B: Polym. Lett.*, 9(10):741–746, 1971.

[135] Russell B Thompson, Valeriy V Ginzburg, Mark W Matsen, and Anna C Balazs. Predicting the mesophases of copolymer-nanoparticle composites. *Science*, 292(5526):2469–2472, 2001.

[136] S Srivastava and JK Basu. Experimental evidence for a new parameter to control the glass transition of confined polymers. *Phys. Rev. Lett.*, 98(16):165701, 2007.

[137] Qiang Zhang and Lynden A Archer. Poly (ethylene oxide)/silica nanocomposites: structure and rheology. *Langmuir*, 18(26):10435–10442, 2002.

[138] SS Sternstein and Ai Jun Zhu. Reinforcement mechanism of nanofilled polymer melts as elucidated by nonlinear viscoelastic behavior. *Macromolecules*, 35(19):7262–7273, 2002.

[139] Michael E Mackay, Tien T Dao, Anish Tuteja, Derek L Ho, Brooke Van Horn, Ho Cheol Kim, and Craig J Hawker. Nanoscale effects leading to non-einstein-like decrease in viscosity. *Nat. Mater.*, 2(11):762, 2003.

[140] Giovanni Filippone, Giovanni Romeo, and Domenico Acierno. Viscoelasticity and structure of polystyrene/fumed silica nanocomposites: filler network and hydrodynamic contributions. *Langmuir*, 26(4):2714–2720, 2009.

[141] Hua Wang, Changchun Zeng, Mark Elkovitch, L James Lee, and Kurt W Koelling. Processing and properties of polymeric nano-composites. *Poly. Eng. & Sci.*, 41(11):2036–2046, 2001.

[142] Michael E Mackay, Anish Tuteja, Phillip M Duxbury, Craig J Hawker, Brooke Van Horn, Zhibin Guan, Guanghui Chen, and RS Krishnan. General strategies for nanoparticle dispersion. *Science*, 311(5768):1740–1743, 2006.

[143] Luca Cipelletti, Suliana Manley, RC Ball, and DA Weitz. Universal aging features in the restructuring of fractal colloidal gels. *Phys. Rev. Lett.*, 84(10):2275, 2000.

[144] Rami A Omari, Andrew M Aneese, Christopher A Grabowski, and Ashis Mukhopadhyay. Diffusion of nanoparticles in semidilute and entangled polymer solutions. *J. Phys. Chem. B*, 113(25):8449–8452, 2009.

[145] Christopher A Grabowski, Bijoy Adhikary, and Ashis Mukhopadhyay. Dynamics of gold nanoparticles in a polymer melt. *Appl. Phys. Lett.*, 94(2):021903, 2009.

[146] S Srivastava, AK Kandar, JK Basu, MK Mukhopadhyay, LB Lurio, S Narayanan, and S. K. Sinha. Complex dynamics in polymer nanocomposites. *Phys. Rev. E*, 79(2):021408, 2009.

[147] Daniel Kim, Samanvaya Srivastava, Suresh Narayanan, and Lynden A Archer. Polymer nanocomposites: polymer and particle dynamics. *Soft Matter*, 8(42):10813–10818, 2012.

[148] Anne Caroline Genix and Julian Oberdisse. Structure and dynamics of polymer nanocomposites studied by x-ray and neutron scattering techniques. *Curr. Opi. in Coll. & Int. Sci.*, 20(4):293–303, 2015.

[149] Hongyu Guo, Gilles Bourret, R Bruce Lennox, Mark Sutton, James L Harden, and Robert L Leheny. Entanglement-controlled subdiffusion of nanoparticles within concentrated polymer solutions. *Phys. Rev. Lett.*, 109(5):055901, 2012.

[150] Tadanori Koga, C Li, MK Endoh, J Koo, M Rafailovich, S Narayanan, DR Lee, LB Lurio, and S. K. Sinha. Reduced viscosity of the free surface in entangled polymer melt films. *Phys. Rev. Lett.*, 104(6):066101, 2010.

[151] R Aravinda Narayanan, P Thiyagarajan, S Lewis, A Bansal, LS Schadler, and LB Lurio. Dynamics and internal stress at the nanoscale related to unique thermomechanical behavior in polymer nanocomposites. *Phys. Rev. Lett.*, 97(7):075505, 2006.

[152] Hongyu Guo, Gilles Bourret, Muriel K Corbierre, Simona Rucareanu, R Bruce Lennox, Khalid Laaziri, Luc Piche, Mark Sutton, James L Harden, and Robert L Leheny. Nanoparticle motion within glassy polymer melts. *Phys. Rev. Lett.*, 102(7):075702, 2009.

[153] Rahul Mangal, Samanvaya Srivastava, Suresh Narayanan, and Lynden A Archer. Size-dependent particle dynamics in entangled polymer nanocomposites. *Langmuir*, 32(2):596–603, 2016.

[154] Suresh Narayanan, Dong Ryeol Lee, Aleta Hagman, Xuefa Li, and Jin Wang. Particle dynamics in polymer-metal nanocomposite thin films on nanometer-length scales. *Phys. Rev. Lett.*, 98(18):185506, 2007.

[155] Aline Grein Iankovski, Izabel C Riegel Vidotti, Fernanda F Simas Tosin, Suresh Narayanan, Robert L Leheny, and Alec R Sandy. Exploring the relationship between nanoscale dynamics and macroscopic rheology in natural polymer gums. *Soft Matter*, 12(46):9321–9329, 2016.

[156] A Papagiannopoulos, TA Waigh, A Fluerasu, C Fernyhough, and A Madsen. Microrheology of polymeric solutions using x-ray photon correlation spectroscopy. *J. Phy. Condens. Matter.*, 17(25):L279, 2005.

[157] Li Heng Cai, Sergey Panyukov, and Michael Rubinstein. Mobility of nonsticky nanoparticles in polymer liquids. *Macromolecules*, 44(19):7853–7863, 2011.

[158] Li Heng Cai, Sergey Panyukov, and Michael Rubinstein. Hopping diffusion of nanoparticles in polymer matrices. *Macromolecules*, 48(3):847–862, 2015.

[159] B J Berne and Robert Pecora. *Dynamic light scattering: with applications to chemistry, biology, and physics,*. Dover Publications Inc., 1976.

[160] Julien RM Lhermitte, Michael C Rogers, Sabine Manet, and Mark Sutton. Velocity measurement by coherent x-ray heterodyning. *Review of Scientific Instruments*, 88(1):015112, 2017.

[161] F Livet, F Bley, F Ehrburger-Dolle, I Morfin, E Geissler, and M Sutton. X-ray intensity fluctuation spectroscopy by heterodyne detection. *Journal of synchrotron radiation*, 13(6):453–458, 2006.

[162] Sebastian Busch, Torben Haugaard Jensen, Yuriy Chushkin, and Andrei Fluerasu. Dynamics in shear flow studied by x-ray photon correlation spectroscopy. *The European Physical Journal E*, 26(1-2):55, 2008.

[163] Luca Cipelletti, Laurence Ramos, Suliana Manley, Estelle Pitard, DAVID A Weitz, Eugene E Pashkovski, and Marie Johansson. Universal non-diffusive slow dynamics in aging soft matter. *Faraday Discussions*, 123:237–251, 2003.

[164] Jihoon Choi, Michael JA Hore, Nigel Clarke, Karen I Winey, and Russell J Composto. Nanoparticle brush architecture controls polymer diffusion in nanocomposites. *Macromolecules*, 47(7):2404–2410, 2014.

[165] Jihoon Choi, Michael JA Hore, Jeffrey S Meth, Nigel Clarke, Karen I Winey, and Russell J Composto. Universal scaling of polymer diffusion in nanocomposites. *ACS Macro Letters*, 2(6):485–490, 2013.

[166] Jerome Carnis, Wonsuk Cha, James Wingert, Jinback Kang, Zhang Jiang, Sanghoon Song, Marcin Sikorski, Aymeric Robert, Christian Gutt, San-Wen Chen, et al. Demonstration of feasibility of x-ray free electron laser studies of dynamics of nanoparticles in entangled polymer melts. *Scientific reports*, 4:6017, 2014.

[167] Jean-Charles Majeste, J-P Montfort, Ahmed Allal, and Gérard Marin. Viscoelasticity of low molecular weight polymers and the transition to the entangled regime. *Rheologica acta*, 37(5):486–499, 1998.

[168] Jean Philippe Bouchaud and Antoine Georges. Anomalous diffusion in disordered media: statistical mechanisms, models and physical applications. *Phys. Rep.*, 195(4-5):127–293, 1990.

[169] V Zaburdaev, S Denisov, and J Klafter. Lévy walks. *Rev. Mod. Phys.*, 87(2):483, 2015.

[170] Thomas Schweizer, Jan van Meerveld, and Hans Christian Öttinger. Nonlinear shear rheology of polystyrene melt with narrow molecular weight distribution—experiment and theory. *Journal of rheology*, 48(6):1345–1363, 2004.

[171] Salvatore Costanzo, Qian Huang, Giovanni Ianniruberto, Giuseppe Marrucci, Ole Hassager, and Dimitris Vlassopoulos. Shear and extensional rheology of polystyrene melts and solutions with the same number of entanglements. *Macromolecules*, 49(10):3925–3935, 2016.

[172] J P Bouchaud and E Pitard. Anomalous dynamical light scattering in soft glassy gels. *Eur. Phys. J. E*, 6(3):231–236, 2001.